Design of Protein-Based Hybrid Catalysts for Fuel Production

by

Dayn Sommer

A Dissertation Presented in Partial Fulfillment
of the Requirements for the Degree
Doctor of Philosophy

Approved April 2016 by the
Graduate Supervisory Committee:

Giovanna Ghirlanda, Chair
Kevin Redding
Gary Moore

ARIZONA STATE UNIVERSITY

May 2016

ABSTRACT

One of the greatest problems facing society today is the development of a sustainable, carbon neutral energy source to curb the reliance on fossil fuel combustion as the primary source of energy. To overcome this challenge, research efforts have turned to biology for inspiration, as nature is adept at inter-converting low molecular weight precursors into complex molecules. A number of inorganic catalysts have been reported that mimic the active sites of energy-relevant enzymes such as hydrogenases and carbon monoxide dehydrogenase. However, these inorganic models fail to achieve the high activity of the enzymes, which function in aqueous systems, as they lack the critical secondary-shell interactions that enable the active site of enzymes to outperform their organometallic counterparts.

To address these challenges, my work utilizes bio-hybrid systems in which artificial proteins are used to modulate the properties of organometallic catalysts. This approach couples the diversity of organometallic function with the robust nature of protein biochemistry, aiming to utilize the protein scaffold to not only enhance rates of reaction, but also to control catalytic cycles and reaction outcomes. To this end, I have used chemical biology techniques to modify natural protein structures and augment the H_2 producing ability of a cobalt-catalyst by a factor of five through simple mutagenesis. Concurrently I have designed and characterized a de novo peptide that incorporates various iron sulfur clusters at discrete distances from one another, facilitating electron transfer between the two. Finally, using computational methodologies I have engineered proteins to alter the specificity of a

CO_2 reduction reaction. The proteins systems developed herein allow for study of protein secondary-shell interactions during catalysis, and enable structure-function relationships to be built. The complete system will be interfaced with a solar fuel cell, accepting electrons from a photosensitized dye and storing energy in chemical bonds, such as H_2 or methanol.

ACKNOWLEDGMENTS

My thesis was made possible by contributions from many people over the years, many who will never know their impressions on me, however there are a few extraordinary examples that I would like to make note of.

First and most important is my advisor, Giovanna Ghirlanda. Her constant support of my crazy ideas, dealing with my constant nagging about publishing, and outstanding cheerleading for my cause has allowed me to be in the position that I am in today, for which I will be forever grateful. I look forward to continued collaboration and contact in the future. I would also like to thank my committee members, Kevin Redding and Gary Moore, for making me a better scientist through both coursework and their overall outlook on science. Multiple other faculty members at ASU also contributed greatly to my education: Anne Jones for teaching me that the devil is in the details, John Chaput for allowing me to rotate and learn *in vitro* evolution, Wilson Francisco and Ian Gould for sitting for my orals examination, and Devens Gust and Thomas Moore for instrument use and support.

Most of the CO_2 work would not be possible without funding from the Department of Energy, Office of Science Student Graduate Research Program, and my advisors Etsuko Fujita and Jim Muckerman for hosting me for 9 months at Brookhaven National Lab.

I have been fortunate to have great advisors during my scientific career, but the work would not have been accomplished without boots on the ground: the undergraduate and graduate students, as well as postdocs that helped me in my

cause. To all of my past and future coauthors (Michael Vaughn, Anindya Roy, Bobby Schmitz, Chelsea Brown, Andrei Astashkin, Marina Faiella, Annabelle Gillig, Brett Clark, Jason Allen, Rafael Alcala Torano, Zahra Bahrami Dizicheh, Jesse Coe, Gerald Manbeck, M. Zahid Ertem, Gerdenis Kodis, and John Tomlin), thank you for your excellent experimental and intellectual contributions to my work. Michael Vaughn and Anindya Roy, in particular, were instrumental in developing me into, "Do whatever it takes to get it done" type scientist, something I will take forward and wear with pride in future endeavors. Rafael Alcala Torano aided in my sanity by listening to my crazy ideas and constant questions about organic chemistry, providing great guidance and reassurance. Gerald Manbeck and Zahid Ertem were instrumental in pushing my projects forward at BNL, thank you for dealing with my naïve ways and helping me learn new techniques. I would also like to thank Brian Woodrum for willingness to train me on instruments and have as many friendly arguments as possible. I would like by thank all of the students that I encountered during my time in the Ghirlanda lab; I hope I made a positive impact on your career.

My family and friends were the best support system that I could have asked for. My family put up with me explaining the confusing world of science, so thank you Mom and Matt for putting up with me over the last four years. Friends, particularly David Jennings, thank you for countless cups of coffee and extended happy hours. Finally, Aurelie Marcotte was heroic on countless occasions, providing a level head, exciting adventures, and outstanding scientific support, all at precisely the right time.

TABLE OF CONTENTS

Page

LIST OF TABLES

Table Page

LIST OF FIGURES

Figure Page

Figure Page

Figure Page

Figure Page

CHAPTER 1

PREFACE

As the world's population continues to grow, one of the most important challenges facing modern society is the development of sustainable energy sources. Currently, the majority of energy utilized comes in the form of fossil fuels such as coal and oil; use of these fuels has unsustainable consequences on the environment as combustion increases pollution and greenhouse gas levels in the atmosphere.[1, 2] Along with the negative effects on the environment, political and social unrest are created over the allocation of an ever-dwindling supply of fuels.

To address this issue a number of alternatives have risen in usage in recent history. Sources such as natural gas, while more environmentally friendly in the short term, still rely on discovery and harvesting of finite amounts in Earth's reservoirs.[1] More modern sources rely on truly renewable sources of energy, such as photovoltaic cells utilizing solar energy and turbines harnessing wind; these energy sources also tend to have a smaller carbon footprint than combustible fuels, making them an attractive alternative. At the root of most sustainable sources is the conversion of solar energy into mechanical or chemical energy.[3] With the sun providing over 172,500 TW of energy to the earth, of which 80,700 TW falls on the surface, the energy requirements of modern society (approximately 40 TW) could be met by harvesting a fraction of the total incident light hitting the earth.[4] While photovoltaic devices are starting to harness this energy as electrical current, they are only able to provide energy during the daytime hours. With this in mind, many

researchers have been inspired to utilize sunlight to store energy in chemical bonds for later use, allowing for the harnessed solar energy to be utilized more efficiently during peak-use hours.

Current materials utilized in commercial solar fuel cells are often comprised of precious metal-based materials, using metals such as Ru, Ir, and Pt to perform the chemical conversions.[4] Precious metals are electronically poised to be great catalysts for redox chemistry as diffuse molecular orbitals enable them to carry out two-electron chemistries; most energetically relevant reactions require the transfer of multiple electrons and protons along the reaction pathway. Furthermore the bond strength between reactants and products allows the reaction to proceed quickly as reactants bind tightly and products are released quickly. Although extraordinarily good as catalysts, scalability issues has hampered the wide-spread use of these systems, as precious metals are a valuable commodity that can not easily be made affordable using common economy-of scale methods. Instead of using precious metals it has become desirable to use earth-abundant metals, with many researchers taking inspiration from nature to develop the renewable devices.

Nature uses solar energy to power biological processes through photosynthesis, storing solar radiation in energy rich molecules that in turn are used to drive cellular metabolism. This process indirectly powers most life on the planet as it maintains oxygen levels in the atmosphere, generates key organic molecules, and supports the growth of biomass that in turns is used as food. Fossil

fuels are also ultimately derived from biomass resulting from photosynthetic solar energy conversion.

At the heart of the photosynthetic pathway, as well as other small molecule activating metabolic pathways, are the proteins that carry out both the chemical transformations and the shuttling of electrons. In order to accomplish these tasks, nearly all energy-relevant proteins utilize earth abundant metals at their active sites to facilitate the chemistry.[5] Over the years a large amount of work has accumulated on the study of these metallocenters as well as the synthesis of their inorganic counterparts, all with the aim to develop highly active, cheap, and robust catalysts.

One of the most desirable features of the proteins is their ability to function reversibly and at negligible overpotentials for electrocatalytic fuel production.[6] However, when inorganic models of the enzymes are studied under similar conditions they are often unstable, operate a large overpotentials, or fail to achieve similar catalytic turnover numbers as the parent enzyme.[7] With these observations it has been concluded that there is a strict requirement for the protein environment to provide crucial contacts to the active sites, stabilizing catalytically active geometries, and to facilitate transfer of reactants to/from the active site via gas channels or evolved proton shuttles.[8] Proteins such as hydrogenase and nitrogenase are also supramolecular assemblies containing multiple domains that each serves their own purpose along the catalytic cycle.

Although the natural enzymes have evolved to excel at the interconversion of energy *in vivo*, there are a number of traits that are hamper both the study of these

enzymes mechanisms and their application for biotechnological approaches. Coupled with their supramolecular nature comes the advanced biosynthetic pathways to assemble these proteins. Unlike inorganic mimics, which can be prepared in gram scale, enzymes often must be expressed from native sources in the low milligram scale, making it unrealistic for large-scale applications involving them. The size also affects the theoretical maximum for current density, as larger molecules decrease the number of active molecules adhered to a surface. Finally nearly all relevant enzymes are highly oxygen sensitive, necessitating a physical barrier in a fuel cell between oxidative and reductive reactions.

To overcome these barriers for utilization of proteins for biotechnological applications, our lab has pioneered a retrosynthetic approach to development of novel protein-based materials. Our unique approach splits the problem into a multiple facets to optimize individual components of the macromolecular system independently, with the eventual goal to bring all the components together as a functioning system for solar-driven fuel production. We have split the design into three components to study, two of which will be explored in detail in this thesis.

The first component to understand and optimize is the inorganic active site and the role of the protein in enhancing its reactivity; my thesis will study this aspect utilizing cobalt porphyrin catalysts in designed protein scaffolds as alternative to hydrogenase active site mimics. The second aspect is the means by which electrons are moved to and from the active site, a task that is accomplished in nature with the ubiquitous iron sulfur clusters. My work has focused on the design

and characterization of *de novo* peptides that incorporate iron-sulfur clusters at discrete distances from one another. The final aspect, use of metal directed assembly to bring individual components together while concurrently including a photosensitizer into the structure, will not be discussed in this thesis.

CHAPTER 2

DE NOVO DESIGN OF FES-CLUSTER PEPTIDES

2.1 Introduction

Hydrogenases generally contain an electron-transfer module containing iron-sulfur clusters in proximity of their redox-active catalytic site. (Figure 1) These cofactors are also found in other complex catalytic machinery such as the electron transfer chain, nitrogenases, and photosystem I (PSI), making them highly relevant in designing proteins for fuel production. A number of different groups have made recent advances in the incorporation of these electron transfer modules into peptides.

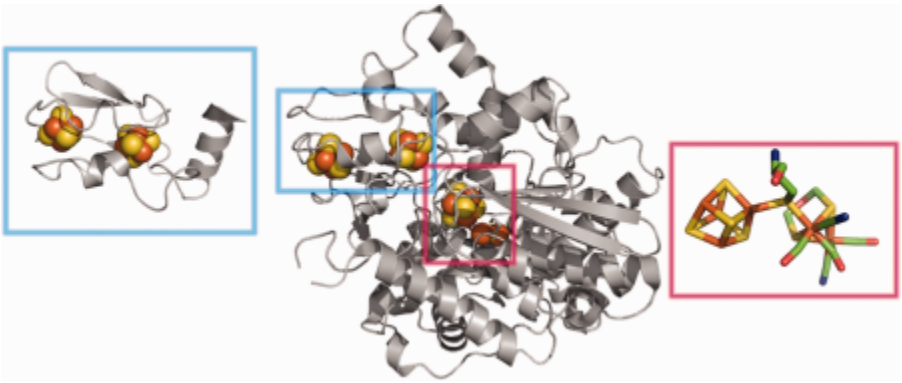

Figure 1: Structure of [FeFe] hydrogenase from *Desulfovibrio desulfuricans* (PDB 1HFE). The ferredoxin-like domain and the H-cluster are highlighted on the left and on the right, respectively. All molecular figures were created with the PyMOL Molecular Graphics System. (http://www.pymol.org)

Iron-sulfur clusters are found in a wide range of forms in nature, including [2Fe2S], [3Fe4S], [4Fe4S] and higher order clusters (Figure 2); of these, [4Fe4S] cubane-type clusters are the most abundant.[9] These moieties are formed in proteins via coordination of iron through Cys side chains with bridging inorganic sulfur atoms. In many biological systems, [4Fe4S] clusters are found aligned to create an electron conduit that shuffles electrons to and from the active site.

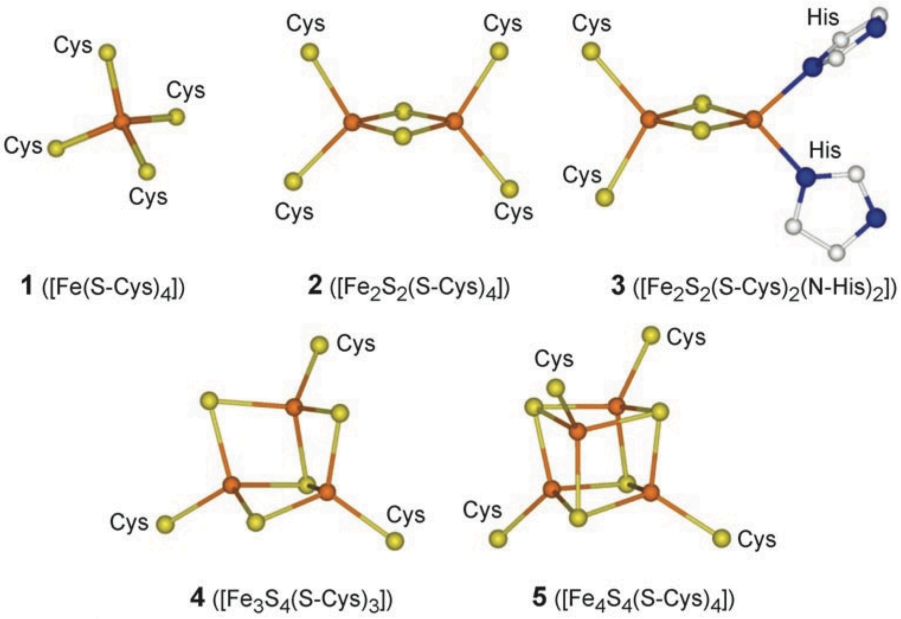

Figure 2: Structures of naturally occurring electron transfer Fe-S clusters. (Figure from ref. 12)

Along with their ability to function as electron transfer modules, iron-sulfur clusters also play a role in other processes, such as catalysis, iron level regulation, and storage, as well as transport of ligands within the cell; they are also used in the

multielectron chemistry of proton reduction, sulfite reduction, and elemental nitrogen reduction.[10, 11] Although the modular clusters perform a number of functions, work preformed by the Ghirlanda group and others for the design of artificial iron-sulfur cluster proteins has focused on the use of iron-sulfur clusters for the purposes of electron transfer.

Despite containing isostructural [4Fe4S] clusters and their derivatives, iron-sulfur proteins exhibit redox potentials ranging from -700 to 450 mV; cubane clusters have been shown to use three different redox states to span such a wide range of potential: $[4Fe4S]^{+3/+2/+1}$.[12] It is believed that the electrostatic environment of amino acids surrounding the cluster, the hydrogen bonding interactions of bridging S-atoms, and the accessibility of the cluster to the solvent influence the potential observed for a particular cluster in a given context. Due to their inherent structural complexity and to the necessity of a proteinogenic environment for existence in nature, a substantial amount of scientific effort has been dedicated to elucidating the structure-function relationship of iron-sulfur proteins in natural as well as de novo designed proteins.[13-15]

Work in natural proteins has not been able to elucidate fully the relationship between structure and iron-sulfur clusters redox potentials. Point mutagenesis work on the well studied ferredoxin proteins and the unique Rieske cluster has given some insight into the mechanisms by which nature has tuned iron-sulfur cluster redox potentials to particular functions.[13, 14, 16] Generally, it has been seen that introduction of positive charges into the proximity of the iron-sulfur clusters

shifts the redox potential more positive, while the opposite holds true for introduction of negative charges. While the charges in proximity to each cluster can greatly affect the redox potential, it is also believed that hydrogen bonding to the polar peptide backbone significantly alters the apparent redox potentials.[13, 17] It has been suggested that it is this hydrogen bonding that differentiates the two types of [4Fe4S] clusters, those that employ a +3 to +2 transition, and those that employ a +2 to +1 transition (HiPiP vs Ferredoxin clusters), as the more hydrogen bonds to ferredoxin clusters allow for stabilization of higher electron density.[18] While much information on the structures and spectroscopic signatures of iron-sulfur clusters has been gleaned through the study of natural iron-sulfur proteins, several factors controlling the redox potential and the assembly of clusters remain unclear. Understanding how the protein structure and sequence modulates the properties of iron-sulfur clusters would have a profound effect on our ability to design complex redox-active proteins with predetermined properties. *De novo* design offers an alternative approach to investigate these factors in simplified model proteins, and it has been used extensively over the last two decades.

Iron-sulfur cluster binding sites have been incorporated into proteins that do not naturally bind this cofactor by using computational methods,[19] or reconstituted into minimalistic sequence motifs derived from natural proteins. Early work on [4Fe4S] binding peptides was based on a conserved CXXCXXC sequence motif found in native cluster binding proteins such as the ferredoxins. It was shown that these peptides can generally incorporate iron sulfur clusters via in situ incorporation, in

which the cluster is believed to form from inorganic precursors with β-mercaptoethanol ligands followed by an entropically driven exchange with the peptide, which acts as a chelating agent and releases the β-mercaptoethanol ligands. These early designs were reviewed recently.[12] Briefly, sequence alignment studies, confirmed by experimental characterization, narrowed the consensus sequence to CIACGAC.[20, 21] In the quest for increased structural and functional complexity, sequences adapted from the minimalistic motif CXXCXXC have been used as loops in helical hairpins. The Dutton laboratory engineered heme-binding maquettes to design a helix-loop-helix motif that coordinates two hemes and one iron-sulfur cluster, and suggested that this motif dimerized into a four-helix bundle. (Figure 3) The redox potential of the cluster, determined via spectroelectrochemical experiments, was −350 mV, which is comparable to that of natural ferredoxins; it appears that the cluster's properties are not affected by the neighboring heme. A few possible models were put forward based on sequence information, and it is quite likely that the protein is a molten globule; no evidence was found for coupling between cofactors.[22]

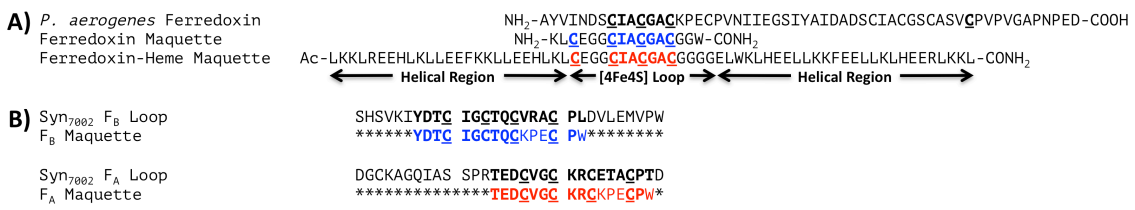

Figure 3: A) Sequence alignment of the *P. aerogenes* ferredoxin with the minimalist peptide and helical bundle used by Dutton, highlighting key structural factors. B) Alignments of the natural binding sequences found in PSI for F_A and F_B with the minimalist maquettes used by Lubitz to mimic their properties.

This concept was adapted to reconstruct bridged metal assemblies based on the A-cluster of carbon monoxide dehydrogenase, which contains a cubane iron-sulfur cluster bridged to a Ni(II) site.[23] Using the ferredoxin consensus sequence, the Holm laboratory designed a series of four peptides that explored different ligand coordination spheres around the nickel. All the peptides bound a preformed cubane cluster with apparent 1:1 stoichiometry, and two of the peptides also bound nickel; it was not possible though to infer structural information from the available spectroscopic data.

Other efforts have focused on modeling the [4Fe4S] clusters found in PSI, which contains three clusters, deemed F_X, F_A, and F_B. The F_x cluster is characterized by a pseudosymmetric arrangement in which the Cys ligands are contributed in pairs by the two subunits of the PsaA/PsaB heterodimer. Scott *et al.*[24] inserted the 10-amino acid consensus sequence CDGPGRGGTC as loops in helical hairpins

designed to pair up into a four-helix bundle, so that the two loops coordinated a cubane cluster at one end of the bundle. The resulting protein displays a redox potential of −422 mV, reflecting the solvent exposed location of the cluster. In contrast, models of the F_A and F_B clusters had remained elusive. Utilizing the consensus binding sequence of CXXCXXCXXXCP found in PSI, Lubitz *et al.* modeled the individual binding sites of both F_A and F_B onto 16 amino acid peptides (Figure 3).[25, 26] After cluster incorporation, the peptides showed similar redox potentials to the natural clusters, at −440 and −470 mV, and also irreversibly bound to PSI.

Recently, a computational methodology that starts from the geometric requirements of the metal was used to design a protein that incorporates an iron-sulfur cluster (Figure 4).[27, 28]The natural symmetry of [4Fe4S] clusters was extended to the four Cys making up the first coordination sphere, and then a four-helix bundle was built around the site. Notably, incorporation of the cluster into their artificial protein stabilizes the overall fold, leading to the conclusion that the designed α-helices are integral in cluster incorporation. The authors subsequently added to this peptide an empirically designed heme binding site. The new model successfully bound both the cluster and heme, although the latter with very low affinity. Throughout this series, however, oligomerization of the helical peptides was a large problem, affecting the functionality of the peptides.

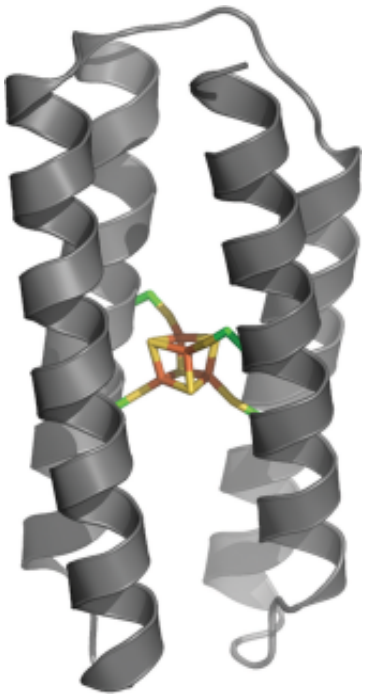

Figure 4: Computational model of a *de novo* designed four-helix bundle coordinating a [4Fe4S] cluster.

The majority of work on iron-sulfur clusters in *de novo* designed peptides has focused on the cubane [4Fe4S] cluster, however there are other types of clusters in nature that are of interest as targets for *de novo* design. Recently, a new type of iron-sulfur cluster was found in the oxygen-tolerant, membrane-bound NiFe hydrogenases.[29, 30] These proximal [4Fe3S] clusters are ligated into the protein via 6 Cys residues, as opposed to the typical 4 or 3 Cys residues seen for other clusters. It has been proposed that these clusters are capable of storing two electrons, via a proton-coupled electron transfer mechanism.[31] Upon reduction of the cluster, the protein undergoes a conformational change during deprotonation of a backbone

amide and removal of the bridging Cys residue.[31] This two-electron chemistry is of great interest to *de novo* peptide design for electron transfer, but has yet to be accomplished in a rationally designed peptide.

Separately, the interconversion of [3Fe4S] and [4Fe4S] clusters in *Desulfovibrio gigas* ferredoxin is linked to hydrogen metabolism, with one isoform of the protein existing as a dimer and coordinating the [4Fe4S] type, and the second isoform associating into a tetramer and coordinating the [3Fe4S] type.[32] The reviewed approaches have been extended recently to the incorporation of the less abundant [3Fe4S] cluster through mutation of a single, ligating Cys residue to a Ser. Mutations in the variable portion of the consensus sequence were shown to modulate the efficiency of cluster incorporation as well as the relative preference for [4Fe4S] vs. [3Fe4S], however the model utilized a relatively unstructured maquette that did not stabilize the clusters sufficiently and no electrochemical analysis was preformed.[15]

The model systems reviewed above were designed to contain a single cubane-type cluster. In nature, however, clusters are often organized in pairs or chains that can be used as electron conduits. To address this problem, our lab has recently developed a general method to design bis-[4Fe4S] cluster binding peptides by exploiting the symmetry of coiled coils (Figure 5).[33] Using this approach, we have shown that two [4Fe4S] clusters can be incorporated inside the hydrophobic core of a three- helix bundle. However, the distance separating the two clusters in our prototype was 36 Å, which did not provide a useful platform for studying efficient

electron transfer. In my work, I will present two second-generation designs: DSD-Fdm, in which the two clusters are located within 12 Å of each other for biologically effective electron transfer, and DSD-3C, in which the cluster specificity was altered from [4Fe4S] to [3Fe4S] through point mutagenesis.

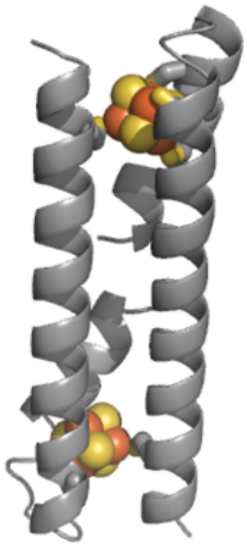

Figure 5: Computational model of DSD-bis[4Fe4S], a *de novo* designed dimeric three-helix bundle protein that coordinates two iron sulfur clusters within its hydrophobic core.

2.2 Materials and Methods

Peptide Synthesis and Purification

All peptides were synthesized by automated microwave-assisted solid phase peptide synthesis on a Liberty instrument (CEM). The synthesis was carried out using standard Fmoc protection procedures. Briefly, Rink amide resin was doubly deprotected using 0.1 M hydroxybenzotriazole (HOBt) in a solution of 20%

piperidine in DMF. Amino acid couplings were achieved using appropriate amounts of 0.45 M N,N,N′,N′-tetramethyl-O-(1H-benzotriazol-1-yl)uronium hexafluoro-phosphate (HBTU) in DMF, 2 M ethyl-diisopropylamine (DIEA) in N-methyl-2-pyrrolidone (NMP), and 0.2 M fluorenylmethyloxycarbonyl (Fmoc) protected amino acid (Novabiochem), followed by irradiation with microwaves to pre-established temperatures according to CEM protocols. Peptides were acetylated at the N-terminus via addition of acetic anhydride under coupling conditions. The peptides were cleaved from the resin using 94% trifluoroacetic acid (TFA), 2.5% H_2O, 2.5% 1,2-ethanedithiol (EDT), and 1% triisopropylsilane (TIS) for 3 h. The solution was then evaporated under a stream of N_2, and the peptide was precipitated with cold ether. Crude lyophilized peptides were purified using preparatory-scale high performance liquid chromatography (HPLC) on a C18 reverse-phase column, with a linear gradient of solvent A (99.9% water with 0.1% TFA) and solvent B (95% acetonitrile, 4.9% water, and 0.1% TFA) at a flow rate of 10 mL/min. Peptide identity was confirmed by matrix-assisted laser desorption ionization time-of-flight mass spectrometry (MALDI-TOF- MS); peptides were >99% pure as assessed by C18 analytical HPLC.

Cluster Incorporation and Quantification

Iron−sulfur clusters were incorporated into peptide variants by adapting well-established methodologies.[26, 34] All reactions were performed in an anaerobic chamber (Coy Scientific), with a 95% N_2 and 5% H_2 environment. To a solution of 150 μM peptide, protein concentration was assessed utilizing the ε_{280} = 5,690 M^{-1}

cm^{-1}, in 100 mM Tris-HCl, pH 8.5, the following reagents were added sequentially at 20 min intervals to a final concentration: 0.8% (v/v) β-mercaptoethanol, 3 mM ferric chloride ($FeCl_3$), and 3 mM sodium sulfide (Na_2S). The mixture was incubated overnight at 4 °C. The resulting dark brown solution was subjected to desalting with a PD10 G25 column (GE Healthcare) that was pre-equilibrated with 100 mM Tris at pH 7.5 to obtain the holo protein.

Cluster Quantification

Cluster incorporation was assessed quantitatively by measuring independently the concentration of iron and of peptide in identical samples.[33] DSD samples were further purified using anion exchange chromatography on a Q-Sepharose FF column (GE Healthcare), using 100 mM Tris at pH 8.5 as equilibration buffer and 100 mM NaCl, 100 mM Tris at pH 8.5 as elution buffer. The DSD-Fdm samples were split in two portions: one was used to measure peptide concentration (Bradford assay), and the second was used to determine iron concentration (ferrozine assay).[35, 36] EPR spin quantification was used to assess the amount of reduced clusters in concentrated EPR samples. The double integral of the CW EPR spectrum of $[4Fe\text{-}4S]^+$ recorded at 7 K was compared with the spectrum of 5 mM Cu(II) nitrate recorded at 21 K (at lower temperatures, the Cu(II) EPR signal saturated even at the lowest accessible MW power of 0.2 μW). The estimated concentration of $[4Fe\text{-}4S]^+$ was then compared with the DSD-Fdm protein concentration evaluated by Bradford assay.

Gel Filtration

Size exclusion chromatography was performed on a G-25 gel filtration column fit to an Agilent Technologies 1260 Insight FPLC system. The column was pre-equilibrated in 100 mM Tris-HCl, pH 7.5, and 200 µL of 150 µM apo or holo peptide were used for each injection. The apo peptide was pretreated with tris(2-carboxyethyl)-phosphine (TCEP) for 30 min before injection to reduce any disulfides resulting from air oxidation.

Circular Dichroism Spectroscopy

Spectra were recorded on a JASCO J-815 spectropolarimeter in the range of 190−260 nm. Data were recorded every 1 nm and averaged over three scans. The concentrations of apo and holo peptides were kept at 50 µM in 100 mM Tris, pH 7.5, while the measurements of the apo peptide were carried out in the presence of an excess of TCEP. Holo peptide was measured under anaerobic conditions in an airtight CD cuvette.

Chemical denaturation titrations were carried out through addition of an 8 M stock solution of guanidinium-HCl (Gdn·HCl), followed by mixing and incubation for 5 min to allow for equilibration. Holo peptide was titrated under anaerobic conditions. Spectra were normalized to protein concentration in the sample and converted to fraction folded relative to the apo or holo protein signal, which lacked Gdn·HCl.

Electron Paramagnetic Resonance Spectroscopy

Holo protein obtained from PD10 desalting was concentrated in a 3000 MWCO centrifuge concentrator to approximately 1 mM peptide concentration. Reduced samples were prepared by addition of 100 mM sodium dithionite in 1 M glycine buffer, pH 10, to a final concentration of 20 mM dithionite. EPR samples were prepared by addition of 10% (v/v) glycerol as a cryoprotectant and placed in quartz EPR tubes, after which the samples were flash frozen and stored under liquid N_2 until measurements. Continuous wave (CW) EPR experiments were carried out on a X-band EPR spectrometer Elexsys E500 (Bruker) equipped with the ESR900 flow cryostat (Oxford Instruments).

Electrochemical Methods

All electrochemical measurements were performed in an anaerobic chamber with a 95% N_2 and 5% H_2 gas mixture. Cyclic voltammetry scans were performed using a CH-instruments 1242B potentiostat with a three-electrode system. Electrodes used were a 3-mm diameter glassy carbon working electrode with a surface area of 0.28 cm^2, platinum mesh counter electrode, and a saturated calomel reference electrode. Potentials were normalized to SHE by addition of 240 mV to the SCE reference values. Buffer solutions were degassed extensively with argon followed by incubation for 2 days in the anaerobic chamber prior to use. Working electrodes were polished with 1 μm alumina for 5 minutes followed by sonication for 10 minutes. Electrodes were also electrochemically cleaned via iterative cycles between 1.2 and -1.2 V vs SCE in 1 M H_2SO_4 followed by extensive washing with water.

Synthesis of Water-Soluble Porphyrin Analogue

The 5,10,15,20-tetrakis(4-diethyl 2-benzylmalonate) porphyrin was synthesized following published procedures for related compounds.[37] Zinc insertion was achieved using $Zn(O_2CCH_3)_2(H_2O)_2$ in THF for 12 h at 60 °C by modifying a literature procedure (Figure 6),[38] and the esters were cleaved as reported for related compounds.[39] The resulting water-soluble, malonate-functionalized porphyrin was characterized by mass spectrometry and NMR in D_2O.

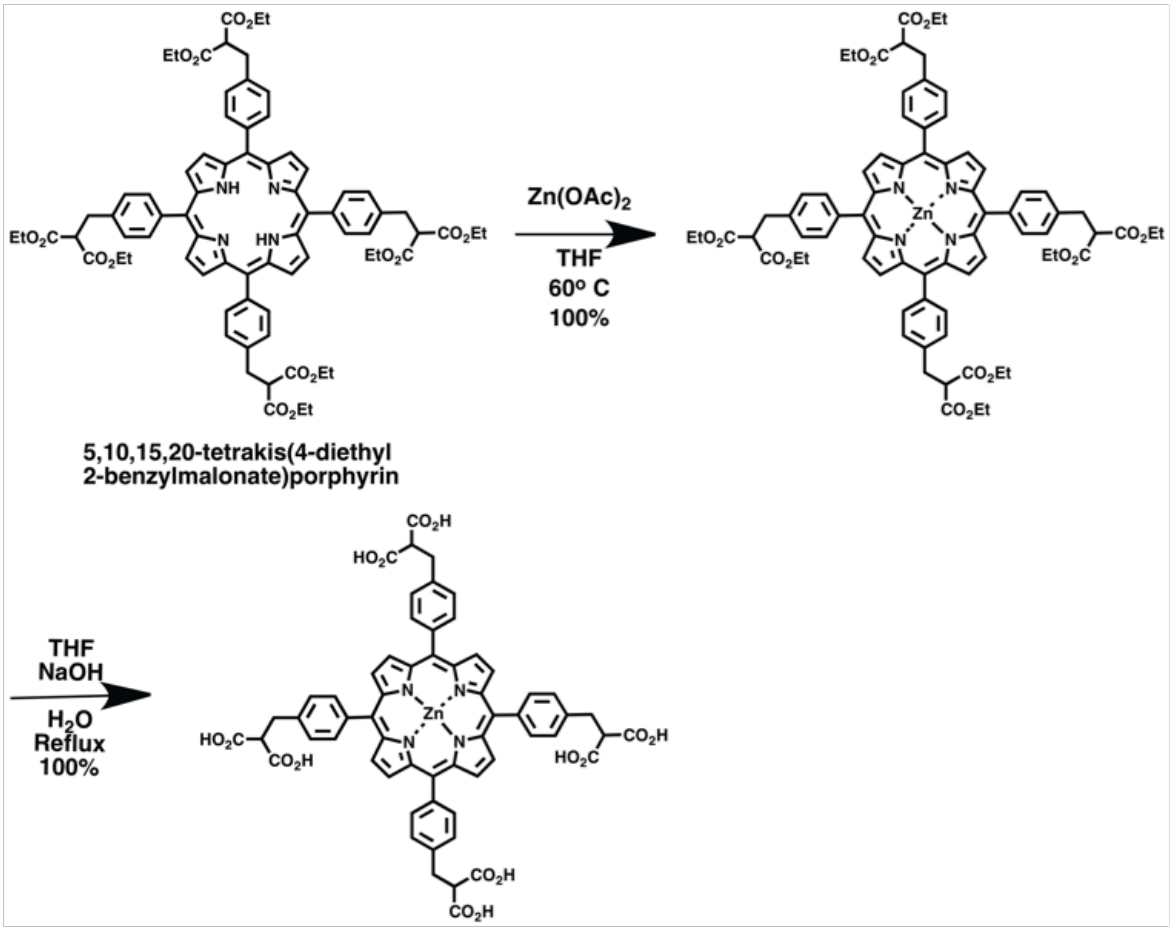

Figure 6: Synthetic scheme for water-soluble porphyrin.

Transient Absorption Spectroscopy

Nanosecond transient absorption measurements were performed on a flash photolysis apparatus using a pulsed laser source and a pump–probe optical setup. The samples contained 10 mM Tris-HCl at pH 7.5 with 30 μM holo or apo peptide in a 1 cm fluorescence cuvette. Malonate-porphyrin was added to a final absorbance of 0.25 at the first Q-band (560 nm). Excitation was provided by an optical parametric oscillator pumped by the third harmonic (352 nm) of a Nd:YAG laser (Ekspla NT 342B). The pulse width was 4–5 ns, and the repetition rate was 10 Hz. The signal was detected by a Proteus spectrometer (Ultrafast Systems). The instrument response function was 4–5 ns. Transient data analysis was carried out using the in-house program ASUFIT. Simple exponentials were fit one wavelength at a time.

Cytochrome c_{550} Reduction Assay

DSD-Fdm was reduced via slow addition of dithionite, monitoring the loss of signal at 410 nm. Once the absorption at 410 nm had stabilized and a slight dithionite signal had arisen at 300 nm, the holo peptide was subjected to two successive PD10 columns to exclude any unreacted dithionite. The first 1.5 mL of the total 3.5 mL elution volume was concentrated to a protein concentration of 300 μM. The reduced DSD-Fdm was added in 1 μL increments to 500 μL of a solution of cytochrome c_{550} isolated from *Thermosynechococcus elongatus* (7 μM protein concentration as assayed by absorbance at 550 nm, ε_{550}= 21000 M^{-1} cm^{-1}). After each addition, UV–vis spectra were obtained with an Ocean Optics USB4000 detector fitted with a USB-ISS-UV-Vis light source. Data were fit by a linear

regression model before and after saturation in order to determine the mole equivalents required to obtain full reduction of the cytochrome c_{550} heme cofactor.

2.3 Modulation of Cluster Specificity

Peptide Design

We have recently adopted a model peptide based on the coiled-coil DSD (domain swapped dimer (PDB 1G6U) peptide, designed by DeGrado and colleagues, as a scaffold to efficiently coordinate two [4Fe4S] clusters within its hydrophobic core.[33, 34, 40] Idealized cluster-binding sites can be engineered at various distances from each other by exploiting the heptad repeat pattern. Due to the internal pseudosymmetry of DSD, the site is replicated on each half of DSD along the longitudinal axis. The sites were introduced into the peptide via docking of the [4Fe4S] cluster-binding site from a *Thermotoga maritima* tRNA synthetase (PDB 2G36)[41] containing the cluster as well as the coordinating cysteine side chains. Briefly, a CXXC motif was engineered on the long helix of DSD and used as first attachment point for the cluster, followed by selection of a single Cys mutation on each of the remaining helices at positions compatible with chelating the [4Fe4S] cluster.

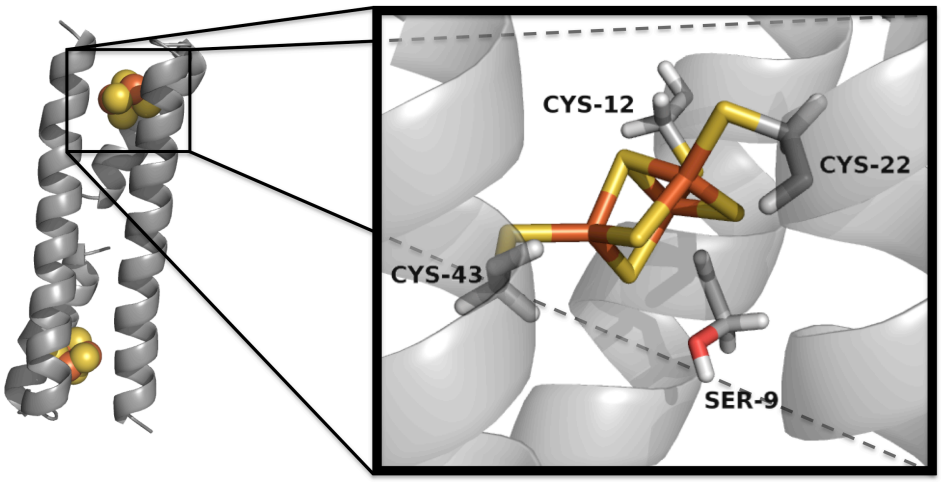


```
DSD            SLAALKSELQALKKEGFSPEELAALESELQALEKKLAALKSKLQALKGW
DSD-2[4Fe4S]   SLAALKSECQACKKEGFSPEECAALESELQALEKKLAALKSKCQALKGW
DSD-3CLeu      SLAALKSELQACKKEGFSPEECAALESELQALEKKLAALKSKCQALKGW
DSD-3CSer      SLAALKSESQACKKEGFSPEECAALESELQALEKKLAALKSKCQALKGW
```

Figure 7: Energy-minimized model of DSD-3C highlighting coordinating Cys residues and position 9, either Ser or Leu for this study (top panel), and sequence alignment of DSD, DSD-2[4Fe4S], and DSD-3C variants.

We set out to alter the specificity of the [4Fe4S] cluster-binding site to [3Fe4S] via mutation of the fourth coordinating Cys. This Cys was either substituted with Leu, which can increase hydrophobic packing around the cluster binding site, or with Ser, which introduces a weakly coordinating ligand in the proximity of the cluster. (Figure 7) Coordination via the alcohol moiety of serine results in increased stabilization of the [3Fe4S] cluster in both natural and designed proteins, although in all cases the majority of protein still contains the thermodynamically more stable [4Fe4S] type upon *in vitro* incorporation.[15, 42] The robust nature and fold of the DSD

peptide, though, may provide a more structured environment around the cluster binding site and lead to preferential incorporation of the [3Fe4S] cluster.

Cluster Incorporation

Clusters were readily incorporated into both scaffolds following well-established methodologies utilizing *in situ* incorporation followed by purification via size exclusion chromatography from the excess inorganic precursors. The UV-vis spectra of both the Ser and Leu variants exhibited broad absorbances centered around 320 and 420 nm, features characteristic of metal-ligand charge transfers in all iron sulfur cluster proteins. (Figure 8) The ratio of absorbance at 420 to that at 280 nm is often used in natural ferredoxins to assay purity and cluster content of the sample. In agreement with both natural samples and previously designed constructs, the ratio of the DSD-3CSer and DSD-3CLeu consistently fell between 0.75 and 0.8 on multiple, independent preparations. This ratio indicates an approximate 1:1 cluster to peptide ratio, with both peptides exhibiting high yields of incorporation. These features are red-shifted compared to synthetic models of iron-sulfur clusters, resulting from the solvent-shielded state of the clusters. The UV-vis spectra of [3Fe4S] and of [4Fe4S] are nearly indistinguishable, though, and thus no information on the identity of the clusters was obtained. Upon reduction of the peptides with an excess of sodium hydrosulfite, the absorbances of these bands reduced to less than 50% of their initial values, indicative of a change of oxidation state in the clusters from Fe^{3+} to Fe^{2+}.

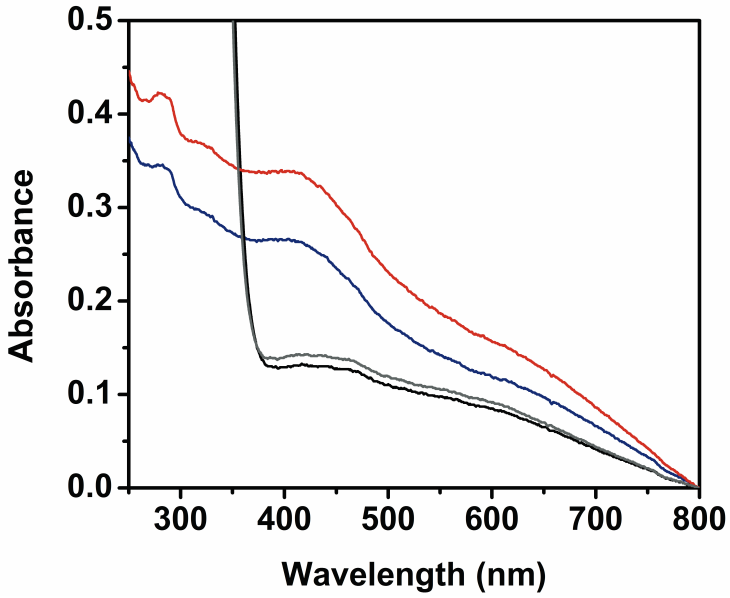

Figure 8: UV-Vis spectra before and after dithionite reduction of DSD-3CSer (blue oxidized, black reduced) and DSD-3CLeu (red oxidized, gray reduced).

The spectra obtained resemble previous work on this family of peptides, indicating that the clusters are incorporated correctly and are housed within the hydrophobic interior of DSD. Cluster incorporation was quantified more accurately by independently measuring iron content and protein concentration on the identical samples of holo peptide. A typical quantification yielded 3.42 and 4.19 Fe/monomer for the DSD-3CLeu and DSD-3CSer mutants, suggesting that the proteins incorporated a mixture of [3Fe-4S] and [4Fe-4S] clusters.

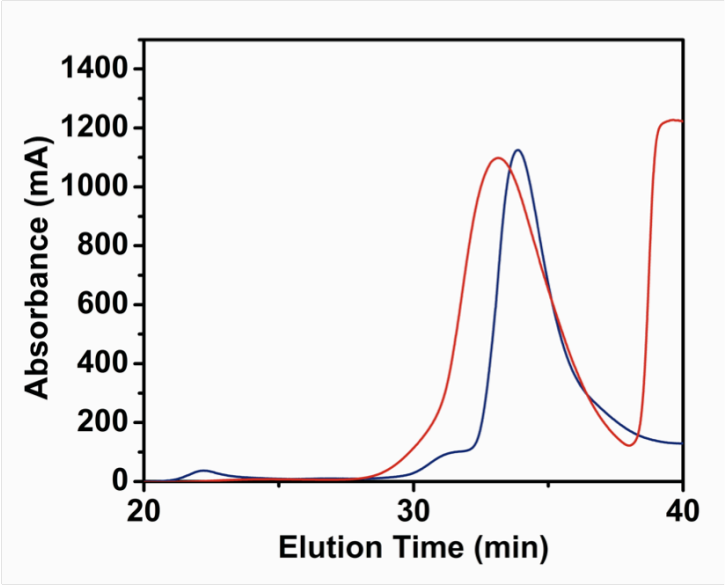

Figure 9: Gel filtration chromatograms of apo DSD-3CSer (red) and apo DSD-3CLeu (blue). Data were obtained on a G-25 gel filtration column in 100 mM Tris-HCl, pH 7.5. Apo peptide samples contained 50 molar excess of TCEP, which elutes in a peak at 40 min.

The secondary structure and oligomerization state of the peptides were assayed by far-UV circular dichroism and gel filtration chromatography, respectively. The oligomerization states of the apo peptides were verified at the concentrations utilized for cluster incorporation (100 μM) at which we expected all samples to elute as dimers. The apo-peptide samples yielded a single peak at elution volumes corresponding to the dimer, as monitored by absorbance at 220 and 280 nm. (Figure 9)

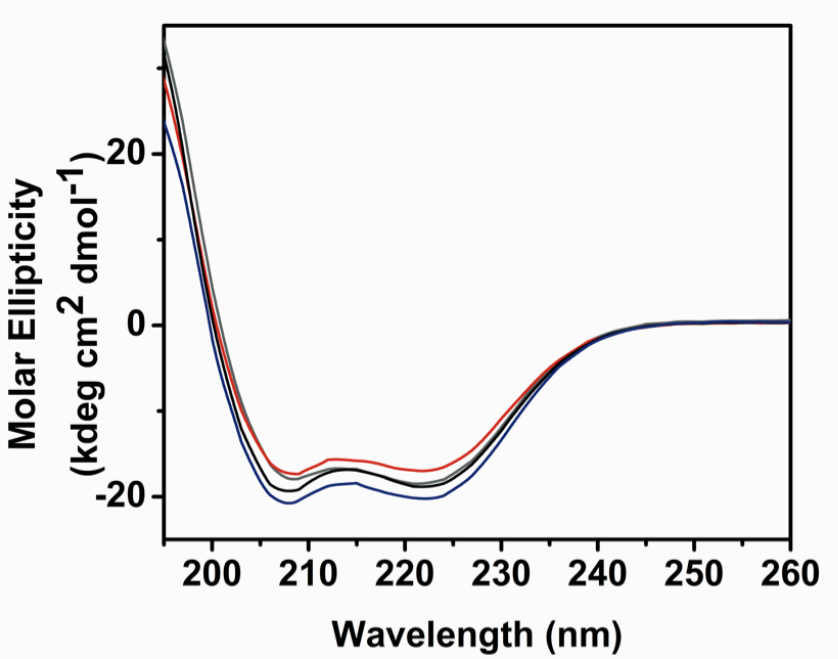

Figure 10: CD spectra of apo DSD-3CSer (black), apo DSD-3CLeu (gray), holo DSD-3CSer (blue), and holo DSD-3CLeu (red). Peptides were at 50 μM concentration in 10 mM Tris-HCl pH 7.5. Apo peptide samples contained excess TCEP.

Similar to the parent peptide, both DSD-3CLeu and DSD-3CSer have a high α-helical content, as shown by the presence of two minima in the CD spectra at 208 and 222 nm. (Figure 10) Upon cluster incorporation the position and strength of these signals are relatively unaltered, indicating that the presence of the cluster does not significantly alter the secondary structure of the peptides at room temperature.

In order to assess the impact of core mutations and cluster incorporation on protein stability, we monitored the loss of secondary structure as a function of

denaturant concentration, utilizing the chaotropic agent guanidine hydrochloride (Gdn•HCl). (Figure 11) Analysis of the denaturation isotherms reveals apparent

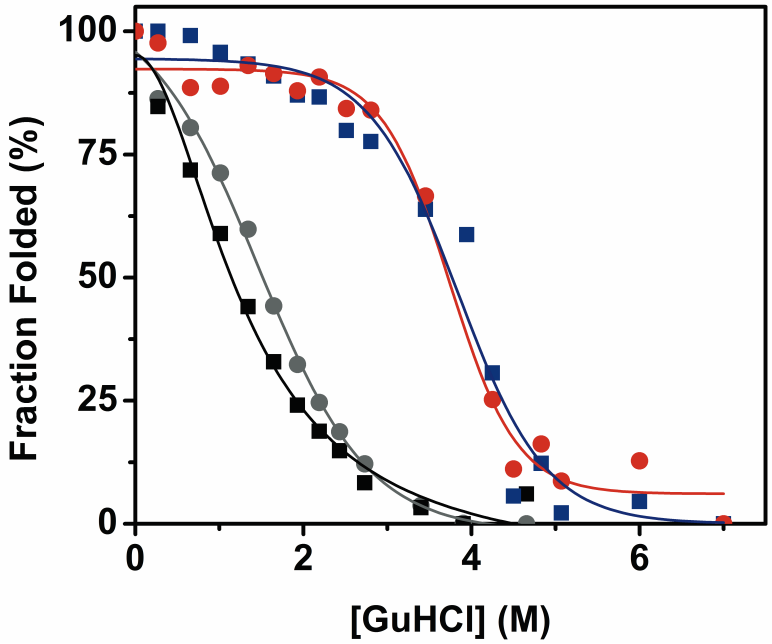

Figure 11: Chemical denaturation of 50 µM apo and holo DSD-3C variants as monitored by CD at 222 nm. Traces correspond to apo DSD-3CSer (black squares), holo DSD-3CSer (blue squares), apo DSD-3CLeu (gray circles), and holo DSD-3CLeu (red circles).

midpoints at 1.6 M for DSD-3CSer and 1.8 M for DSD-3CLeu. Loss of stability upon mutation of core Leu to Cys had been observed for both DSD-bis[4Fe4S] and for DSD-Fdm, reflecting the formation of a cavity in the protein core and the burial of hydrophilic moieties. The difference in stability between DSD-3CLeu and DSD-3CSer reflects the difference in hydrophobicity between the two residues, and is consistent

with the impact of hydrophobic to polar substitution observed in the parent peptides. Upon inclusion of the clusters into the binding pockets, the denaturation isotherms are nearly identical for the two mutants, with midpoints shifting to 3.9 M. This large increase in secondary structure stability results from reconstitution of the core packing of the peptide, as the size of iron sulfur clusters matches closely the size of the binding pocket in the hydrophobic core of the peptide.

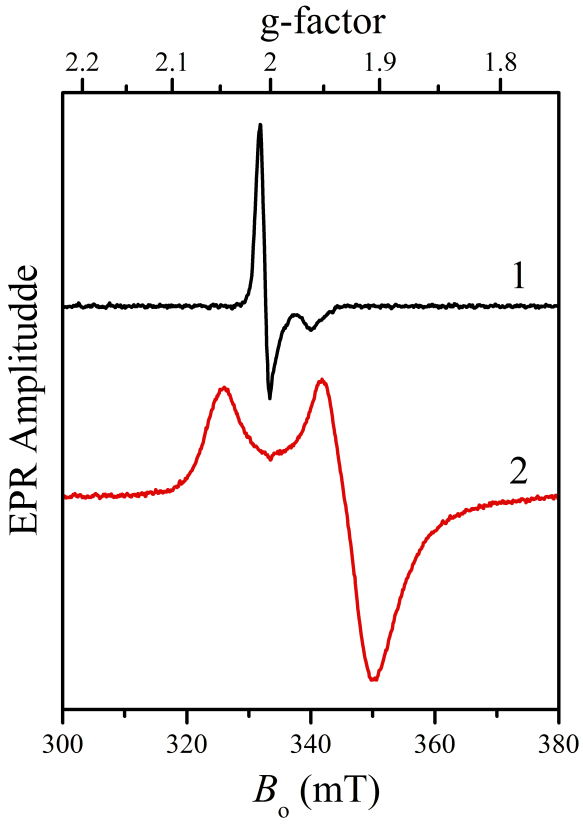

Figure 12: CW EPR spectra of non-reduced (trace 1) and dithionite-reduced (trace 2) DSD-3CSer. Experimental conditions: microwave frequency, 9.336 GHz; microwave power, 2 mW; magnetic field modulation amplitude, 0.5 mT; temperatures, 25 K (trace 1) and 12 K (trace 2)

We determined the presence and the identity of the clusters incorporated in DSD-3CLeu and DSD-3CSer by EPR, as the two types of clusters present distinctive spectroscopic signatures. The EPR spectrum of non-reduced DSD-3CSer (trace 1 in Figure 11) shows a narrow signal with weak g-anisotropy ($g_{\wedge}$ = 2.005, $g_{//}$ = 1.962) characteristic of $[3Fe4S]^{1+}$ cluster, while the reduced protein (trace 2 in Figure 12) shows a significantly more broad signal with the turning points at (g_1, g_2, g_3) = (2.048, 1.932, ~1.892) that is typical of $[4Fe4S]^{1+}$ clusters. The EPR spectra of reduced and non-reduced DSD-3CLeu display identical features.(Figure 13) Spin quantification of these signals against a 5 mM Cu(II) nitrate reference sample revealed that the concentration of the $[3Fe4S]^{1+}$ cluster in the non-reduced samples was between one and two orders of magnitude smaller than that of the $[4Fe4S]^{1+}$ cluster in the reduced samples.

Typical values for reduced samples, corresponding to [4Fe4S] clusters, are 27.5 ± 2.5 mM for DSD-3CSer and 8 ±1 mM for DSD-3CLeu. Non-reduced samples, corresponding to [3Fe4S] clusters, were quantified as 0.5 ± 0.1 mM for DSD-3CSer and 0.2 ±0.04 mM for DSD-3CLeu. The yield of incorporation of [3Fe4S] clusters decreased slightly with increasing incubation times. It appears that polar interactions in DSD-3CSer result in more effective stabilization of cluster incorporation, although DSD-3CLeu contains a higher percent of [3Fe4S] cluster. Lower overall cluster incorporation may be due to increased steric bulk of Leu compared to Ser. Comparison with the protein concentrations determined as described in Methods shows that the [3Fe4S] and [4Fe4S] cluster signals

correspond to approximately 5-10% of the total protein concentration. We note that in the case of DSD-bis[4Fe4S] spin quantification also resulted in underestimating the yield of incorporation. The discrepancy between the high incorporation yields seen by UV-vis and the relatively low yields determined by EPR spin quantification can be explained by two factors. The low concentration of paramagnetic $[4Fe4S]^{+1}$ state in reduced samples could result from a shift in the second cluster's redox potential when one of the clusters is reduced. Secondly, EPR sample preparation conditions vary widely in the literature, and may affect signal intensity of the clusters.

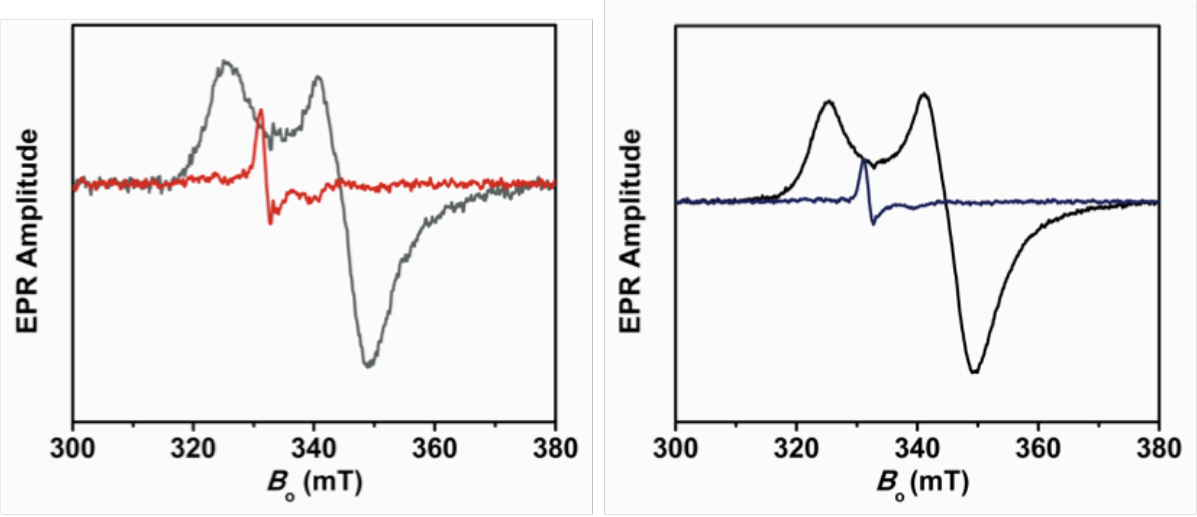

Figure 13: CW EPR spectra of DSD-3CLeu (gray reduced, red oxidized) and DSD-3CSer (black reduced, blue oxidized), indicating cluster preference after incorporation.

We measured the reduction potentials of the two holo proteins by bulk solution cyclic voltammetry in the presence of neomycin, which stabilizes the contacts between the peptide and the electrode surface. Due to the large potential window in which $[4Fe4S]^{2+/1+}$ and $[3Fe4S]^{1+/0}$ couples are found, wide scan windows were initially employed to probe the response of both types of clusters. In analogy to the behavior of DSD-bis[4Fe4S], an electrochemically irreversible wave appeared at 445 mV and 395 mV vs SHE for DSD-3CSer and DSD-3CLeu. (Figure 14)

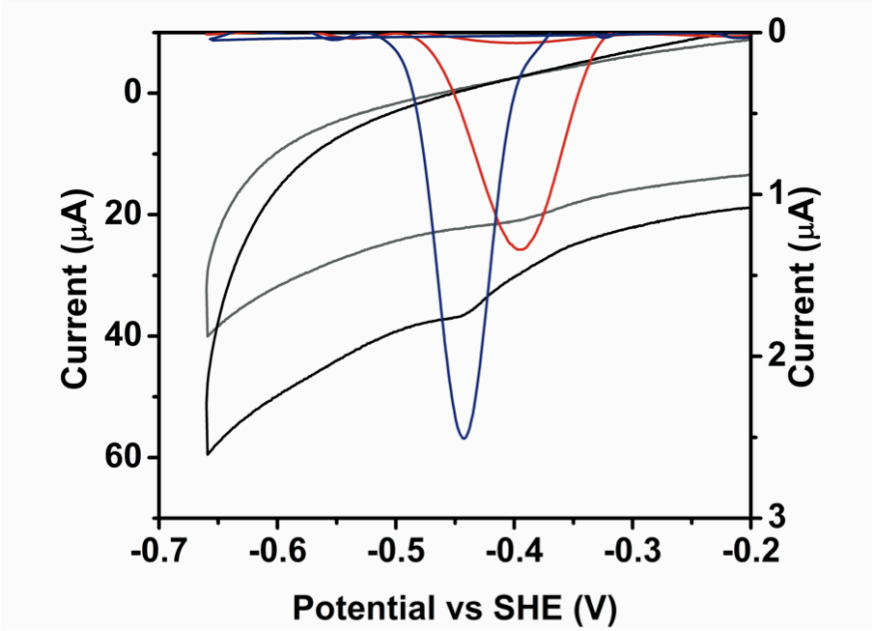

Figure 14: Cyclic voltammograms before and after baseline subtraction of DSD-3CSer (black/blue) and DSD-3CLeu (gray/red).

This wave is ~60 mV positive of the potential observed when the cluster is ligated in place by 4 Cys residues, as in DSD-Fdm and DSD-bis[4Fe4S] where the potentials are

-479 and -478 mV, respectively. The redox potential of metal clusters is generally modulated by two main factors, first the hydrophobic environment as oxidation results in increase in positive charges, which become electrostatically destabilized in hydrophobic environments. The second factor is the presence of hydrogen bond donors, as the presence of a slight positive charge stabilizes interactions with the reduced form, favoring reduction. Mutation of the fourth Cys residue to its more hydrophobic counterpart Leu, generally results in shifting the cluster potential in the positive direction. Mutation to Ser introduces a possible hydrogen bond donor, stabilizing the reduced state of the cluster.[5] The potentials observed align well with single [4Fe-4S] cluster ferredoxins, as in the designed peptide the two incorporated clusters are electronically isolated (albeit weakly magnetically coupled).

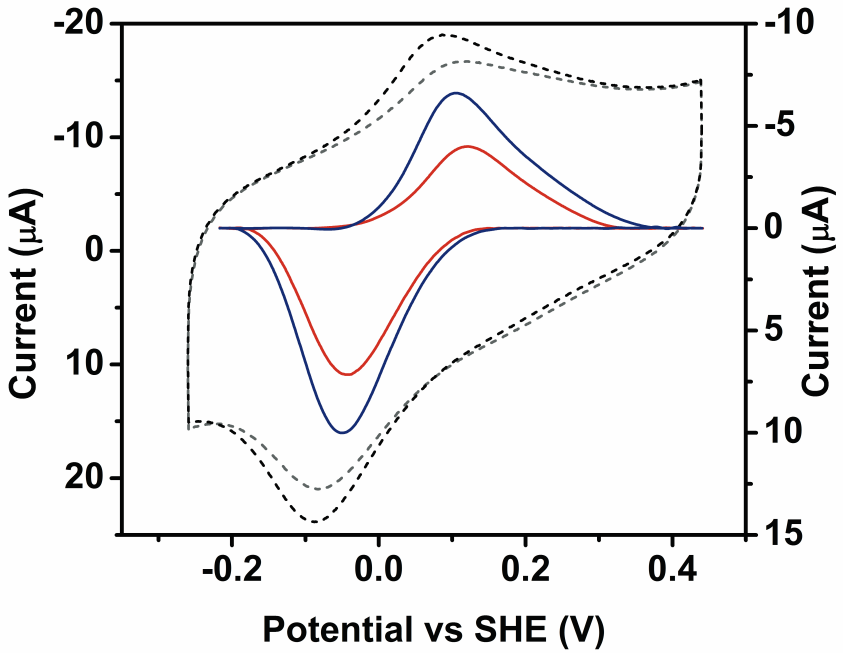

Figure 15: Cyclic voltammograms before and after baseline subtraction of DSD-3CSer (black/blue) and DSD-3CLeu (gray/red).

Additionally, a new reversible wave appeared at higher potentials relative to that of the [4Fe4S] cluster, corresponding to the $[3Fe4S]^{2+/1+}$. (Figure 15) At pH 8, the potentials of this new wave were assigned to be 12 mV and -4 mV for DSD-3CLeu and DSD-3CSer, falling slightly positive of potentials seen for ferredoxins with single [3Fe4S] clusters.[14] As seen with the [4Fe-4S] cluster potential, the Leu variant has an approximate 20 mV shift positive of the Ser variant due to the hydrophobic nature of the side chain, but lack of hydrogen bonding stabilization.

The results presented here show that switching the identity of one Cys ligand to Leu or Ser favors incorporation of [3Fe4S] clusters over the thermodynamically stable [4Fe4S] clusters in a *de novo* designed iron-sulfur cluster binding protein, DSD-bis[4Fe4S]. The two variants, DSD-3CSer and DSD-3CLeu, exhibit similar stability to chemical denaturation; in both cases, incorporation of iron-sulfur clusters results in increase in protein stability. In contrast with previous work on peptides derived from DMSO reductase subunit B (DmsB), which showed incorporation only when a coordinating Cys is exchanged with polar residues, cluster incorporation proceeds readily in both cases. Here, we show that the type of cluster and its redox potential can be modulated by single-point mutations, thus expanding the possible applications of *de novo* designed iron-sulfur proteins as electron transfer modules.

2.4 Characterization as an Electron-Transfer Peptide

We used the heptad repeat pattern of coiled coils, which is reflected in a regular structural motif, to design two [4Fe4S] binding sites into the core of DSD-Fdm starting from DSD-bis[4Fe4S].[33, 34] Each site was translated by one heptad toward the center of DSD along the longitudinal axis (PDB code 1G6U) by moving the two cysteine side chains arranged at the i, i+3 positions within the same helix. Locations for the two remaining cysteines, one per helix, in positions compatible with chelating the cluster were determined by manually docking a [4Fe4S] cluster binding site from *Thermotoga maritima* (PDB ID 2G36) inside the core (Figure 16). Taking into account the pseudo-2-fold symmetry of DSD, we replicated the site onto the other half of DSD by inserting appropriate mutations into the peptide sequence. DSD-Fdm thus incorporates two [4Fe4S] clusters in the hydrophobic core at a distance of 12 Å, as measured between their centers, in an arrangement reminiscent of the symmetry observed in the natural ferredoxin fold. Mutation of eight core leucine side chains to cysteines causes the formation of a 62 $Å^3$ polar cavity within the core of the apo peptide, which is completely filled upon incorporation of the cluster (Figure 16).[43, 44]

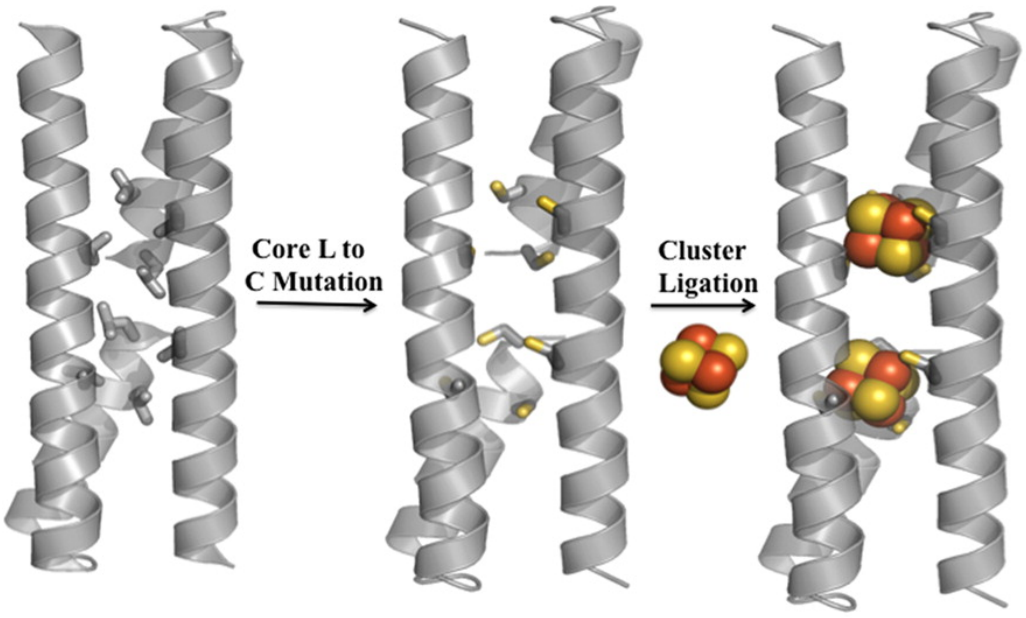

DSD	SLAALKSELQALKKEGFSPEELAALESELQALEKKLAALKSKLQALGW
DSD-2[4Fe-4S]	SLAALKSECQACKKEGFSPEECAALESELQALEKKLAALKSKCQALGW
DSD-Fdm	SCAACKSELQALKKEGFSPEELAALESECQALEKKCAALKSKLQALGW

Figure 16: Design strategy for DSD-Fdm (top panel) and sequences of DSD, DSD-2[4Fe4S], and DSD-Fdm (bottom panel).

The [4Fe4S] clusters were formed and incorporated in situ from inorganic precursors and mercaptoethanol using established protocols, and holo DSD-Fdm was purified by gel filtration chromatography.[45-48] The UV–vis spectrum of DSD-Fdm shows a broad feature with maxima at 415 and 360 nm, characteristic of sulfur to iron charge transfer excitations in $[4Fe4S]^{2+}$ clusters; the absorbance at 415 nm was reduced to below 50% of its initial value upon reduction to $[4Fe4S]^{+}$ (Figure 17) with dithionite. This behavior is typical of cuboidal [4Fe4S] clusters.[49-55] The position of the bands, red-shifted compared with inorganic [4Fe-4S] clusters,

suggests that the clusters are surrounded by a hydrophobic environment.[19, 22-24, 26-28, 45, 54, 56]

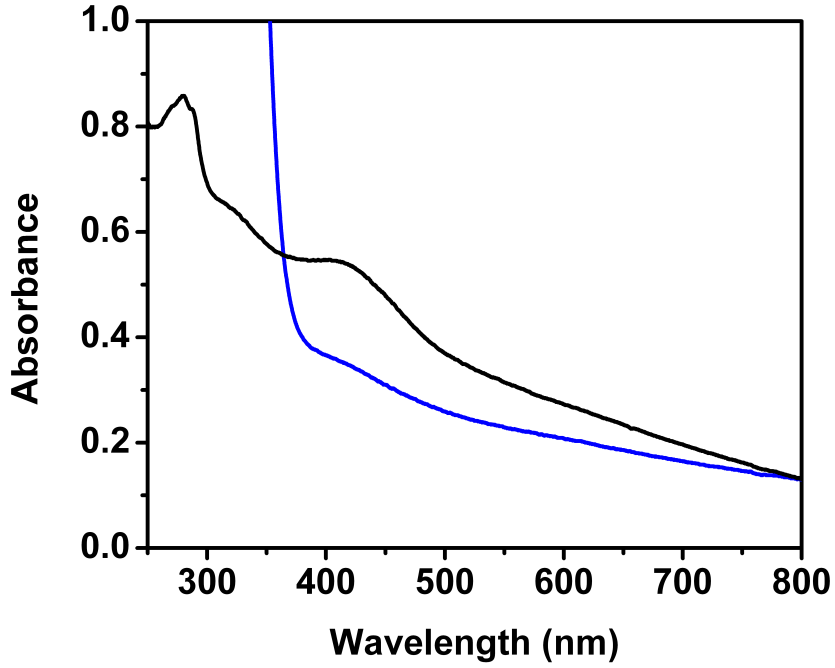

Figure 17: UV–vis spectra of holo DSD-Fdm before (black trace) and after (blue trace) dithionite reduction.

We investigated the oligomeric state of apo and holo DSD- Fdm by analytical ultracentrifugation and size exclusion chromatography. When analyzed by gel filtration, both apo and holo DSD-Fdm elute at comparable volumes of elution buffer, which is consistent with a single species with the apparent molecular mass of a dimer (Figure 18). The elution profiles of the holo DSD-Fdm monitored at 220, 280, and 410 nm are identical, indicating the presence of the [4Fe4S] cluster in the

dimer. Analytical ultracentrifugation of the apo DSD-Fdm at ~100 μM loading concentration reveals an apparent molecular weight in solution of approximately 13.3 kDa, consistent with a dimeric form in solution (Figure 19), confirming the results of the size exclusion chromatography.

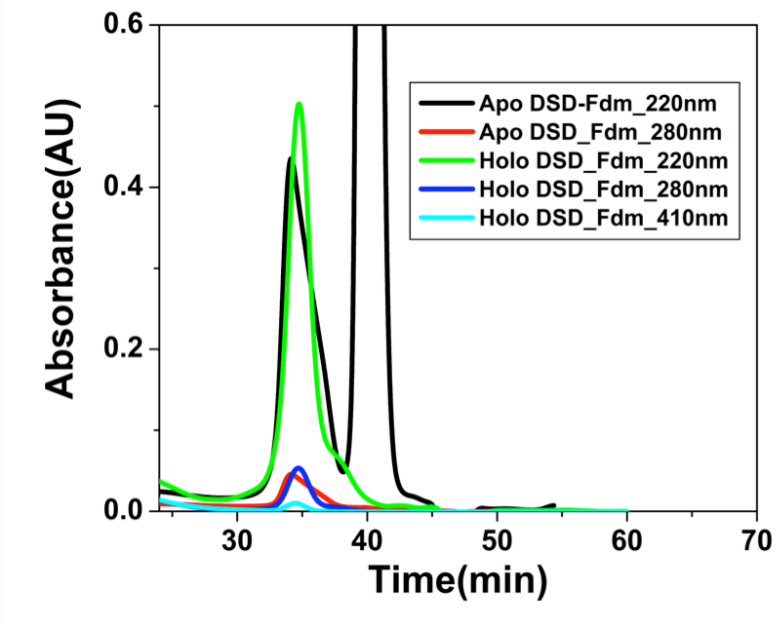

Figure 18: Gel filtration chromatograms of apo DSD-Fdm and holo DSD-Fdm, with corresponding wavelengths in legend. Data were obtained on a G-25 gel filtration column in 100 mM Tris-HCl, pH 7.5. Apo peptide samples contained 50 molar excess of TCEP, which elutes in a large peak centered around 40 minutes (black trace).

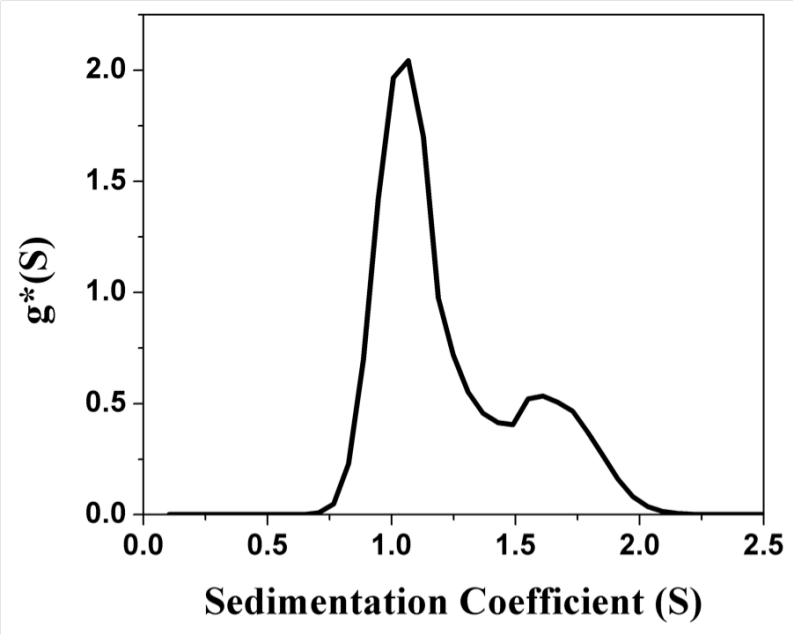

Figure 19: Analytical ultracentrifugation of 100 μM apo DSD-Fdm, indicating a majority species with a MW of 13.3 KDa.

We evaluated the level of cluster incorporation in the dimer by independently assessing Fe and protein concentrations as described in Methods. We found that the ratio of iron per monomer is 4.3 ± 0.9, corresponding to two [4Fe4S] clusters per dimer. These data indicate that incorporation is approximately 100%.

We investigated the secondary structure of both apo and holo DSD-Fdm using far- UV circular dichroism (CD) spectroscopy. The spectra of each of the two proteins are similar to that of the parent peptide and display two minima centered at 208 and 222 nm, indicative of helical structures (Figure 20). Cluster incorporation is well tolerated by the peptide, which is reflected by the similar molar ellipticity value of the holo peptide compared with the apo peptide.

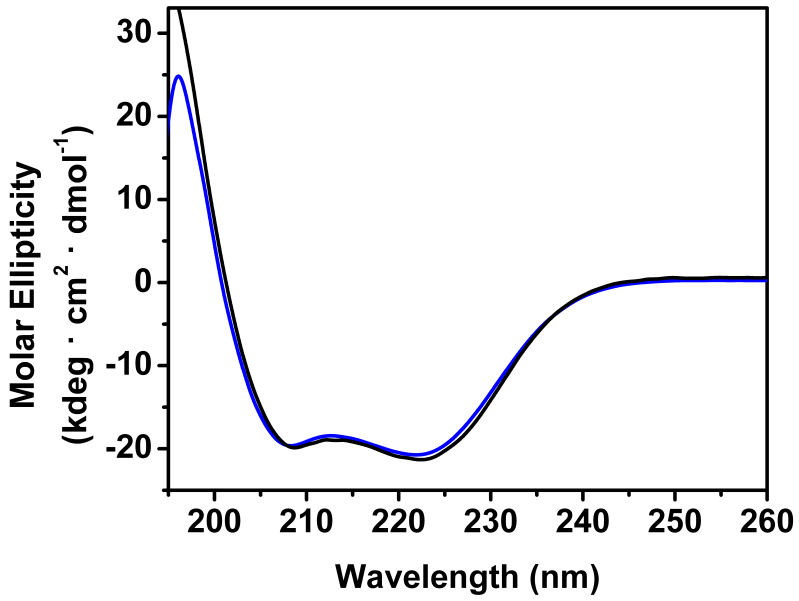

Figure 20: CD spectra of apo (black) and holo (blue) DSD-Fdm in the far-UV range showing two minima at 222nm and 208nm. Proteins were at 50 μM in 10 mM Tris-HCl, pH 7.5. Apo peptide contained a 50 molar excess of TCEP.

To assess the effect of mutations on the DSD framework, we measured the stability of the apo and holo peptide toward chemical denaturation by monitoring the loss of secondary structure as a function of increasing concentration of a chaotropic agent, guanidine hydrochloride (Gdn·HCl). The denaturation curves in Figure 21 report fraction folded, as monitored at 222 nm, versus denaturant concentration for each peptide, showing that holo DSD-Fdm is significantly more stable to chemical denaturants than is the apo version. The midpoint of denaturation for the apo peptide is at 2.1 M Gdn· HCl, while for the holo DSD-Fdm, it is at 4.4 M Gdn·HCl. This behavior mirrors what is observed for DSD-bis[4Fe-4S], for

which a large increase in stability resulted from the cluster incorporation.[33] The starting scaffold for both constructs, DSD, is exceptionally stable to thermal and chemical denaturation.[26, 34] In both DSD-bis[4Fe4S] and DSD-Fdm, substituting hydrophobic leucine residues in the core with polar, smaller cysteines results in the formation of a polar cavity, which in the case of DSD-Fdm has a volume of 62 Å^3. This volume is compatible with the dimensions of a [4Fe4S] cluster; when modeled in the peptide core, the [4Fe4S] cluster completely fills the cavity, thus restoring a well-packed core.

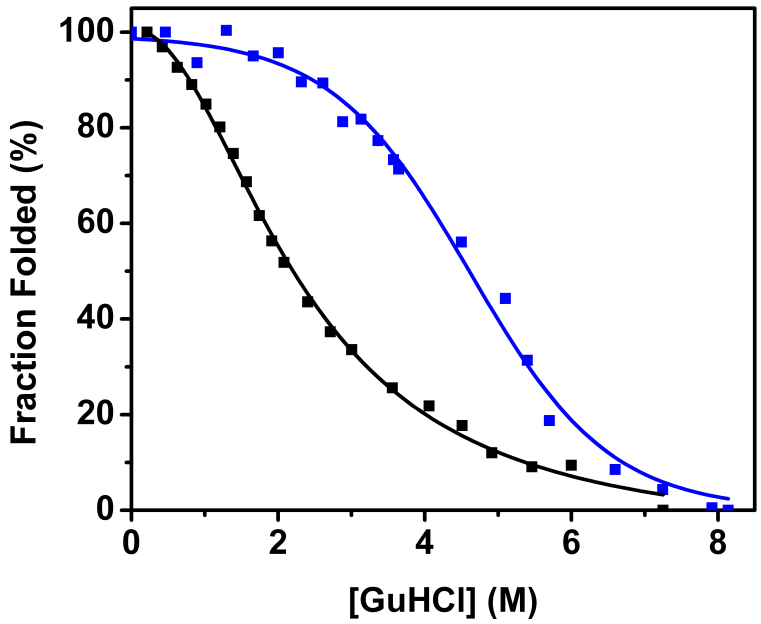

Figure 21: Chemical denaturation profile of 50 μM apo and holo DSD-Fdm monitored by CD at 222 nm. The midpoint of the transition is at 2.1 M Gdn·HCl (black line) for the apo peptide and at 4.4 M Gdn·HCl (blue line) for holo DSD-Fdm.

The electronic properties of holo DSD-Fdm were explored by CW EPR spectroscopy. As expected, in vitro reconstitution of the iron–sulfur cluster into the designed protein results in formation of an EPR silent $[4Fe4S]^{2+}$ resting state. Upon dithionite reduction, an EPR signal corresponding to intact $[4Fe4S]^{+}$ clusters arises, with typical principal g-values of 1.89, 1.94, and 2.06, and an isotropic g-value of about 1.96 (Figure 22). The temperature dependence of this signal is similar (if not identical) to that obtained earlier for DSD-bis[4Fe-4S] and indicative of the presence of low-lying (~60 K) excited states (Figure 23). The spin quantification of this signal and the comparison of the spin count with the protein concentration reveals a yield of reduced cluster per dimer of DSD-Fdm close to 0.6, similar to what has been observed for DSD-bis[4Fe-4S].[33] This value contrasts with complete cluster incorporation yields calculated by iron quantification based on resting state (i.e., oxidized) samples. The discrepancy is caused by difficulties in achieving complete reduction of the cluster in concentrated samples.

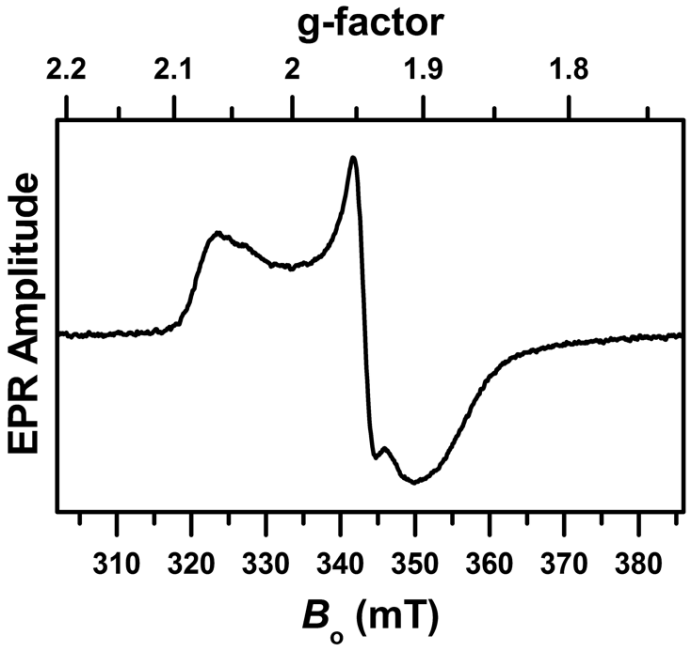

Figure 22: CW EPR spectrum of dithionite-reduced holo DSD-Fdm. Experimental conditions: microwave frequency, 9.337 GHz; microwave power, 20 mW; field modulation amplitude, 0.5 mT; temperature, 12 K

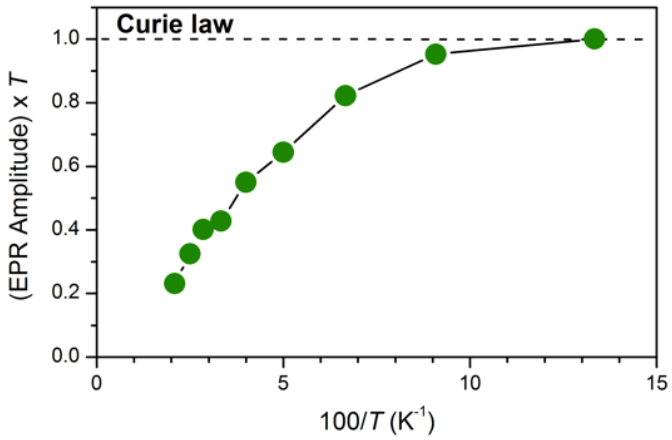

Figure 23: Temperature dependence of the EPR amplitude under non-saturating conditions (mw power, 0.2 μW). The horizontal line corresponds to the temperature dependence described by the Curie Law (no low-lying excited states).

Ferredoxin-type proteins containing two $[4Fe4S]^{1+}$ within 10–15 Å of each other sometimes exhibit features in the EPR spectra attributable to a spin–spin interaction between the clusters.[35, 57] Despite repeated attempts, these features were not observed in the spectra of DSD-Fdm. However, the lack of cluster interaction effects in the CW EPR spectra of dicluster ferredoxins is relatively common, for two main reasons. First, the magnitude of the dipole and exchange interactions between two clusters strongly depends on their relative orientation, because of the mixed valence nature of the clusters.[38, 58] For example, the dipole interaction constant estimated for DSD-Fdm as a function of the relative orientation of the clusters can be anywhere between ~300 and 25 MHz (in magnetic field units, ~11 and <1 mT, respectively) or distributed within these limits. The smaller of these couplings would probably not be detectable because it is much smaller even than the EPR line width at the intermediate turning point (>3 mT). The larger of these couplings could in principle be resolvable, but the relatively flexible nature of DSD-Fdm may result in a significant broadening and the lack of pronounced features in the EPR spectrum of the pair. The second reason, which compounds the first one, is the relatively low yield of reduced cluster.

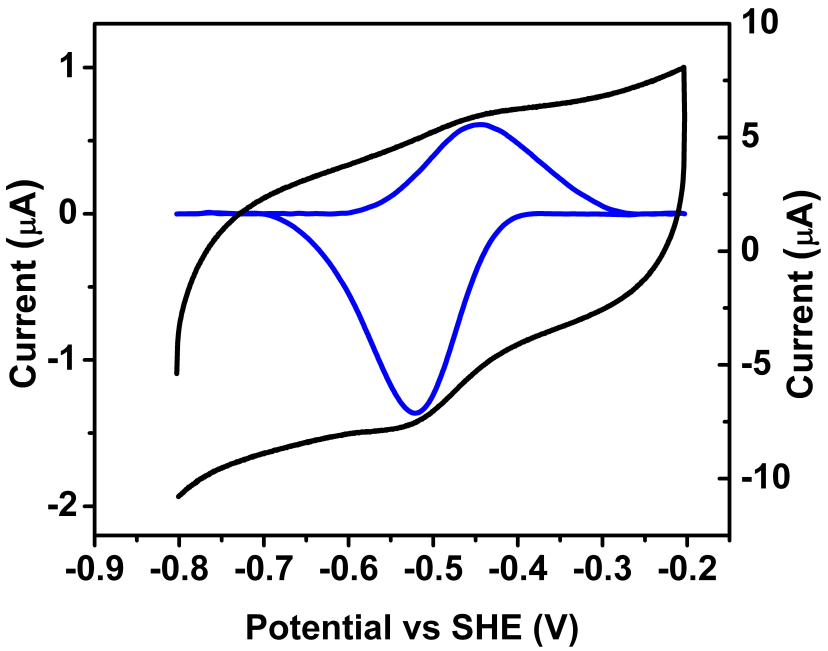

Figure 24: Cyclic voltammogram of DSD-Fdm in a 3.5 mM neomycin, 100 mM Tris, 100 mM sodium chloride, pH 7.5, solution at 100 mV/s scan rate with a Ag/AgCl reference electrode, glassy carbon working electrode, and platinum mesh counter electrode.

The redox properties of DSD-Fdm were probed using cyclic voltammetry (CV). Solution CV experiments showed no observable redox processes in the range from 0 to −1 V vs SHE, presumably because of the absence of interaction between the electrode surface and the electroactive species. Addition of 3.5 mM neomycin, which is known to stabilize and enhance the interaction of ferredoxin type proteins with electrode surfaces, resulted in the observation of a quasi-reversible process with cathodic and anodic waves centered around −0.438 and −0.521 V vs SHE,

respectively (Figure 24). We estimated a redox potential of −0.479 V vs SHE, consistent with the presence of a $[4Fe4S]^{2+/1+}$ couple. This value falls within the window expected for low potential [4Fe4S] clusters in proteins and is very close to those observed for the PsaC subunit of photosystem I.[26, 39, 54, 59]

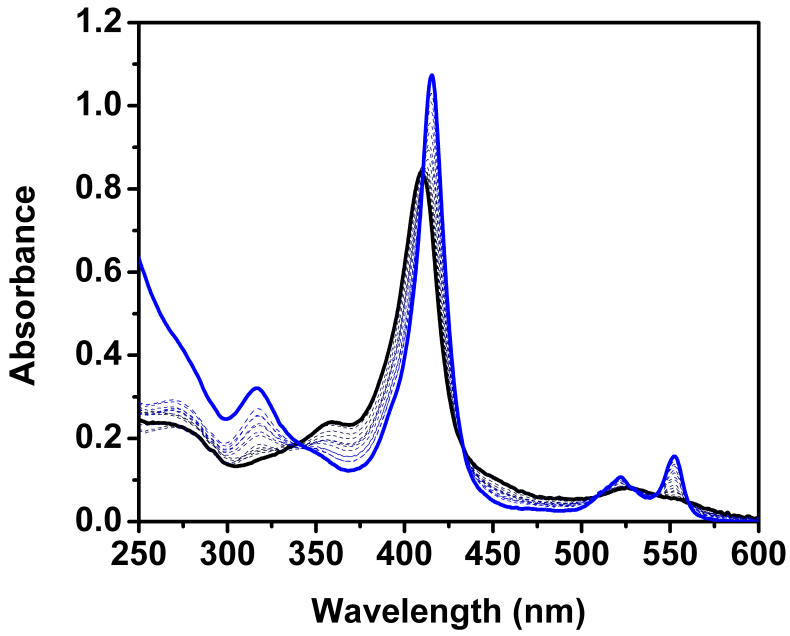

Figure 25: Reduction of cyt c_{550} by DSD-Fdm: UV–vis monitored titration of reduced 300 µM DSD-Fdm to a solution of 7 µM air-oxidized cyt c_{550} in 100 mM Tris, pH 7.5.

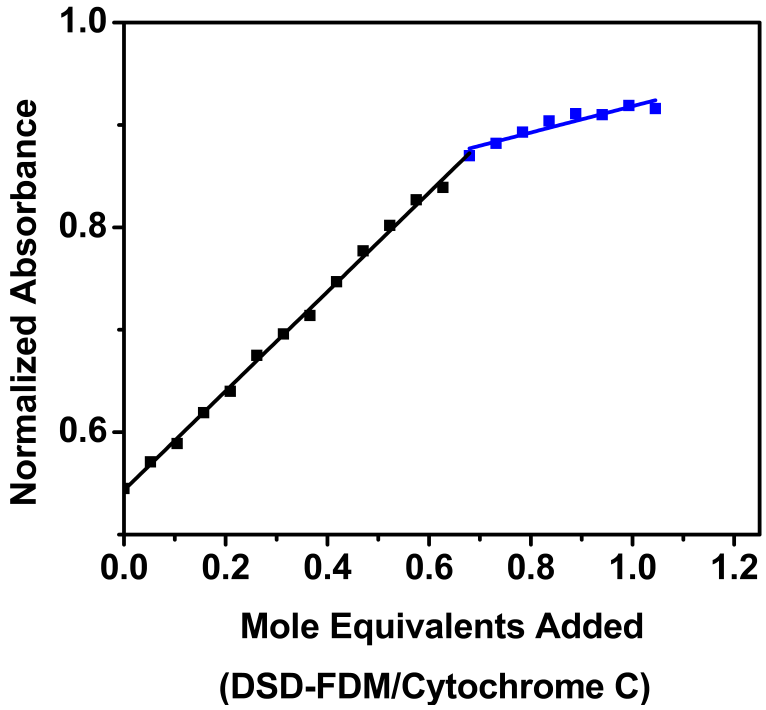

Figure 26: Change in absorbance at 415 nm as a function of molar equivalents DSD-Fdm added during the reduction of cytochrome c_{550}. Values were normalized to isobestic point of the titration.

Because the redox potential of DSD-Fdm is comparable to that of natural ferredoxins, we tested the ability of DSD-Fdm to transfer an electron to a natural protein, oxidized cytochrome c (E_m = +200 mV vs NHE). DSD-Fdm was reduced by sequential addition of sodium dithionite, monitoring the loss of absorbance at 410 nm, and stopping addition as soon as the signal stabilized. The reduced peptide was further purified to remove all excess dithionite and titrated into an air-oxidized sample of Thermosynechococcus elongatus cytochrome c_{550}, while monitoring the reaction by UV–vis spectroscopy. We observed shifts of the Soret band (410 to 415

nm) and of the Q-bands (526 to 520 and 550 nm) that indicate reduction of the protein-bound heme (Figure 25). A plot of the change of absorbance at 415 nm as a function of molar equivalents of holo DSD-Fdm reveals that full reduction of the heme was achieved at a 0.74:1 molar ratio of DSD-Fdm/cyt c_{550} (Figure 26). This stoichiometry is reminiscent of the one-electron reduction processes typically mediated by natural bis-[4Fe4S] cluster ferredoxins and is consistent with the EPR spin quantification results, because incomplete reduction of the clusters would result in deviation of the ideal 0.5:1 molar ratio for a two electron-carrying ferredoxin that mediates one electron reductions.[60, 61] Together with the similarity in redox potential, these results show that artificial proteins can interface effectively with natural ones to support redox reactivity.

De novo designed redox proteins have been proposed as functional parts of energy harvesting devices.[62-66] To investigate whether holo DSD-Fdm could be used for this application, we investigated the interaction of a porphyrin photosensitizer with the oxidized cluster using laser flash photolysis. Solutions of zinc 5,10,15,20-tetrakis(4-diethyl 2- benzylmalonate) porphyrin (Zn-P, ca. 15 μM; Figure 6) in deoxygenated buffer were excited at a Q-band (560 nm), and the triplet state lifetimes were probed via the transient absorption at 450 nm. We observed that samples containing either Zn-P only or Zn-P and apo DSD- Fdm had similar triplet lifetimes, ca. 1400 μs, while in the presence of holo DSD-Fdm, the triplet lifetime of Zn-P was significantly shorter, ca. 100 μs (Figure 27). This quenching by a factor of

ca. 14 signals electronic interactions between the zinc porphyrin and the iron–sulfur clusters. No signal for oxidized zinc porphyrin was detected at 650 nm.

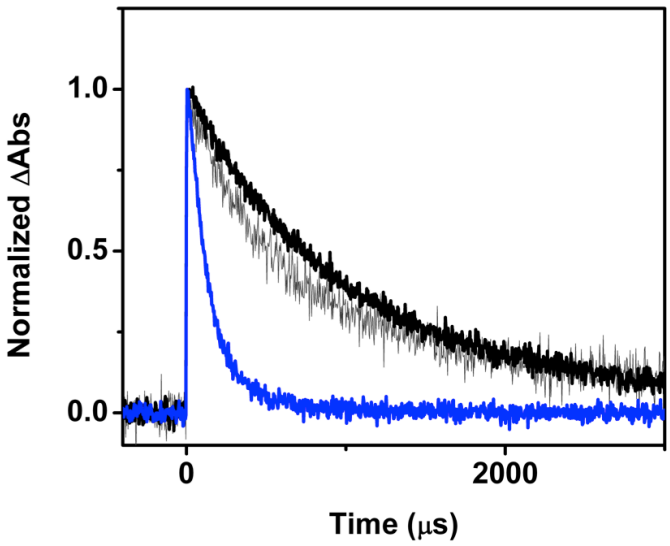

Figure 27: Normalized transient absorption kinetics of Zn-P alone (gray), with apo protein (black), or with holo protein (blue) solutions. The porphyrin was excited at the 560 nm Q-band and probed at 450 nm.

The Zn-P triplet excited state quenching could occur via three mechanisms: triplet–triplet energy transfer, enhanced intersystem crossing (ISC), or photoinduced electron transfer. Photoinduced electron transfer is exergonic by only about 70 meV, based on the reduction potential for the cluster given above (−0.479 V vs SHE), the first oxidation potential of zinc tetraphenylporphyrin (1.04 V vs SHE), and the energy of the zinc tetraphenylporphyrin triplet state (1.59 eV).[67] Although no porphyrin radical cation was detected, photoinduced electron transfer cannot be

completely ruled out because no porphyrin radical cation absorption would be detected if charge recombination were substantially more rapid than charge separation. While the available data do not allow us to assign a mechanism for the quenching, all these possibilities require electronic interaction between the porphyrin and the cluster, which necessitates separations of only a few angstroms. Thus, the results show that external reagents can approach the clusters within the peptide closely enough for interesting and potentially useful energy and electron transfer interactions.

In summary, we designed a protein, DSD-Fdm, in which two [4Fe4S] clusters are within 12 Å of one another, a distance biologically relevant for effective electron transfer. Both apo and holo DSD-Fdm fold into stable dimers with high helical content. Cofactor binding imparts a significant amount of stability toward chemical denaturation, as often seen in designed metalloproteins.[68, 69] The redox potential of DSD- Fdm, −0.479 V vs SHE for the $[4Fe4S]^{2+/1+}$ couple, is within the range typical of low-potential ferredoxins. We showed that DSD-Fdm can interface functionally with natural redox proteins by demonstrating stoichiometric electron transfer from reduced DSD-Fdm to oxidized cytochrome c. Further, we demonstrated that DSD-Fdm can interact electronically with a photoexcited dye. Compared with their natural counterparts, de novo designed proteins can be specifically tailored in terms of their redox potentials, stability, catalytic properties, protein−protein interactions, and small molecule binding depending on the application desired.[70-79] The results presented here support the use of *de novo* designed proteins as redox modules in

various applications, ranging from components of artificial redox pathways in synthetic biology to parts of light-driven devices.

CHAPTER 3

PROTEIN SCAFFOLD ENGINEERING FOR COBALT PORPHYRIN MEDIATED H_2 PRODUCTION

3.1 Introduction

In the quest for alternative, sustainable fuels to address increasing societal needs, molecular hydrogen has arisen as a forerunner because it is potentially carbon independent, energy-rich, and transportable.[80, 81] At the moment, however, hydrogen production relies on steam reforming of hydrocarbons at high temperatures or on the use of precious metal catalysts, such as platinum, and can't be scaled up in a sustainable manner. Nature, in contrast, utilizes a class of enzymes called hydrogenases, which contain an unusual bimetallic active site ([FeFe] or [NiFe]) and reversibly catalyze the reduction of protons to molecular hydrogen.[6, 53, 55, 82] Remarkably, hydrogenases function in weakly acidic conditions, at low overpotentials, with non-noble metals, and catalyze hydrogen production with high turnover frequencies (5000–21000 s^{-1}).[83, 84]

The application of these enzymes to scalable hydrogen production is hampered by their difficulty of overexpression and high oxygen sensitivity.[46, 85] For these reasons, chemists have sought to develop robust organometallic catalysts as alternatives to the natural enzymes.[86-89] In response to this challenge several organometallic catalysts based on earth-abundant transition metals such as Fe, Ni, and Co have been reported.[88, 90-95] With few notable exceptions, however, these systems are unable to work in water at mild conditions, and often require high

overpotentials.[91, 96-98] Further, obtaining catalytic efficiencies on par with natural hydrogenases remain a challenge.

Cobalt macrocyclic complexes are a particularly attractive family of hydrogen production catalysts because they can be easily modified, allowing for fine control over redox properties, coupled with their unique ability to function under aerobic conditions.[86, 99-102] Within this family, cobalt porphyrins remain relatively unexplored despite their promising properties; recent reports have begun to explore both the photochemical and electrochemical reduction of protons by cobalt porphyrins.[103-106] For example, a marked decrease in overpotential for electrochemical hydrogen evolution was designed into a cobalt porphyrin through use of the "hangman" moiety, where inclusion of a carboxylic acid on the periphery of the macrocycle optimally places the acid to function as a proton shuttle during catalysis.[104] In separate work, by introducing positive ionic functionalities onto a Co(II) porphyrin scaffold, photoinduced hydrogen evolution in neutral water was obtained.[106] While both successful in their designs, the ability to only functionalize the periphery of the porphyrin in purely organometallic systems limits their widespread use, as natural catalysts often have 3D contacts to facilitate catalysts.

More recently, we and others have explored the substitution of CoPP(IX) for FePP(IX) in heme-binding peptides and proteins in order to establish these 3D contacts.[107, 108] One of the advantages of these systems is that the protein component is optimized to bind the porphyrin macrocycle and coordinate the metal via robust axial ligation by a single histidine residue, leaving the second axial position open for

either protonation or for introduction of alternative coordinating residues. Substitution of cobalt for iron in microperoxidase-11 (CoMP11), a proteolytic fragment of cytochrome c, resulted in an electrocatalyst for proton reduction in water at pH 7, with an overpotential of 850 mV, turnover frequency of 6.7 s^{-1}, and high Faradaic efficiency (>85% depending on conditions). (Figure 28) In this construct, the CoPP(IX) is covalently linked to a helical fragment via thioether linkage to the porphyrin vinyl groups, and solvent exposed on the other side. These features are likely associated with loss of activity over a relatively short time (15 minutes).

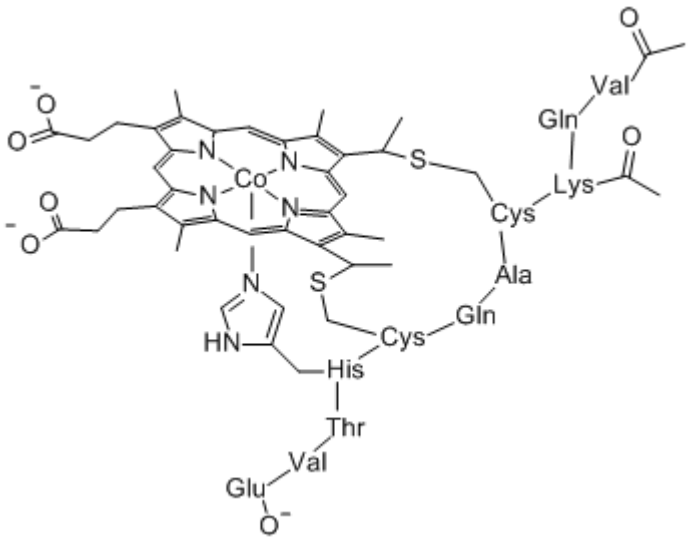

Figure 28: Bisacetylated cobalt microperoxidase-11

Conversely, incorporation of CoPP(IX) (and other cobalt based catalysts) into native, well-structured proteins is a developing approach to modulate the intrinsic

activity of the catalytic center through second-sphere and long-range interactions, while shielding the macrocycle from inactivation through unproductive pathways such as dimerization. Further, proteins provide rapid access to alteration of the coordination sphere and long-range interactions through rational mutagenesis and/or directed evolution. Here I will present two approaches for the design of biohybrid systems which modulate the properties of a bound CoPP(IX) catalyst. The first uses myoglobin, a well-studied oxygen transport protein, to install a gas channel in the proximity of the catalyst. The second approach utilizes cytochrome b_{562}, a soluble electron transport protein, to alter the residues occupying the primary coordination shell of the bound cobalt porphyrin.

3.2 Materials and Methods

Mutant Generation, Purification, and Porphyrin Incorporation

Mutants were generated using Gibson assembly and sequenced directly in the pET30c+ vector utilizing the T7 promoter sequence.[109] Verified mutants were transformed into a BL21(DE3) cell line and grown in 1L of 2xTY media at 37°C with shaking. Cells were induced with 1 mM IPTG at and OD_{600} of 0.6 and cells were harvested after 4 hours of expression. Cell pellets were suspended in 20 mM Tris-HCl, 1 mM DTT, 0.5 mM EDTA and lysed by multiple cycles of ultrasonication. The clarified lysate was brought to either 75% saturation (Cyt b_{562}) or 55% (Myoglobin) with solid ammonium sulfate and precipitated proteins were removed by centrifugation. Myoglobin supernatant was brought to 75% saturation and the precipitated proteins collected for further purification. The Cyt b_{562} supernatant,

containing the cytochrome mutants, was dialyzed against two changes of 10 mM Tris, pH 7.5 at 4°C. Proteins were further purified via RP-HPLC utilizing a preparatory scale C18 column with a linear gradient from 100% A (99.9% water, 0.1% trifluroacetic acid (TFA)) to 100% B (95% acetonitrile, 4.9 % water, 0.1% TFA), followed by lyophilization to yield the pure apo-protein. Protein identities were confirmed via MALDI-TOF-TOF spectrometry and purity by C18 analytical analysis.

Purified proteins were reconstituted with Co-Protoporphyrin IX (CoPP(IX)) similarly to previously reported procedures.[110, 111] Samples in 100 mM Tris, pH 8.5 were subjected to 50 molar excess of DTT for 30 min, followed by a 50 molar excess of CoPP(IX) for 1 h. Excess porphyrin was removed by subjecting protein to a PD10 desalting column (GE Healthcare) equilibrated in 50 mM Tris pH 7.5. Sample concentrations were determined via UV-Vis spectroscopy utilizing extinction coefficients of 17.0 mM^{-1} cm^{-1} for all myoglobin mutants, 8.6 mM^{-1} cm^{-1} (WTCytb_{562}), 16.0 mM^{-1} cm^{-1} (M7A), 12.0 mM^{-1} cm^{-1} (M7E), and 9.9 mM^{-1} cm^{-1} (M7D) at the Soret. Protein was used immediately or frozen at -80 °C for future characterization.

Porphyrin Affinity Determination

Apo and CoPP(IX)-bound proteins were characterized by UV-vis spectroscopy. All spectra were recorded on a Varian 50 Cary Bio Spectrophotometer. Binding affinities to CoPP(IX) were determined by UV-vis monitored titrations. Samples of the apo-protein in phosphate buffered saline were titrated by sequential addition of a Co(III)PP(IX) chloride stock in 0.1 M KOH and

incubated for 10 minutes to allow for equilibration before data acquisition. The shift in the Soret peak of the bound state (425-430 nm) towards the unbound state (418 nm) was monitored as a function of porphyrin concentration, and data were analyzed with a simple 1:1 binding model.

Circular Dichroism Spectroscopy

CD spectra were recorded on a JASCO J-815 spectropolarimeter in the range of 190-260 nm. Data were recorded every 1 nm and averaged over 3 scans. The concentration of apo and holo-peptides were kept at 10 μM in 10 mM Tris, pH 7.5; measurements of the apo-peptide were carried out in the presence of an excess of TCEP. Thermal denaturation was performed by heating samples from 4-90°C, monitoring loss of signal at 222 nm.

Electrochemical Methods

Electrochemical experiments were carried out using a CH-instruments 1242B potentiostat. For all electrochemical measurements, a three-electrode system was used: a 3-mm diameter glassy carbon working electrode with a surface area of 0.28 cm^2, platinum mesh counter electrode, and a saturated calomel reference electrode. Electrolyte solutions were degassed by incubation in a Coy anaerobic chamber for 2 days prior to use. Working electrodes were polished with 1 μm alumina for 5 minutes followed by 10 minutes of sonication. Electrodes were cleaned electrochemically by cycling 40 times between 1.2 and -1.2 V at 100 mV sec, followed by extensive washing with water, prior to use. Data were background subtracted using the SOAS software.[112]

Photoinduced H_2 Production

Irradiation was performed using a Lumileds LXS8-PW27-0024(N) lamp, irradiating at a constant 1100 W/m^2 throughout the experiment. For each experiment, 1 mM $Ru(Bpy)_3^{2+}$, 100 mM sodium ascorbate, and the desired catalyst were added to a 1 M potassium phosphate buffer at the appropriate pH. A 400 μL total reaction volume was added to a custom made airtight 1 mm cuvette and degassed extensively with argon prior to illumination. During irradiation time course experiments, 100 μL samples of gas taken from the headspace with a gas-tight syringe were injected directly for analysis with a SRI 310C gas chromatograph fitted with a 5 Å molecular sieve column and thermal conductivity detection. Calibration was achieved by injection of various volumes of a 1% H_2, 99% N_2 gas mixture onto the GC.

An in-house developed continuous flow system was used for hydrogen detection in aerobic conditions similar to previous reports.[113, 114] An argon carrier stream flowing at 3 mL min^{-1} delivered hydrogen produced in the reaction chamber to an in-line Figaro tin oxide hydrogen sensor (model TGS821, Figaro Engineering). The output of the hydrogen sensor was amplified using an instrumentation op-amp (Analog Devices, AD620AN). Illumination was achieved using a xenon arc lamp (Oriel 68811 power supply with 66028 lamp) at a total intensity of 1100 W/m^2. For each experiment, 1 mM $Ru(Bpy)_3^{2+}$, 100 mM sodium ascorbate, and the desired catalyst were added to a 1 M potassium phosphate buffer and placed in a gas tight cuvette. Samples were equilibrated in the flowing gas for 30 minutes, followed by 30

minutes of baseline collection in the dark. Rates of hydrogen production were integrated to obtain moles of hydrogen produced, and utilized for calculation of final TON.

3.3 Myoglobin as a probe for secondary shell interactions

Here, we present an alternative approach by which a cobalt-derivatized porphyrin is buried into a protein scaffold, myoglobin. This well-folded, stable protein scaffold binds heme (Fe-Protoporphyrin IX) leaving the metal in a pentacoordinate state; the sixth position is available for coordination to molecular oxygen and other substrates. Myoglobin withstands mutagenesis at positions close to the vacant axial site, facilitating the engineering of catalytic sites into the scaffold.[106, 115] In addition, myoglobin readily accommodates unnatural cofactors.[111, 116-118] In the case of Co-Protoporphyrin IX, incorporation into myoglobin provides additional second sphere and long-range interactions, while protecting the cofactor from degradation. Our results show that CoMyo (Figure 29) catalyzes photoinduced production of hydrogen with high efficiency, and that activity is modulated by engineered mutations.

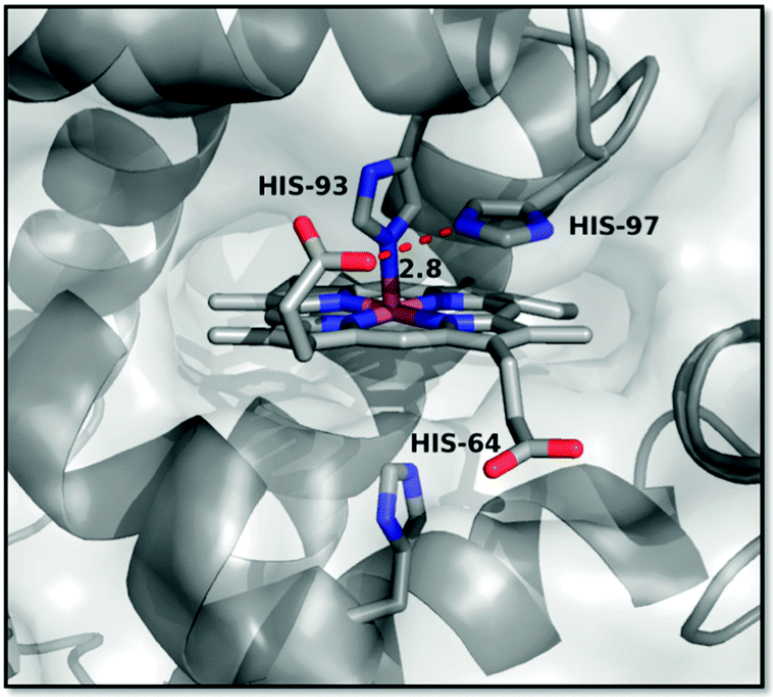

Figure 29: Crystal structure (PDB 1YOI) of Co-myoglobin active site, highlighting residues H93, H97 and H64.

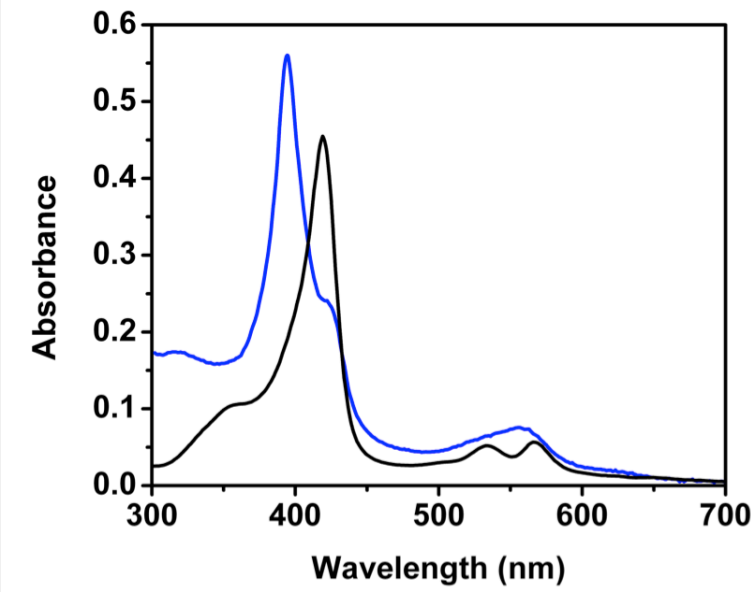

Figure 30: UV-Vis traces of 2.6 μM CoMyo in 100 mM KPi pH 7.5 in the oxidized (black) and dithionite reduced (blue) states.

Preparation of CoMyo was accomplished with cobaltous protoporphyrin IX (CoPP(IX)) using established methods.[116] The electronic spectra of the air-oxidized protein displays absorbance maxima at 425, 534, and 567 nm, typical of Co(III) porphyrins (Figure 30). These maxima are red shifted relative to other peptide-based catalytic systems, which exhibit maxima at 415, 530, and 560 nm, indicating shielding CoPP(IX) from the aqueous environment.[107, 119] Reduction of the holo protein at pH 7.5 with a 500 molar excess of sodium dithionite resulted in shift of the Soret and *q*-bands to 394 and 557 nm, respectively, corresponding to a Co(II) species (Figure 30).

We then assayed the ability of CoMyo and CoPP(IX) to catalyze the reduction of protons to hydrogen by cyclic voltammetry (CV) (Figure 31). CoPP(IX), which has low solubility in water, was studied in acetonitrile (MeCN) with 0.1 M (n-Bu_4N)(PF_6) as the supporting electrolyte. (Figure 32) A quasi-reversible wave appears at -1.17 V vs SHE after referencing to ferrocene monocarboxylic acid, assigned to the reduction of Co(II) to Co(I). Addition of para-toluenesulfonic acid to the anhydrous acetonitrile results in the onset of a catalytic wave at -1 V, thus implicating this redox couple as the catalytically active species (Figure 33).[104] In the case of CoMyo, the onset of a strong catalytic wave is observed at -0.95 V against SHE in the CV scans in 200 mM Tris-HCl buffered solution, concealing the Co(II)/Co(I) peak (Figure 30). This wave is 200 mV positive of the catalytic wave of a bare glassy carbon electrode (Figure 34), and not seen in the presence of apomyoglobin alone (Figure 30). These values are in agreement with previous work on aqueous cobalt

macrocycles.[104, 106, 120] However, the catalytic onset potential is approximately 100 mV closer to the thermodynamic value compared to other water-soluble cobalt porphyrins assayed.[106]

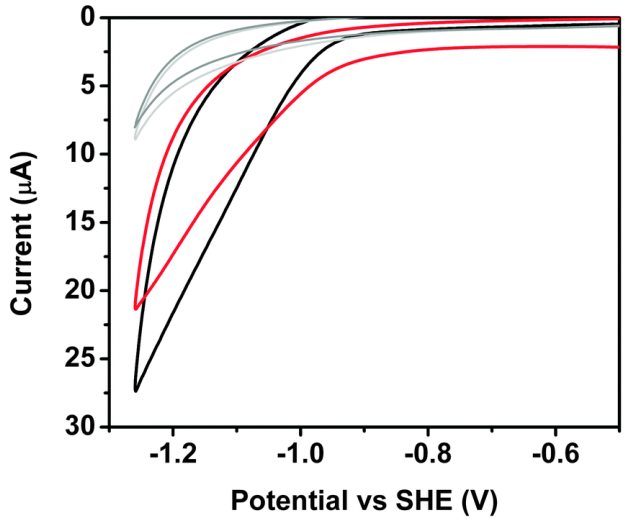

Figure 31: Cyclic voltammograms of a blank electrode (light grey), 1.5 μM apomyoglobin (dark grey), and 1.5 μM CoMyo in the absence (black) and presence (red) of oxygen in a 200 mM Tris-HCl, 100 mM NaCl, pH 7.5 solution at 100 mV s^{-1} with a 0.28 cm^2 glassy carbon working electrode.

The peak catalytic current for scans down to -1.26 V is linearly dependent on CoMyo concentration (Figure 35). The catalytic current was found to be strongly dependent on the pH of the solution, as expected for a molecular hydrogen generating system (Figure 36). CV scans were also performed in unsealed electrochemical cells open to the ambient atmosphere; negligible catalytic current

loss was observed after introduction of oxygen into the electrochemical setup (Figure 31). However, loss of activity of the CoMyo system is seen below pH 6, due to protonation of the ligating His93 in the myoglobin core and loss of the porphyrin from the hydrophobic core of myoglobin.

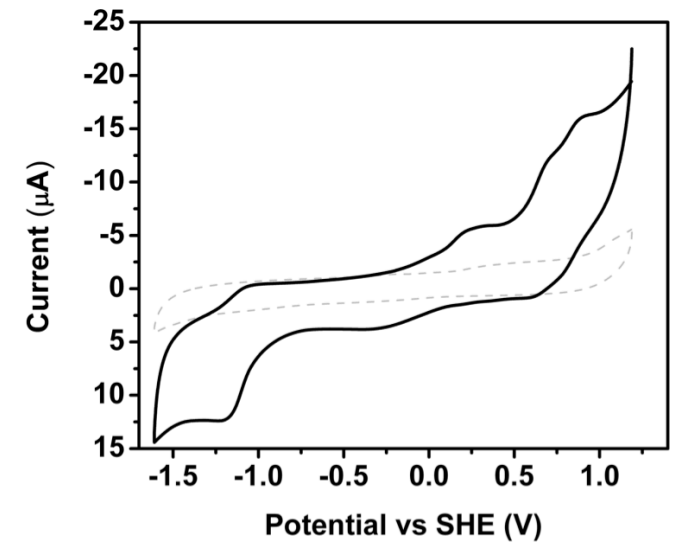

Figure 32: Cyclic Voltammagram of a 1 mM CoPP(IX) solution in MeCN with 0.1 M (*n*-Bu_4N)PF_6 (solid line), compared to a blank scan (dotted line), at 100 mV/s with a glassy carbon working electrode.

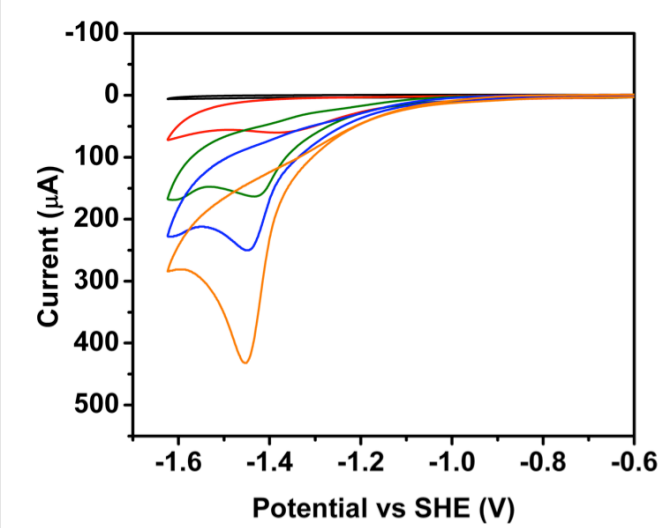

Figure 33: Cyclic voltammograms of 250 μM CoPP(IX) in MeCN with 0.1 M (*n*-$Bu_4N)PF_6$ with increasing concentrations of tosic acid. (Black: 0 mM, Red: 1.2 mM, Green: 3.6 mM, Blue: 4.8 mM, Orange: 7 mM) Scan rate was 100 mV/s with a glassy carbon electrode.

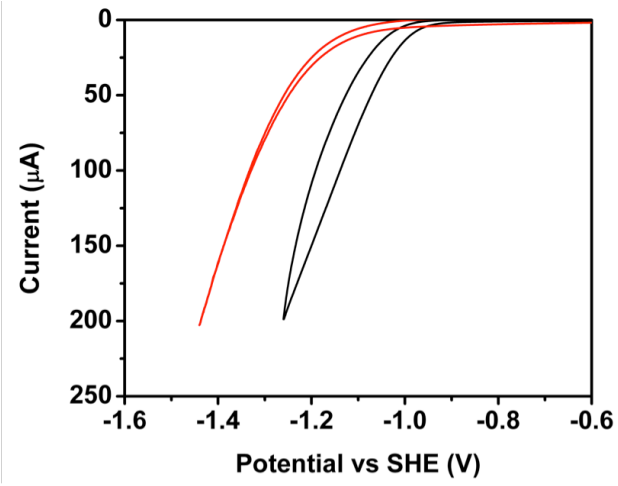

Figure 34: Cyclic Voltammograms of a blank glassy carbon electrode (red) compared to 1.5 μM H64A mutant (black) at pH 7.0 in 100 mM KPi, 200 mM KCl at a scan rate of 100 mV/s.

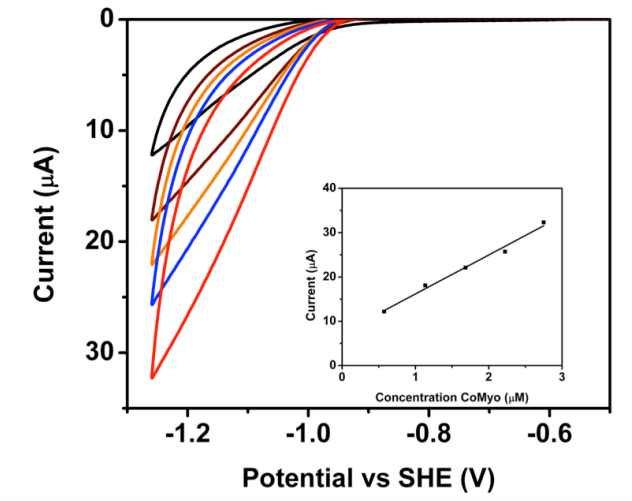

Figure 35: Cyclic voltammograms of WT CoMyo at varied concentrations in 100 mM Tris-HCl, 200 mM NaCl, pH 7.5 at 100 mV/s with a glassy carbon electrode. Inset: Linear fit of current at -1.26 V vs SHE for various concentrations of CoMyo.

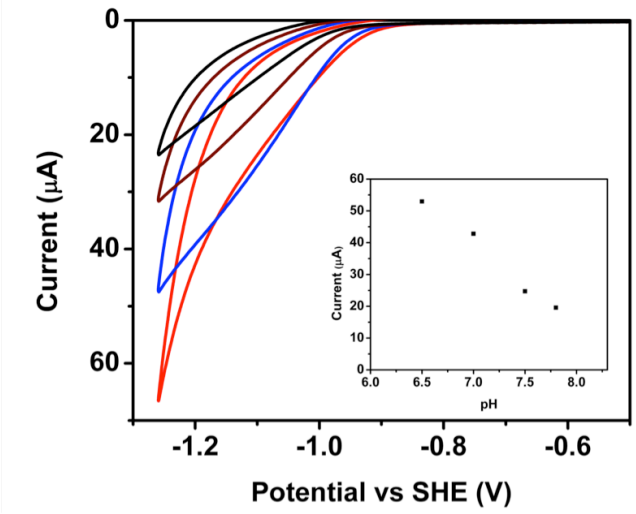

Figure 36: Cyclic voltammograms of 1.6 μM WT CoMyo at varied pH levels of 100 mM Tris-HCl, 200 mM NaCl at 100 mV/s with a glassy carbon electrode. Inset: Current at -1.26 V vs SHE for varied pH levels.

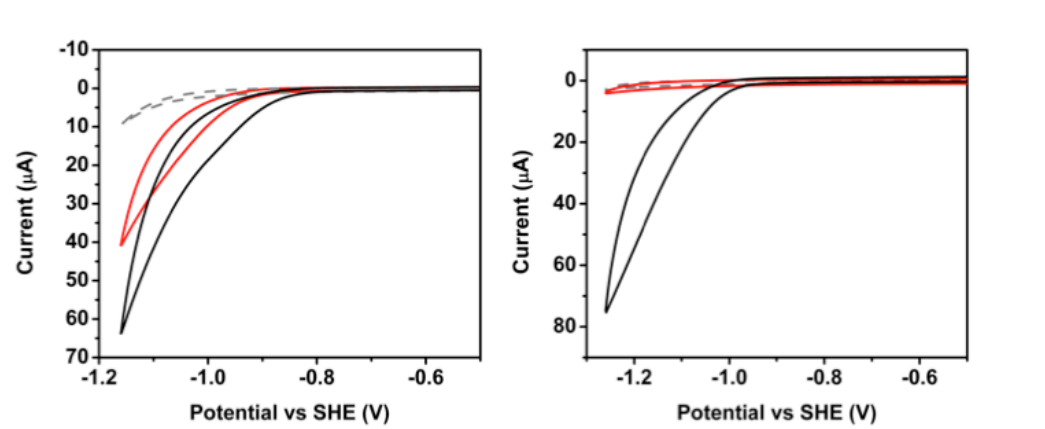

Figure 37: Left) Cyclic voltammogram in pH 4.5, 100 mM Citrate, 100 mM NaCl of the blank scan (grey dashed), after addition of 2.6 µM WT CoMyo (black), and after placing rinsed electrode back into fresh buffer (red). Right) Cyclic voltammogram in pH 7.5, 100 mM Tris-HCl, 100 mM NaCl of the blank scan (grey dashed), after addition of 5.5 µM WT CoMyo (black), and after placing rinsed electrode back into fresh buffer (red).

To confirm the loss of CoPP(IX) from the active site, rinse tests were performed (Figure 37). Consecutive scans on a 1.5 µM sample of CoMyo at a pH of 7.5 showed negligible loss of catalytic current. Removing the electrode from the CoMyo solution, rinsing, and placing into fresh buffer without CoMyo yielded no catalytic current, indicating no degradation of the catalytic system at the electrode surface to form an electroactive film. Upon lowering of the pH to 4.5, consecutive scans on CoMyo in solution yielded a catalytic wave, as expected. When the electrode was rinsed and placed into buffer containing no CoMyo, the catalytic wave

observed persisted, indicating deposition of CoPP(IX) onto the electrode surface. UV-Vis spectra of CoMyo at pH 4 revealed a red shift of the Soret band to 427 nm, consistent with the loss of coordination by the axial His93 (Figure 38).[121] Because of this loss of coordination, we chose to characterize the CoMyo system at pH levels above 6.5, avoiding characterization of a mixture of myoglobin-bound and unbound CoPP(IX).

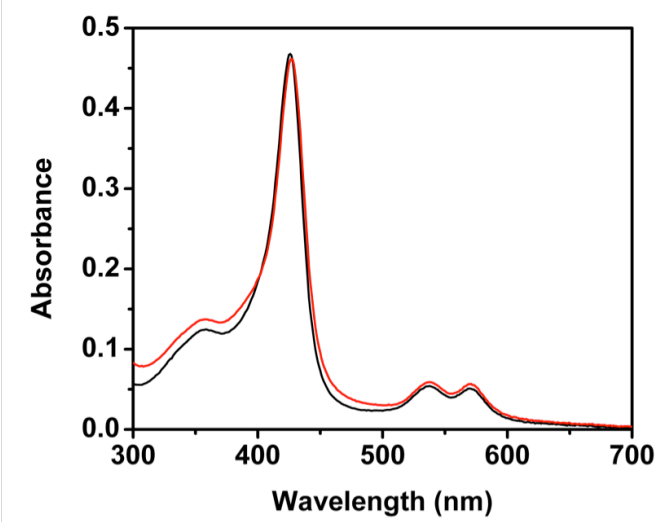

Figure 38: UV-Vis spectra of 2.6 µM WT CoMyo in 100 mM Tris, 100 mM NaCl, pH 7.5 (black trace) and 2.6 µM WT CoMyo in 100 mM Citrate, 100 mM NaCl, pH 4.5.

We investigated whether incorporation of catalysts into hydrophobic, peptide-rich environments could modulate the intrinsic activity of CoPP(IX) by assessing hydrogen production in the presence of a photosensitizer and sacrificial electron donor. In a typical experiment, samples were irradiated with 1100 W/m^2 of visible light (>400) in the presence of 1 mM $Ru(Bpy)_3^{2+}$ and 100 mM sodium

ascorbate, a sacrificial electron donor, over the course of 12 hours. Hydrogen evolution was quantified by analyzing aliquots of headspace volume of the anaerobic cuvette via gas chromatography as a function of time.

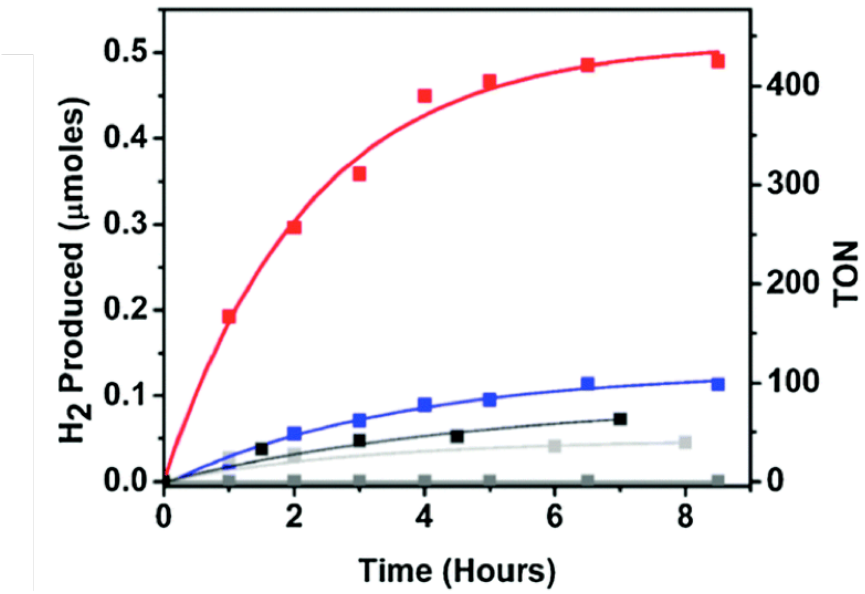

Figure 39: Photoinduced (410–770 nm) hydrogen production in 1 M KPi with 0.1 M sodium ascorbate and 1 mM $Ru(bpy)_3^{2+}$ at pH 7. Traces correspond to WT CoMyo (red), CoPP(IX) (blue), Ferric WTMyo (dark grey), no catalyst (light grey), and WT CoMyo lacking $Ru(bpy)_3^{2+}$ (grey).

Table 1: pH dependence of photoinduced hydrogen production of WT CoMyo

pH	TON	TOF (min^{-1})	Enhancement Factor[a]
6.5	234	0.47	2.13
7	518	1.47	4.32
7.5	454	0.85	2.84

[a]Enhancement over CoPP(IX) assayed under the same conditions.

We found that the CoMyo system efficiently produces hydrogen under these conditions, achieving turnover numbers (TON) ranging from 230-520. Direct comparison of photoinduced catalysis of the CoMyo system to free-CoPP(IX) showed that incorporation of the porphyrin into the protein scaffold increased the TON by a factor of 3 on average (Table 1). In the same conditions, ferric myoglobin produces only a nominal amount of H_2, comparable to controls lacking any catalyst at all (Figure 39).

The activity of porphyrin based catalysts, expressed as TON, have strong inverse relationship with concentration, because activity is lost when dimers form. In contrast, CoMyo proved to be resilient to changes in catalyst concentration, yielding the same TON for all concentrations tested (1 μM – 5 μM). The activity of CoMyo is pH dependent, with maximal photoinduced hydrogen production observed at pH 7, and was lower as pH either increased or decreased (Table 1). The loss of activity observed at higher pH is easily justified, as lower concentrations of protons will result in lower TON. However, protonation of the axial histidine and of the two distal histidines in the active site (His64 and His97) with pKa value of ~5 and 5.6, respectively, also results in loss of activity.[122, 123]

To verify this hypothesis, we generated three mutants of myoglobin, in which histidines were exchanged for non-ionizable alanine: H64A, H97A, and H64/97A (Figure 29). We found that the H64A and H97/64A point mutants increased catalytic activity of CoMyo at pH 6.5 to 331 and 512 TON, respectively, compared to the 231 TON observed for WT (Figure 40). However, the H97A mutant reduced the

TON to 120, only slightly higher than the porphyrin alone (TON 100). Electrochemical analysis of the mutants at pH 7 revealed an increase of current at -1.26 V vs. SHE for both the H64A and double mutant and a reduction of catalytic current of H97A, but no change of the onset of catalytic hydrogen reduction (Figure 41). Two factors could play a role in the change in the catalytic peak height upon removal of the two active site His. First, removing His64 from the proximity of the CoPP(IX) catalysts removes a slight positive charge at physiological pH levels, as well as the potential for His64 to compete for proton binding. The loss of this positive charge will shift the redox potential of the catalyst more positive, allowing for easier reduction of protons at the catalytic site. Characterization of the electrochemical pH dependence of the H64A mutant shows a stronger dependence of catalytic activity on pH, a direct result of these two changes. (Figure 42).

Secondly, closer inspection of the active site of CoMyo reveals a hydrogen bond forming between the His97 residue and one of the propionic acid groups of CoPP(IX). Removing this residue destabilizes the binding of the porphyrin, altering steric constraints on the porphyrin and increasing the degrees of freedom between the scaffold and the catalyst, lowering its catalytic ability by diminishing enhancing contacts with the scaffold. It has been shown that with heme in the myoglobin active site, a H97D mutation increases lability of the cofactor by a factor of 38.[124] In CoMyo, increased cofactor lability results in loss of scaffold-mediated enhancement of catalytic activity, as the H97A mutant is nearly indistinguishable from the free porphyrin. During photoinduced hydrogen production, removal of this residue also

increases the solvent-accessibility of the active site, and may allow for increased interaction between the photosensitizer and the catalyst, increasing the TON of the H97/64A mutant relative to the H64A mutant.

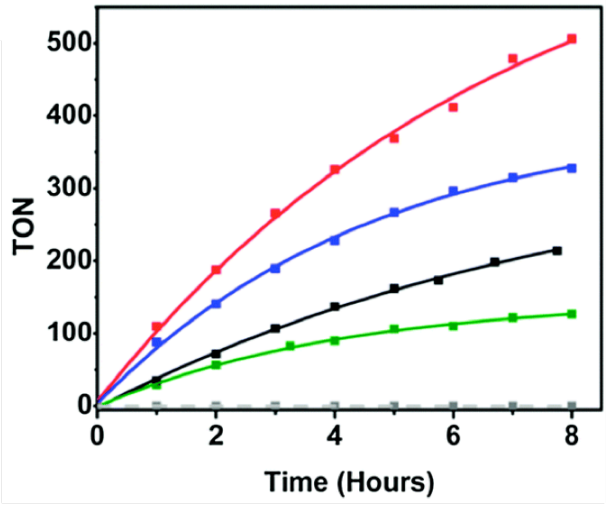

Figure 40: Photoinduced hydrogen production of CoMyo variants, 1 M KPi with 0.1 M sodium ascorbate and 1 mM $Ru(bpy)_3^{2+}$ at pH 7. Traces correspond to WT (black), H97A (green), H64A (blue), H64/97A (red).

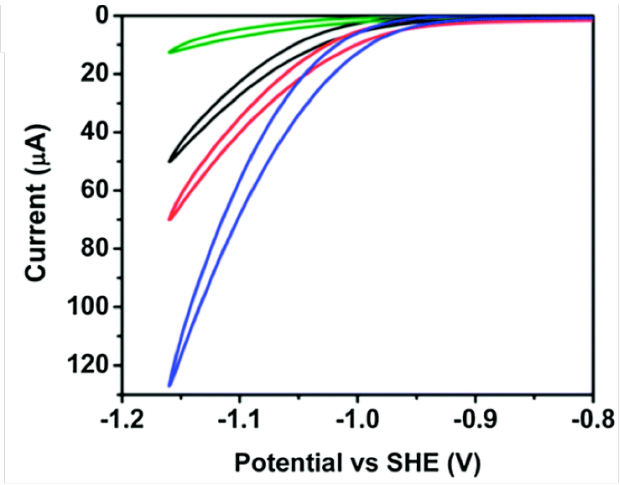

Figure 41: Cyclic voltammograms of 1.5 μM myoglobin mutants in 200 mM Tris-HCl, 100 mM NaCl, at pH 7 at a scan rate of 100 mV s^{-1} with a 0.28 cm^2 glassy carbon working electrode (WT (black), H97A (green), H64A (blue), H64/97A (red)).

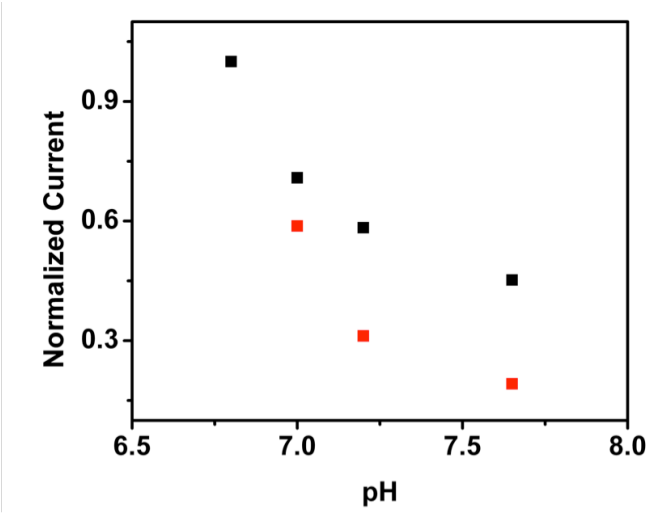

Figure 42: Catalytic current at -1.26 V for WT (black) and H64A (red) CoMyo at various pH levels in 100 mM KPi, 200 mM KCl with a glassy carbon working electrode at 100 mV/s. Data were normalized to current at pH of 6.8 to account for variation in catalytic activity of the two systems.

The variation of photoinduced catalysis of hydrogen production by these mutants confirms that the protein environment plays a major role in the overall increase of catalysis of the CoPP(IX), affecting not only the stability of the catalyst but also the competing processes and redox activity in the active site. These effects are reminiscent of the role of the protein matrix in [FeFe] hydrogenases, in which it augments and modulates the intrinsic activity of the diiron center through secondary shell and long range interactions.[6, 8] This concept was exploited by burying biomimetic inorganic complexes and higher turnover in photocatalytic experiments. Compared to CoMP11, which is essentially a helical peptide covalently linked to a porphyrin, the myoglobin scaffold presents several advantages. First, the scaffold efficiently protects the porphyrin cofactor from degradation, resulting in sustained photoinduced catalytic activity over 480 minutes. In contrast, the electrocatalytic activity of CoMP11 ceased after 15 minutes. Second, the increased complexity of the protein scaffold surrounding the porphyrin allowed us to introduce specific mutations in the second coordination sphere, thus modulating the activity of the protein. Further optimization of the system via directed mutagenesis may be possible. Third, the scaffold is robust and can be functionalized on the surface for attachment to a number of photosensitizers or solid-support materials, allowing for development of a heterogeneous catalytic system. Finally, the non-covalent nature of the interaction between the porphyrin and myoglobin allows for the identity of the catalyst studied to be altered from the native protoporphyrin IX.

In conclusion, we show here that incorporation of macrocycle catalysts through non-covalent interactions into a protein environment allows studying the effect of secondary shell interactions on catalysis. This strategy also allows to facilitate catalysis in aqueous environments using catalysts that would otherwise be limited to organic solvents. The CoMyo system shows significant enhancement of photoinduced hydrogen production for a simple macrocyclic complex, CoPP(IX), due to stabilization of the catalyst by incorporation into a hydrophobic, protein scaffold. Along with the ability to stabilize the catalyst, point mutants of myoglobin affected the catalysis of the CoPP(IX), suggesting that *in vitro* selection techniques could be used to enhance the catalytic activity of CoMyo. Future studies will aim to optimize both the catalyst, as well as the protein environment solubilizing the catalyst, to achieve efficient photoinduced hydrogen production.

3.4 Utilizing Cyt b_{562} to investigate primary coordination

Next, we aimed to explore the effect of dual axial coordination to CoPP(IX) on catalytic activity, using the well characterized electron transfer protein cytochrome b_{562} (cyt b_{562}) as scaffold.[125-128] This protein folds into an antiparallel four-helix bundle and binds a single heme within the hydrophobic core at one of the termini. In contrast to microperoxidase-11 and to myoglobin, cyt b_{562} coordinates heme at each of the two axial positions via methionine 7 and histidine 102, a motif found in a number of electron-transfer proteins.[126, 129-131] We explored the effect of the coordination by comparing variants containing alanine, aspartic acid, or glutamic

acid at the methionine's position. These latter variants were designed to place a proton relay in proximity of the cobalt center, mimicking the "hangman" moiety engineered by Nocera and coworkers.[104] This proton relay plays an important role in a variety of hydrogenase mimics, such as cobalt diimine-dioxime complexes and the nickel-based Dubois catalyst.[96, 100] Rapid proton transfer to the active site is also required in [FeFe] hydrogenases, in which this function is enacted by the secondary amine moiety of the azadithiolate bridging ligand in the H-cluster.[132, 133] We found that exchanging the second axial ligand to cobalt protoporphyrin IX in cyt b_{562} can modulate activity by a factor of 2.5.

We choose as scaffold for our investigation cyt $b_{562,}$ a 106-amino acid protein that folds into a stable, antiparallel four-helix bundle, and binds metallated protoporphyrin (IX) non-covalently through coordination by His107 and Met7.[128] (Figure 43) We characterized CoPP(IX) complex of wild type, and compared it to mutants that explore loss of coordination (M7A) or a switch to carboxylate as coordinating moiety (M7D and M7E) in order to investigate the effect of axial coordination on the properties of Co-Cyt b_{562}. These latter mutations also position a proton relay in proximity of the cobalt, mimicking the "hangman effect" observed for synthetic cobalt porphyrins.[104] Cyt b_{562} mutants were readily purified in the apo form in high yields from the 2xTY media, a media known to increase overexpression yields of heme-containing proteins.

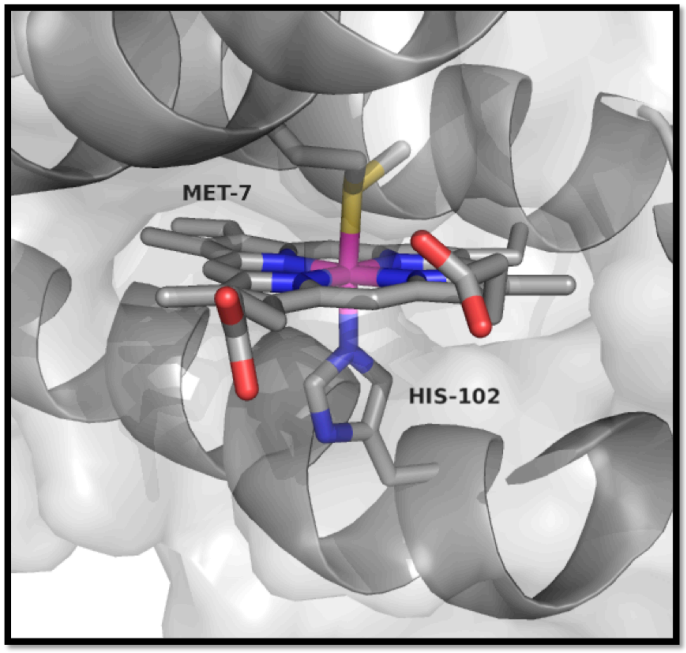

Figure 43: Active site of Fe cytochrome b_{562} (PDB 1QPU) highlighting the coordinating residues Met-7 and His-107.

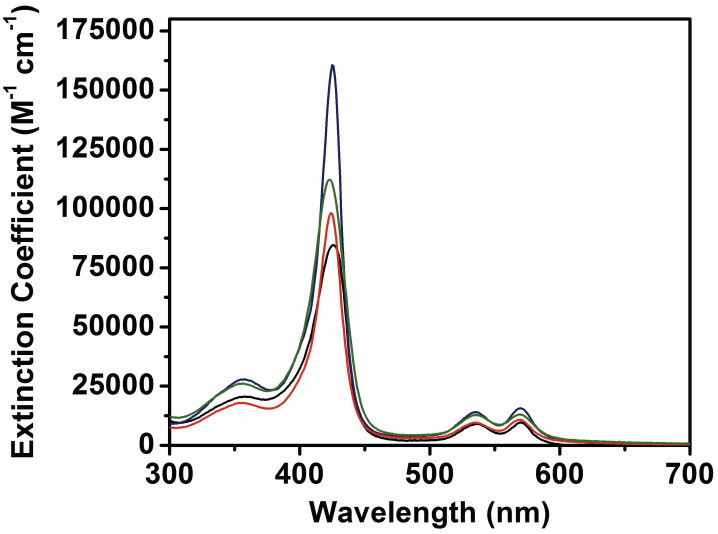

Figure 44: Electronic spectra of Cyt b_{562} variants in 10 mM Tris pH 7.5, traces correspond to CoWT (black), M7A (blue), M7D (red), and M7E (green).

The mutants were reconstituted with CoPP(IX) and analyzed by UV-vis spectroscopy. All variants exhibited absorbance maxima ranging from 425-430 nm for the Soret peak, consistent with protein-bound CoPP(IX). (Figure 44) All the spectra were red shifted relative to free CoPP(IX), indicating shielding of the cofactor from solvent. Notably the extinction coefficients, calculated using metal concentration obtained by ICP-OES, varied widely among the mutants. WT has an extinction coefficient at the Soret of 86 mM^{-1} cm^{-1}, significantly lower than the extinction coefficient of 170 mM^{-1} cm^{-1} we measured for the Soret band of free CoPP(IX) in the same conditions. The large change in coefficient was attributed to the bis-axial coordination observed in the WT protein.[134] Mutant M7A, in which the coordinating Met7 has been removed, has an extinction coefficient for the Soret band of 160 mM^{-1} cm^{-1}, indicative of water in the axial site, poising the designed protein for H_2 production. Mutants M7D and M7E, in which M7 is replaced by carboxylic acid, display intermediate extinction coefficients of 99 mM^{-1} cm^{-1} and 112 mM^{-1} cm^{-1} respectively. Thus, the coefficients reflect the type of coordination. Analysis of the models reveals that one of the rotamers of aspartic acid at position 7 places the carbonyl moiety at a distance of 2.3 Å from the cobalt, allowing axial coordination. Conversely, the extra methylene group in the side chain of glutamic acid results in increased flexibility of the side chain, and places the carboxylate at a distance incompatible with coordination of the metal.

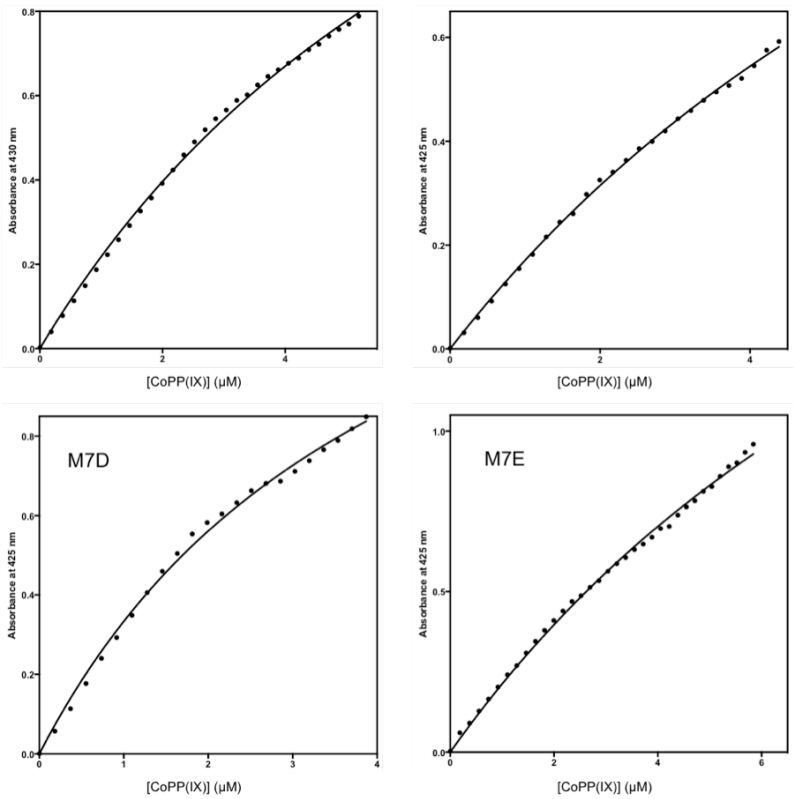

Figure 45: Change in absorbance during titration of CoPP(IX) into apo-Cyt b_{562} variants, monitored at the porphyrin soret band. Data were fit to a simple 1:1 binding model using Prism 6 graphing software.

We evaluated the coordination profiles of the variants by determining the dissociation constants (K_d) for CoPP(IX) via UV-vis monitored titrations (Figure 45). We measured a K_d of 8.9 μM for wild type; remarkably, removal of the coordinating methionine in M7A has little effect, as shown by a dissociation constant of 10.8 μM. Introducing an aspartic acid resulted in improved binding affinity, with K_d of 3.5 μM, indicative of stronger coordination to the Co(III). Conversely, the M7E variant had weaker affinity for the porphyrin as shown by a K_d of 13.5 μM.

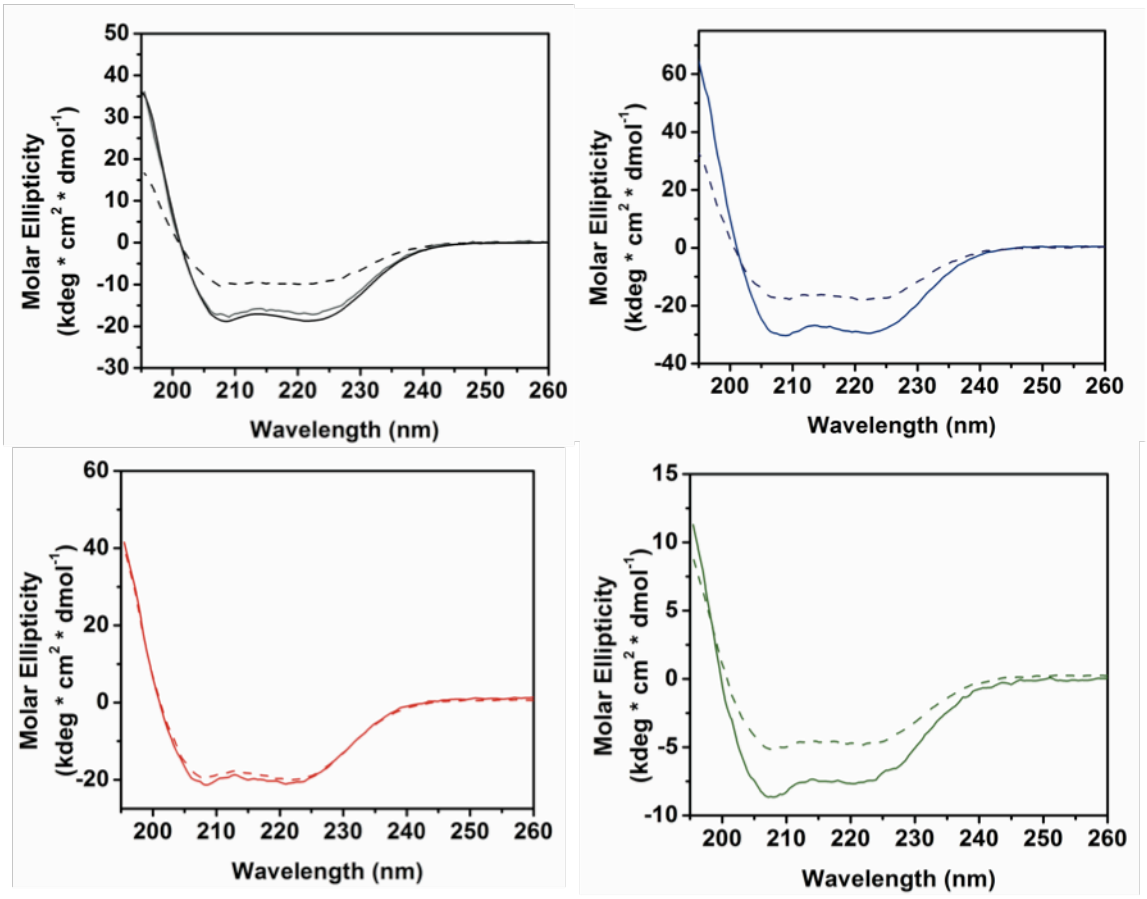

Figure 46: CD spectra of apo (dotted lines) and holo (solid lines) Cyt b_{562} variants in the far-UV range showing two minima at 222nm and 208nm. Proteins were at 10 μM in 10 mM Tris-HCl, pH 7.5. Traces correspond to CoWT (black), M7A (blue), M7D (red), M7E (green), and FeWT (gray, top left panel).

We verified the secondary structure content of the variants by circular dichroism (CD) spectroscopy. All variants exhibited spectra typical of a-helical proteins, with minima at 208 and 222 nm. Incorporation of the porphyrin into the apo-proteins resulted in an increase in the α-helical content (Figure 46). We then

assessed the effect of mutations on the fold stability by determining the thermal denaturation profiles of the variants, monitored by loss of the CD signal at 222 nm (Figure 47). The apo-proteins showed little variations in stability, with an average T_m of 55.2 °C. In contrast, the holo variants exhibited very different denaturation profiles. WT Co-Cyt b_{562} is remarkably stable to thermal denaturation: it is only approximately 80% unfolded at 94 °C, and shows an estimated T_m of 85 °C. Substitution of the coordinating methionine in the M7A and M7D variants lowers the T_m to 65 °C. The M7E variant exhibits a T_m of 61.4 °C, confirming the destabilizing effect of this mutation.

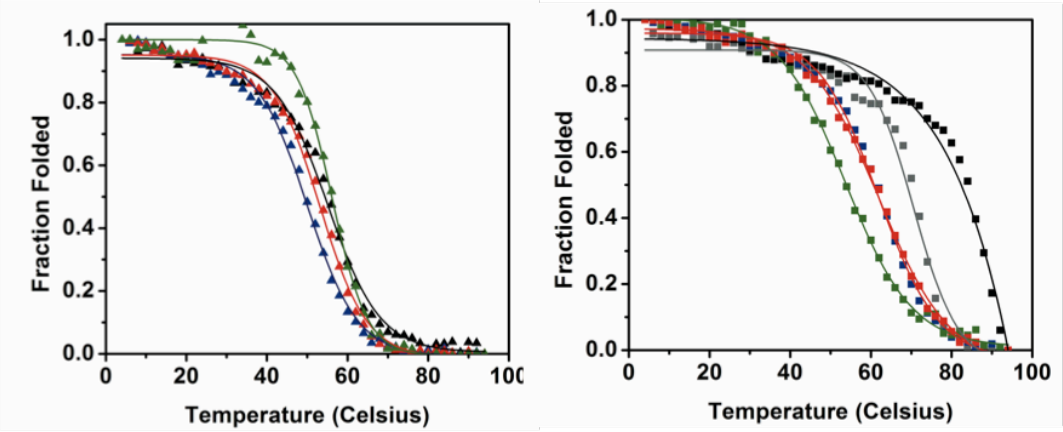

Figure 47: Thermal denaturation curves of Cyt b_{562} variants in the apo (left) and holo (right) forms, monitoring the loss of signal at 222 nm. Proteins were at 10 μM in 10 mM Tris-HCl, pH 7.5. Traces correspond to CoWT (black), M7A (blue), M7D (red), M7E (green), and FeWT (gray).

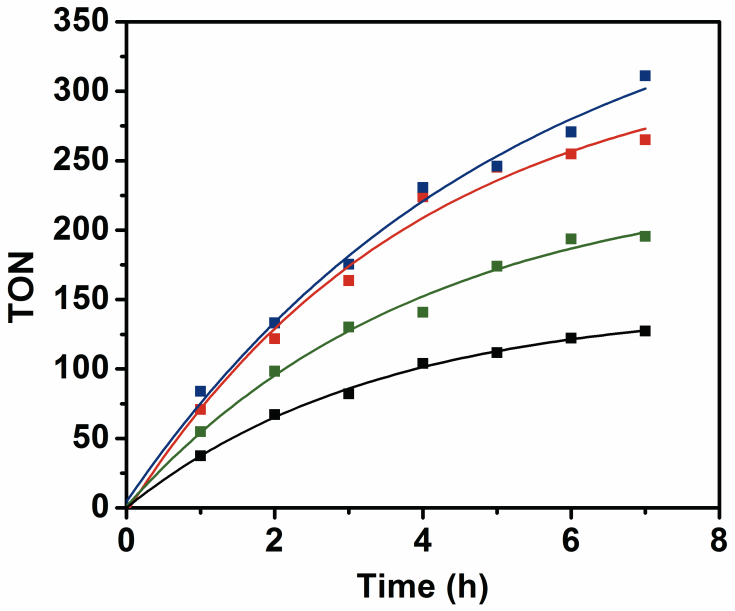

Figure 48: Photoinduced (410–770 nm) hydrogen production in a sealed cuvette with 1 M KPi with 0.1 M sodium ascorbate and 1 mM $Ru(bpy)_3^{2+}$ at pH 7, traces correspond to CoWT (black), M7A (blue), M7D (red), and M7E (green).

We evaluated the ability of the Cyt b_{562} variants to reduce protons in the presence of a photosensitizer and a sacrificial electron donor (Figure 48). In these conditions, proton reduction by cobalt porphyrins results from reduction of a Co(II) species to Co(I), likely via concerted proton-coupled electron transfer (PCET), to release molecular hydrogen; the rate limiting step is thought to be the formation of a Co(III)-H species.[120] Under constant illumination at 1100 W/m^2 of white light, all four proteins exhibited proton reduction activity. The WT Co-Cyt b_{562} showed a final TON of 120 after 8 hours of constant illumination in a sealed cuvette, comparable to the activity of the unbound CoPP(IX) in similar conditions.[108] Reinjection of fresh

$Ru(bpy)_3^{2+}$ into the catalytic system restored catalytic activity, identifying it as the primary limiting factor for the photoinduced reaction (Figure 49). The M7A variant exhibited the highest activity, with a three-fold increase over WT to a final TON of 310. We attribute this increase in activity to the opening of the axial site, which could allow for easier accessibility of protons during the catalytic cycle and facilitates formation of the rate-liming cobalt hydride. Introduction of a carboxylic acid into the axial site also allowed for an increase in the catalytic ability of the cytochrome. The M7E variant exhibited a TON of 195, and M7D resulted in further increase of TON to a final value of 270. We hypothesize that inefficient ligation of the porphyrin and increased structural flexibility may account for the observed activity of M7E, approximately 1.5 fold that of WT. The bis-ligated M7D variant, though, exhibited activity comparable to the M7A mutant containing an open axial site.

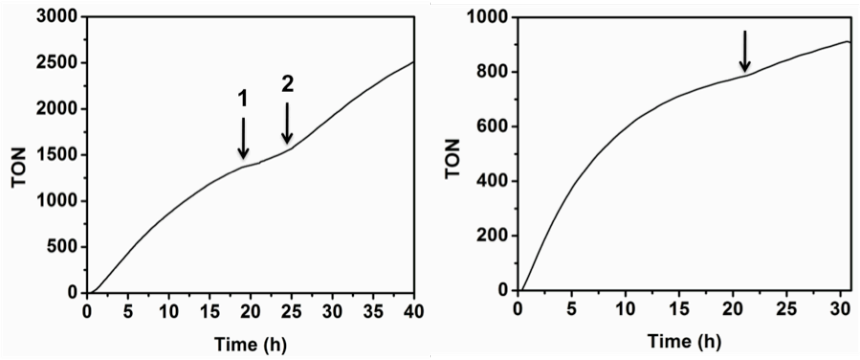

Figure 49: Photoinduced H_2 production of 4 μM M7A under continuous irradiation with 1100 W/m^2 light from a xenon arc lamp in a continuous flow detection system. Arrows in left graph correspond to addition of 1) 4 μM M7A and 2) 1 mM $Ru(Bpy)_3^{2+}$. Arrow in right graph corresponds to addition of 100 mM sodium ascorbate.

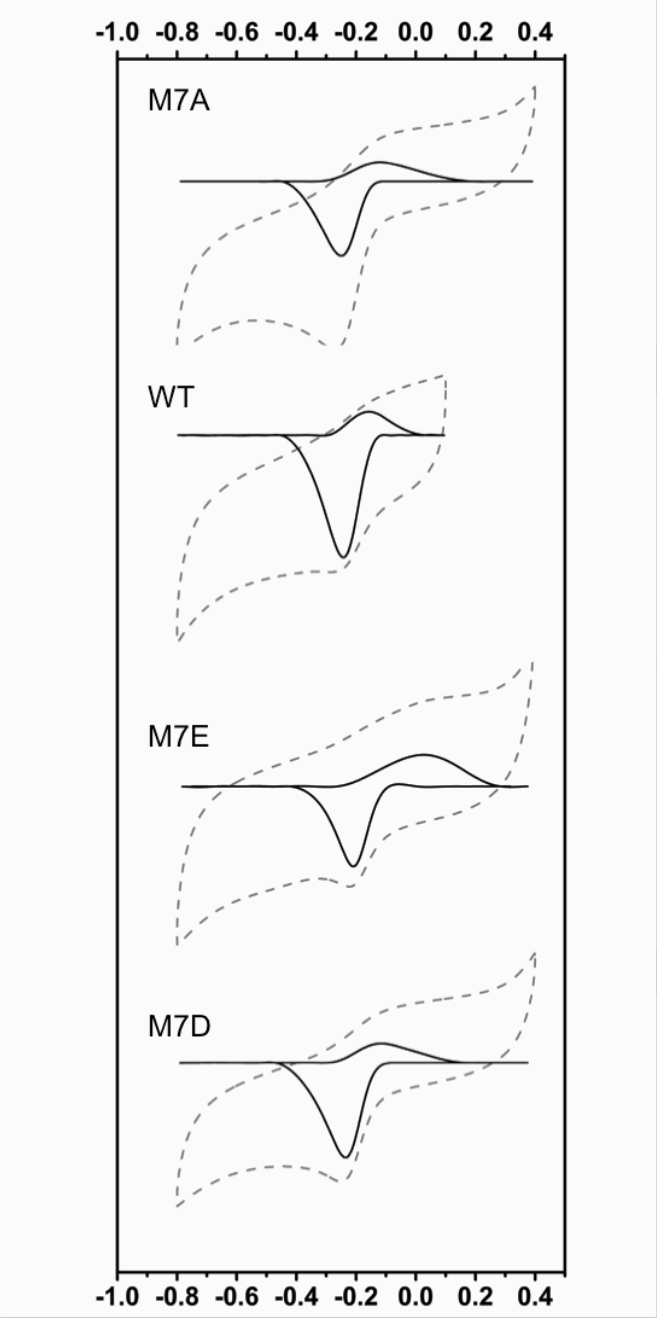

Figure 50: Cyclic voltammograms of the Co(II)/Co(III) couple for cyt b_{562} variants. Proteins were at a concentration of 28 μM in 100 mM Tris pH 7, 100 mM NaCl with a 0.28 cm^2 glassy carbon working electrode, platinum mesh counter, and SCE reference electrode.

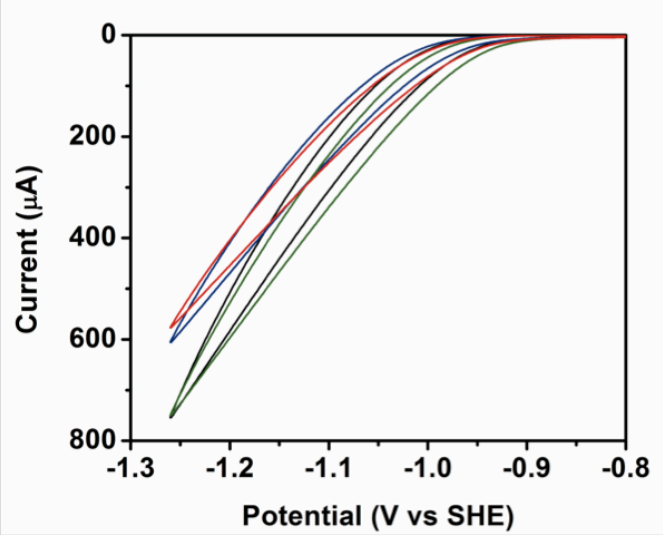

Figure 51: Cyclic Voltammograms of Cyt b_{562} variants in the catalytic region. Proteins were at a concentration of 28 μM in 100 mM Tris pH 7, 100 mM NaCl with a 0.28 cm^2 glassy carbon working electrode, platinum mesh counter, and SCE reference electrode. Traces correspond to CoWT (black), M7A (blue), M7D (red), M7E (green), and FeWT (gray).

To gain insights into the increased activity of M7D cytochrome as compared to the WT protein, we evaluated the redox properties of the Co(III)PP(IX)-bound proteins by cyclic voltammetry (CV). Scans from 0 to -0.8 V vs SCE revealed a single, reversible redox couple in the region characteristic of the Co(III)/Co(II) couple, with a redox potential for the WT protein of -225 mV (Figure 50). Compared to other cobalt porphyrin binding proteins with proton reduction activity, this value is more negative of CoMyo but positive of CoMP11. Removal of the axially coordinating methionine in M7A shifted the potential negative by 60 mV to -280 mV, while

coordination by the M7D variant resulted in a potential of -251 mV. The M7E mutant exhibits a redox potential positive of the WT protein at -209 mV. We carried out CV scans to -1.5 V vs SCE in order to drive electrocatalytic proton reduction. We found that the onset of the catalytic current, reflecting the overpotential needed to drive the reaction, is nearly indistinguishable between variants (Figure 51).

Analysis of the data collected on this system (Table 2) shows that the Co(III)/(II) redox potential values across the series align well with the catalytic efficiency of each variant. It has been shown that the activity of cobalt catalysts is increased as the basicity of the metal is increased, facilitating formation of the cobalt-hydride intermediate.[123, 135] With basicity increasing as a potential shifts negative, the M7A and M7D proteins should exhibit the highest activity. Although the wild type is more basic than M7E, the closed axial site inhibits catalytic turnover; the less-structured M7E allows for more turnover with the partially closed axial site.

Table 2: Summary of measured values for the Cyt b_{562} variants.

Variant	T_m (°C)	K_d (μM)	Midpoint Potential (V)	Activity (TON)
WT	85 (Co) 72.5 (Fe)	8.9	-225	125
M7A	64.2	10.8	-280	305
M7D	64.8	3.5	-251	275
M7E	61.4	13.5	-209	200

Cobalt-based catalysts have recently been shown to mediate H_2 electrocatalysis under oxygen-rich environments. Here, we explored whether cobalt porphyrins retain the ability to produce H_2 in the presence of oxygen by a photoinduced reduction. To do so we developed a continuous flow sensor that would maintain oxygen content in the cell while constantly purging produced H_2 from the reaction. Under anaerobic conditions, the M7A variant reached turnover numbers approaching 1500 in this apparatus. TON values are higher than in a closed-cell system because open conditions prevent product inhibition, which has been shown to reduce catalytic activity of cobalt porphyrins in photosensitized reactions.[136] Upon introduction of oxygen ranging from 10 to 21 percent, the TON of H_2 production decreased with increased O_2 content (Figure 52). Remarkably, production of H_2 under pure air resulted in a TON of 400. The decrease in TON attributed to competition with other reactions, namely reduction of O_2 and CO_2. The overall catalytic stability though is not affected by the introduction of air, as the catalyst is not destroyed by reactive oxidative species that are generated *in situ*.

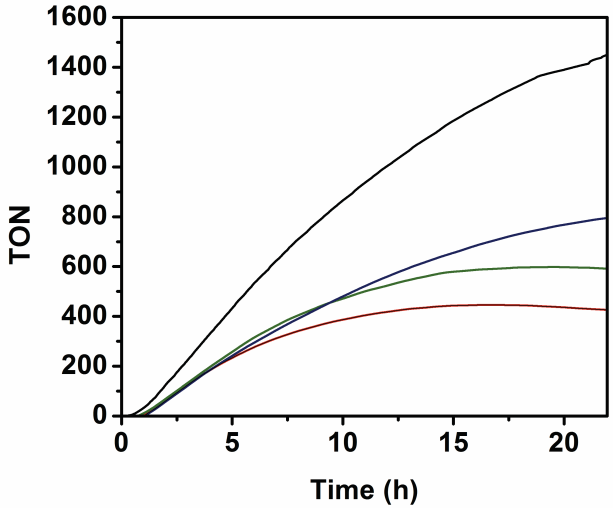

Figure 52: Photoinduced (410–770 nm) hydrogen production in a continuous flow reactor with 1 M KPi with 0.1 M sodium ascorbate and 1 mM $Ru(bpy)_3^{2+}$ at pH 7, traces correspond to anaerobic (black), 10% O_2 (blue), 15% O_2 (green), and 21% O_2 (red).

In summary, we have reengineered a natural electron transfer protein to catalyze the production of H_2 both electrochemically and photochemically. The activity of the engineered enzyme was modulated through mutagenesis in the primary sphere of the catalytic cofactor, with a "hangman" mutation allowing for high levels of activity relative to the WT protein. The cobalt porphyrin system is able to produce H_2 photochemically in 100% air, a property not common to hydrogen-production catalysts. The designed system offers the chance for scalable photocatalysis, as it can be produced in high amounts with cheap precursors.

CHAPTER 4

COMPUTATIONAL DESIGN AND CHARACTERIZATION OF CO_2 REDUCTION CATALYSTS

4.1 Introduction

Ever since the industrial revolution, society has relied on fossil fuels to power economies, burning coal, oil, and natural gas to supply energy to a growing population, but combustion of these fuels has become an overwhelmingly large anthropogenic source of CO_2, a potent greenhouse gas. As research efforts have focused on development of alternative energy sources such as solar, wind, or biofuels, the remediation of CO_2 is also a pressing concern. Remediation of CO_2 into fuels or useful chemical precursors offers a realistic solution to the high levels of atmospheric CO_2, provided that suitable catalysts are developed to carry out the conversion.[137-140]

Past efforts in this field have identified two types of materials (homogenous and heterogenous) for the conversion of CO_2 to products such as CO, formate, and methanol. While both have their advantages and disadvantages, both are plagued with the issue of selectivity, where the reduction of CO_2 proceeds to form multiple types of products, leading to issues in the use these products downstream.[138] Heterogenous catalysts, namely metal surfaces, efficiently catalyze the CO_2 reduction reaction. While these catalysts allow product selectivity to be altered based on the overpotential applied, high percentage of selectivity has yet to be achieved.[141] Furthermore, these materials are easily poisoned by the products of the

reaction and are made of expensive transition metals such as Pd. The second type is homogenous catalysts, the so-called molecular catalysts.[140] Unlike their homogenous catalyst counterparts, molecular catalysts are not easily poisoned by reaction products, although they often function at very high overpotentials and degrade in short periods of times. While many of these catalysts are also based on precious metals such as Re, a number of catalysts based on abundant transition metals such as Co and Fe have surfaced as candidates for technological approaches.[142-144]

One of the most well characterized families of homogenous CO_2 reduction catalysts is the *fac*-[Re(α-diimine)$(CO)_3$X]$^{n+}$ (X = halide, n = 0 or X = neutral ligand, n = 1), which selectively reduce CO_2 to CO.[145-150] This reduction product is desirable, as it is readily removed from the reaction mixture and fed into downstream organic processes. The conversion with this family can be carried out via either electrochemical or photochemical (both in the presence and absence of a photosensitizer) methods, proceeding through both 1-electron and 2-electron mechanisms.[150] It is due to the interesting variances in the mechanism, as well as the synthetic ease of working with diimine complexes, that these catalysts have been so extensively computationally and experimentally characterized. Further, their properties can be modulated by installation of proton-responsive sites on the ligand, providing the means for proton shuttling and storage of hydrogen when required. However only a single report exists of use of this family doing homogenous catalysis in aqueous systems, therefore the mechanism of function and selectivity in this solvent is not well understood.[151]

An alternative class is the cobalt, nickel, and iron porphyrins, which have long been utilized as both electrochemical and photochemical CO_2 reduction catalyst.[105] Initial work in the field using cobalt porphyrins extensively characterized the photophysical properties of a range of porphyrins, establishing a basic structure/function relationship between the electronic properties of the macrocycle and the catalytic capabilities.[136, 152-154] Further work in the area using iron porphyrins as electrocatalysts showed the ability of external proton sources substituted on the ring can enhance the rate of reaction through stabilizing the CO_2 adduct, implicating their use in designed protein systems.[142] These macrocyclic Co or Ni complexes face their own disadvantages, as they too function at high overpotentials in non-aqueous conditions, with only recent reports showing activity of an iron porphyrin in water, which produced formate, H_2, and CO at the same time (while only producing H_2 and CO in organic solvents).

To address these issues nature can serve as inspiration, as redox active enzymes are non-promiscuous and function near thermodynamic redox couples in aqueous solutions.[155-157] Enzymes are able to overcome the problem of selectivity by providing three-dimensional contracts around the catalytic site, sterically and kinetically favoring particular pathways by tuning reaction thermodynamics. Both heterogenous and homogenous catalysts cannot provide these same contacts due to synthetic infeasibility, implicating the use of proteins for redox reactions that can produce a number of products.

Additionally, due to the difficult nature of one electron reduction of CO to $CO^{-\bullet}$ (-2.14 V vs SCE), utilization of multiple proton-coupled electron transfer (PCET) events lowers the potential required to obtain useful products.[158] Natural enzymes carry out PCET reactions with high reaction rates of ~5000 s^{-1}, obtaining 100% efficiency, and in aqueous, neutral pH, room temperature conditions, by stabilizing reaction intermediates with the aforementioned critical protein contacts.[6] Coupled with these high rates, proteins are easily interfaced with solid materials for inclusion into solar fuel cells. Redesigning of natural enzymes for CO_2 reduction has had some recent success, but complex protein maturation pathways and instability of natural enzymes limit the field.[155]

In order to delve deeper into the role that proteins can play in altering selectivity of redox reactions, as well as to gain further insight into the mechanisms by which redox reactions occur in artificial metalloenzymes, we set out to develop a general methodology to design artificial metalloenzymes. The first example to be discussed will be the cobalt cytochrome b_{562} system, discussed in chapter 3, an optimal system to benchmark the developed methodology. Here I present both the computational and experimental characterization of the CoCyt-b_{562} system, showing the first example of an artificial metalloenzyme altering the redox reaction specificity of an artificial catalyst, as well as a general method for the computational prediction of mutations in the artificial enzymes that may alter the reaction specificity. The second example will utilize an alternative design approach, based on the biotin-avidin technology developed by Whitesites and Wards, to incorporate a

rhenium tricarbonyl catalyst into a protein system.[159] Here I will present full a computational mechanistic investigation of the designed catalytic system in water, finally proposing a novel reaction mechanism for the family of catalysts. I will also present transient spectroscopic investigation into the role the protein is playing in the photoinduced reaction.

4.2 Materials and Methods

General Methods

All chemicals were purchased from commercial suppliers unless otherwise noted. Dry solvents were purchased from Sigma-Aldrich and used without further purification. Tetrabutylammonium hexafluorophosphate (NBu_4PF_6) was recrystallized twice from water prior to use. UV-vis spectra were recorded on a Cary-50 instrument with a 1-cm pathlength cuvette. IR spectra were recorded on a Bruker Vertex 70 series instrument on a CaF_2 window after drying samples onto the surface under vacuum. CD spectra were recorded as outlined in chapter 3.

Catalyst Synthesis

Rhenium-biotin was synthesized in a two-step reaction. D-biotin (500 mg, 2.05 mmol), 1,10-phenanthroline-5-amine (400 mg, 2.05 mmol), HATU (700 mg), and DIPEA (775 μL) were dissolved in 20 mL of anhydrous DMF. The reaction placed under argon, warmed to 50 °C, and stirred for 16 h. DMF was removed under reduced pressure and the resulting residue purified via inactivated silica chromatography (1:9 MeOH:DCM) affording the biotin-phenanthroline in 80% yield as confirmed by NMR and MALDI-TOF-TOF MS.

Biotin-phenanthroline (100mg, 0.24 mmol) and [$Re(CO)_5Cl$] (86 mg, 0.24 mmol) were dissolved in anhydrous DMF under argon. The reaction was refluxed for 16 hours and the solvent removed under reduced vacuum. The resulting oil was purified via silica chromatography, (1:9 MeOH:DCM) obtaining biotin-rhenium (BRe) in 95% yield, confirmed using MALDI-TOF and H-NMR.

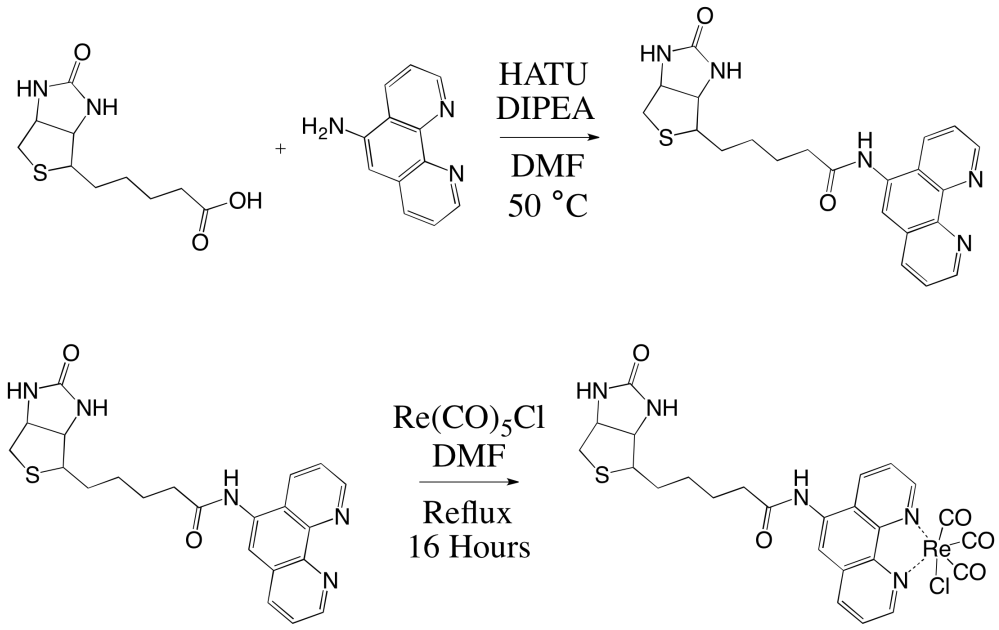

Figure 53: BRe two-step synthetic scheme

Protein Expression and Purification

Cytochrome b_{562} mutants were generated purified, and reconstituted with cobalt protoporphyrin IX as described in chapter 2, affording the pure proteins in excess of 99% purity.

Rhenium-Streptavidin (SA-BRe) was prepared in batches by mixing 10 mg of commercially available streptavidin (Prozyme), dissolved in 100 mM Tris-HCl pH 8, with 10x molar excess of the BRe complex dissolved in DMSO. Samples were incubated overnight at 4 °C, followed by removal of excess complex by subjecting the protein to PD-10 desalting columns (GE-healthcare). Presence of the complex was confirmed by IR and UV-vis spectroscopy.

Computational Methodologies

All geometries were fully optimized at the either the MO6 or M06L level of density functional theory with the SMD continuum solvation model for water as solvent using the SDS contracted pseudopotential basis set on Co or CEP contracted pseudopotential basis set for Re and the 6-31G(d) basis set on all other atoms. Non-analytical integrals were evaluated using the integral=grid=ultrafine option as implemented in the Gaussian 09 software package. Free-energy contributions were added to single-point M06 electronic energies computed with the SDD basis set on Co, CEP for Re, and the 6- 311+G(2df,p) basis set on all other atoms to arrive at final, composite free energies.

Photoinduced CO_2 Reduction Activity Determination

CO_2 reduction ability of both designed catalysts was assayed in a well characterized system containing ruthenium bipyridine, $Ru(Bpy)_3^{2+}$ in the presence of a sacrificial electron donor, ascorbic acid. Buffers were prepared by dissolving 100 mM ascorbic acid in water, followed by saturation of the buffer with CO_2. The pH of each buffer was then adjusted to the appropriate level (4, 4.5, 5, 6) through

addition of 1M KOH. For the photochemical assay, $Ru(Bpy)_3^{2+}$ was added to a final concentration of 1 mM, as well as the catalyst to the appropriate concentrations. Samples were placed in airtight 1 mm cuvettes, sparged with CO_2 for 20 minutes, followed by illumination with a Xenon lamp filtered through a $CuSO_4$ water filter, for 8 hours. Reaction progress was monitored by removing aliquots of headspace volume for injection onto a Agilent 6890N network GC system (columns: GS-CARBON-PLOT 15 m ´ 0.32 mm ´ 1.5 mm; HP-MOLSIV 30 m ´ 0.32 mm ´ 12 mm) with a custom built methanizer for simultaneous detection of H_2 and CO. Formate was analyzed by injection onto a Dionex ICS-1600 ion chromatography (IC) system equilibrated in 30 mM NaOH, and compared to standard formate integration areas.

Transient Absorption Spectroscopy

Transient absorption and emission lifetime experiments were performed using a home-built instrument described elsewhere where the excitation was provided by an Opotek Vibrant LD 355 II OPO laser (420 nm, 1 mJ per pulse) at 5 Hz. For transient absorption measurements, the sample was probed by a pulsed 150 W Xe arc lamp in a 90° beam geometry arrangement and a Tetronix DPO40332 digital oscilloscope (350 MHz, 2.5GS s^{-1}) was used to digitize the transient signals obtained with a Hamamatsu R928 PMT detector. The sample cuvette was placed in a cell holder equipped with thermostat, and the temperature was maintained at about 25°C. The probe light was filtered through a combination of longpass and shortpass filters to avoid unnecessary irradiation of the sample.

Electrochemical Methods

All electrochemical experiments of catalysts alone (1 mM catalyst concentration) were carried out in dry DMF with 0.1 M recrystallized NBu_4PF_6 using a three electrode setup: 0.3 cm^2 glassy carbon working electrode, platinum mesh counter electrode, and a silver wire as pseudo reference. All experiments were referenced to the ferrocene couple, +450 mV vs SHE in DMF. For protein electrochemistry, 100 mM Tris HCl pH 7, 100 mM NaCl, and 3 mM neomycine as a redox mediator were used. The same working and counter electrode were used, however a 3M Ag/AgCl reference was employed for aqueous measurements.

4.3 Computational and Experimental Analysis of Cobalt Cyt b_{562} for CO_2 Reduction

Nature is able to efficiently catalyze the reduction of CO_2 to a single product using multiple PCET steps with enzymes such as Carbon Monoxide Dehydrogenase or Formate Dehydrogenase.[155, 157] Catalysts designed based off the active site structure of these enzymes, or artificial catalysts, either fail to obtain reactivity, or do not exhibit the same selectivity as the enzyme itself.[156] This implicates the protein in playing a crucial role in stabilizing key intermediates as well as providing stereoselectivity during the reaction, tuning thermodynamic pathways to favor a single reaction pathway over another. It is often challenging to study these types of interactions in nature due to the complex maturation pathways seen with large, multidomain proteins that carry out the reactions, as well as the complex cofactors employed by the proteins themselves.

In order to study the role that proteins can play in artificial catalyst's reaction pathways, we chose to explore the cobalt cytochrome b_{562} system. Previous work on computational characterization of CO_2 reduction catalysts has found that the selectivity in these reactions is kinetically controlled, instead of thermodynamically controlled as is generally expected.[160, 161] With the CoCyt-b_{562} system exhibiting a bis-axial ligation (Figure 54), it is optimal to alter the kinetics of the cobalt protoporphyrin reaction via steric hindrance of products accessing the catalytic pocket. The prior work on the system has also shown our ability to modulate the axial ligands of the system, making it a prime system to establish structure-function relationships for a number of amino acids occupying that position.[162]

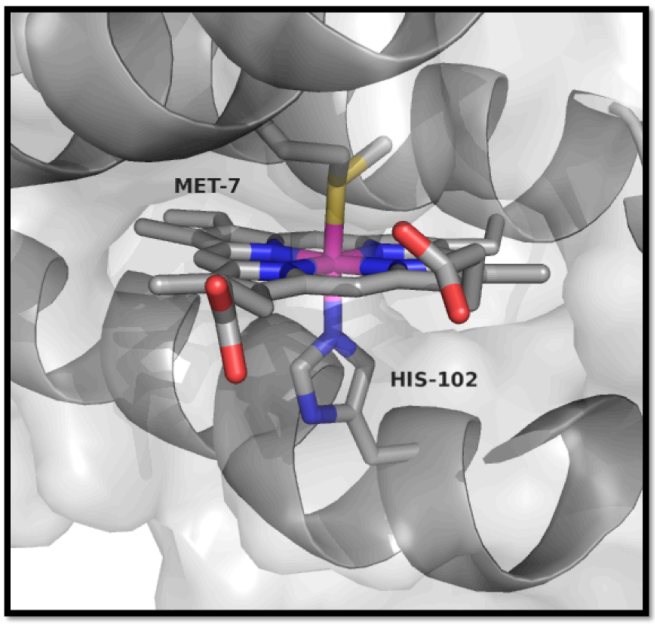

Figure 54: Active site of Fe Cytochrome b_{562} (PDB 1QPU) highlighting the coordinating residues Met7 and His-107.

While there has been reactive mechanisms proposed for both H^+ and CO_2 reduction by cobalt porphyrins, there has been little work which models the catalytic cycle or looks at the driving factors for the selectivity seen in porphyrin systems, inspiring us to do a full DFT modeling of the cycle in water before experimentally characterizing the system. We began by optimizing the closed-shell singlet resting state of cobalt protoporphyin IX, Co(III), bound axially by ligands that should mimic the protein environment, water and methyl imidazole in a continuous SMD aqueous solvation model. (Figure 55) To avoid unwanted hydrogen bonding and ionic interactions between the propionic acid arms, two explicit water molecules were placed to hydrogen bond to the arms. Upon reduction of the system to a doublet Co(II), the axial water ligand is lost, providing a site for the reaction to occur upon further reduction. Finally, the Co(I) singlet and Co(0) doublet states were optimized in the square planar geometry, showing the loss of all protein direct contacts to the metal center. The calculated reduction potentials for the optimized cycle in comparison to experimental values are shown in Table 3.

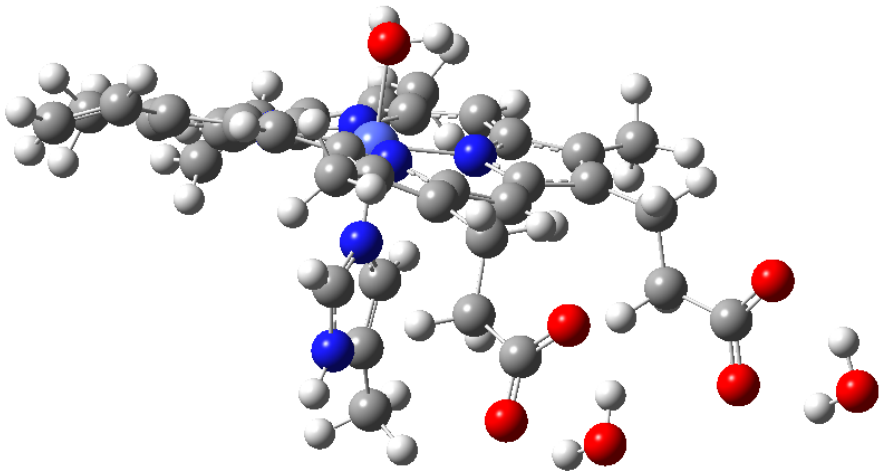

Figure 55: DFT model of the cobalt protoporphyrin IX catalyst.

Table 3: Computationally predicted and experimentally measured midpoint potentials for cobalt protoporphyrin IX

Couple	DFT	Experimental	Difference
Co(III)/(II)	427	N/A	N/A
Co(II)/(I)	-395	-750	355
Co(I)/(0)	-1793	-1880	87

*All potentials measured mV vs SHE, experimental in DMF with 0.1 M NBu_4PF_6

In the literature, there is a debate whether the Co(I) or Co(0) state are the catalytically active state for cobalt porphyrins for both CO_2 and H^+ reduction, due to conflicting electrochemical results and prior experience with cobaloximes.[99, 105-107, 163] To aid in answering this question, both the Co(I) and Co(0) states were chosen

for both a H^+ addition, forming Co(III) or Co(II) hydride, or CO_2 binding; these are the key steps in the catalytic cycle for determining whether formate or H_2 will be formed (hydride) or CO (CO_2). Both states showed reasonable thermodynamic values for reaction to proceed, as summarized in Figure 56, implicating Co(I) as the probable catalytically active state for the reaction in water.

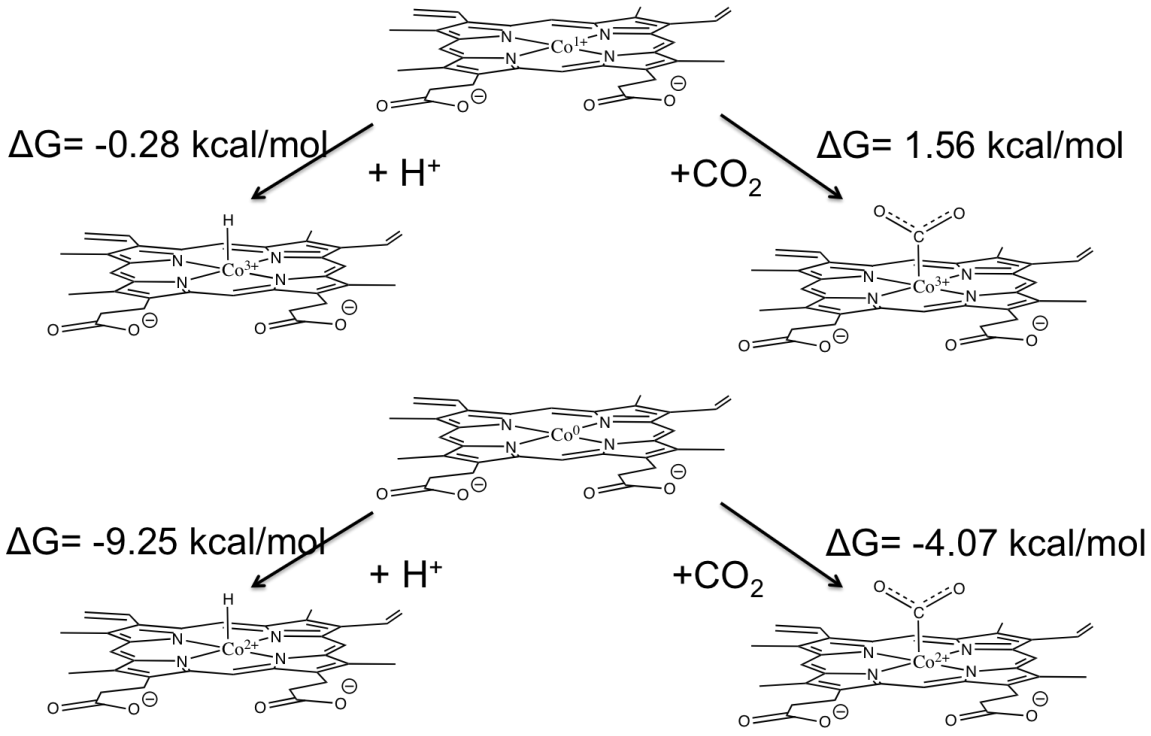

Figure 56: Calculated free energy changes upon proton or CO_2 binding to cobalt protoporphyin IX at the +1 or 0 oxidation state.

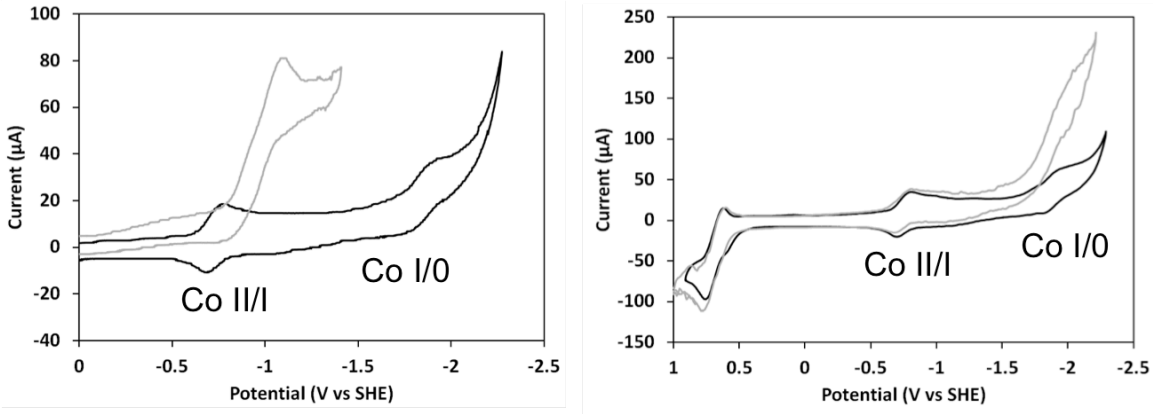

Figure 57: Cyclic voltammograms of CoPP(IX)DME in the absence (black) or presence (gray) of tosic (left) or acetic (right) acid, measured in DMF with 0.1 M NBu_4PF_6, 100 mV/sec

In order to confirm these predictions, I carried out cyclic voltammetry experiments on the analogous cobalt protoporphyrin IX dimethyl ester, CoPP(IX)DME, which is soluble in DMF. In these experimental conditions under argon, two reductive peaks are seen which correspond to the Co(II)/(I) and Co(I)/(0) couples. The observed couples align well with computationally predicted values, as outlined in Table 3. The small discrepancy seen in the values was attributed to the variances in the dielectric constant of the solvent, and the absence of imidazole in the electrochemical setup, as the Co(II)/(I) couple which involves the loss of a coordinating imidazole is the most affected. To identify the potential at which protons bind to form the hydride the porphyrin was titrated with two acids, acetic acid (pK_a = 13.2) and tosic acid (dissociated fully in DMF).[164] By using this relatively weak (acetic) and strong (tosic) acid, the Co(0) state and Co(I) state went

catalytic respectively, as shown in Figure 57. Due to the relatively high concentration of hydronium in water, it follows that in water the Co(I) potential is the catalytically active state.

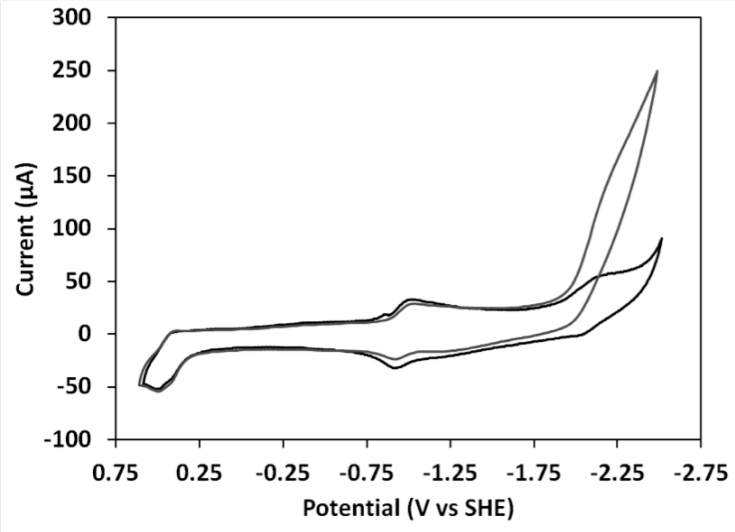

Figure 58: Cyclic voltammogram of CoPP(IX)DME under argon (black) or CO_2 (gray) in DMF, 0.1 M NBu_4PF_6, 100 mV/sec

In the absence of acid, the solution was flushed with CO_2. (Figure 58) In the presence of CO_2 in DMF, the Co(I)/(0) couple went catalytic, in agreement with what was previously seen with cobalt porphyrins.[154] This did not bode well for the computational predictions though, as Co(I) was predicted to be the catalytically active state. Previous work on cobalt porphyrins saw catalytic waves at much more positive potentials in water, indicative that in water the Co(I) state is indeed catalytic, supporting our computational predictions.[108, 162] We attribute this

difference due to the hydrogen bonding abilities of water, as the CO_2 adduct will be sufficiently stabilized in water to allow the Co(I) reaction to proceed, while in organic solvents the transient nature of this complex precludes reactivity.

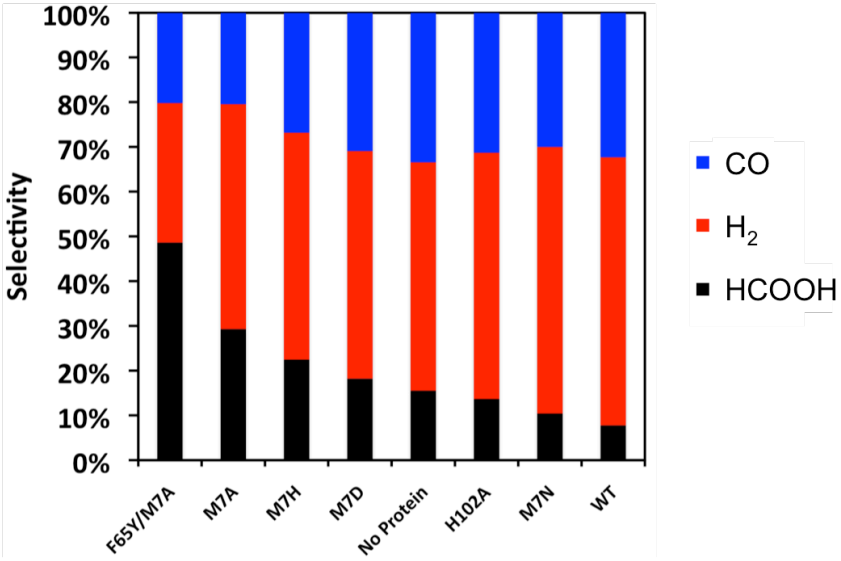

Figure 59: Photoinduced CO_2 reduction catalyzed by CoPP(IX) and CoCyt b_{562} variants, with selectivity reported as % of total turnovers of each catalyst. Conditions: 100 mM ascorbic acid, 1 atm CO_2, 1 mM $Ru(Bpy)_3^{2+}$, pH 6

While the computational model was being developed, we began to assay the ability of the biohybrid cyt b_{562}/CoPP(IX) system to reduce CO_2 photocatalytically in aqueous conditions at pH 6. In this experimental setup, $Ru(Bpy)_3^{2+}$ acts as a photosensitizer to absorb white light, followed by a rapid reductive quenching of the photoexcited triplet state by ascorbic acid, a sacrificial electron donor. This highly reducing (-1.26 V vs SHE) molecule can then reduce the biohybrid system

sequentially through its catalytic cycle. Under these conditions, in the absence of protein, CoPP(IX) efficiently reduces CO_2 and H^+ in a non selective manner. (Figure 59) Under the same conditions, we assayed seven different variants of the cytochrome b_{562} scaffold, as summarized in Figure 59. Interestingly, the best mutants were able to tune the selectivity of the reaction towards either H_2 or formate, in comparison to the protein-free catalytic system, which produced the most CO of all the catalysts tested. The best catalyst for selective H_2 production surprisingly was the wild-type scaffold, which had the lowest turnover numbers from previous work. We believe this decrease in formate and CO production is due to the steric hindrance of the axial methionine ligand, which is not a good H-bond donor to facilitate CO_2 entering the active site. On the other side of the series is the only double mutant assayed, F65Y/M7A. The M7A mutation serves to open the active site to substrate molecules, in agreement with prior work on the system, while the F65Y mutation was done to provide a hydrogen bonding donor to facilitate CO_2 entering the pocket; this mutant has the highest overall products for CO_2 reduction, indicating the success of our design strategy.

The next step in the computational method development was to develop a DTF model that accurately recapitulates the electronic effects that the proteins play on cobalt porphyrins. By examining the structure of CoCyt-b_{562}, we noted that the designed active site is only comprised of ~10 amino acids, in comparison to the 106 in the full-length protein. By trimming away the excess amino acids, the features of the active site are maintained, however the model is significantly reduced in size to

facilitate computational turnover. (Figure 60) To benchmark this method, we began first by doing artificial "mutagenesis," that is changing the organic axial ligands in the small molecule, to see how they compare to the larger model. In doing so, we are able to successfully mimic the change in electronic density around the cobalt center that is seen in the proteins, summarized in Table 4. Inspired by this success, future work will move to the larger model, optimizing the Co(I) state in order to assess the electronic density in the protein active site, as well as to determine the kinetic factors that are altering the selectivity between H_2, CO, and formate.

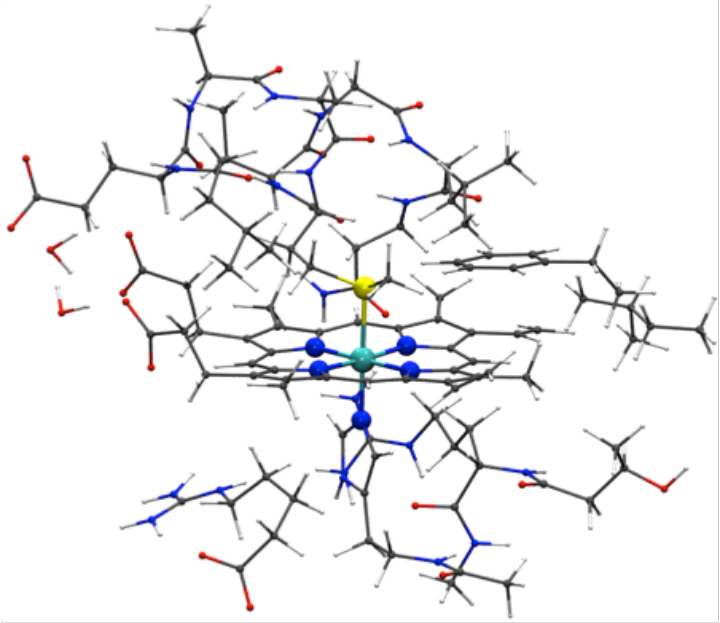

Figure 60: DFT model of CoCyt b_{562} to be used in futures studies.

Table 4: Comparison of DFT model midpoint potentials with various computational methods compared to experimentally measured value.

Functional	E (Co(III)/Co(II)) in V vs NHE
BP86	-0.81
B3LYP	-0.49
M06	-0.20
Experimental	-0.225

The presented work on the CoCyt-b_{562} system shows the ability of natural protein scaffolds to alter the reaction specificity of artificial redox catalysts, the first example in the field of artificial metalloenzyme design. As the project moves forward, with the developed computational methods in hand, scaffolds with enhanced selectivity towards CO and formate will be designed in order to obtain selective redox catalysis in aqueous systems. Future work will switch to alternative catalysts in order to benchmark the described approach, assessing the generality of the developed method while elucidating key design principles for artificial metalloenzymes.

4.4 Rhenium Streptavadin as a Tunable CO_2 Reducing Enzyme

Currently, natural metalloenzymes are the gold standard for carrying out redox reactions at thermodynamic potentials and high rates, but along with the

problems mentioned earlier (large size, O_2 sensitivity, and complex maturation pathways), natural enzymes are also limited by types of elements that are provided in nature. Besides the typical C, N, O, S, and P required for protein maturation, the availability of metals has shaped biology to utilize particular types of metals in proteins.[165] For instance, high availability of Fe and S in prebiotic earth led to the formation of iron sulfur clusters for electron transfer; these clusters are still utilized today even though current oxygenic conditions reduce availability of Fe and readily degrade the clusters.[166] While the enzymes that nature employs are able to carry out the reaction, recently researchers have started to look into designing artificial metalloenzymes with non-biologically available metals to see if an enzyme can be developed with properties better than those seen in nature.[159]

Over the years molecular catalysts bearing Ru, Re, Pd, Pt, Rh, Os, and Ir have been reported that are able to carry out energetically-relevant reactions at relatively high rates and at low overpotentials.[140] One of the most well studied families of catalysts is the *fac*-[Re(α-diimine)$(CO)_3$X]n+ (X = halide, n = 0 or X = neutral ligand, n = 1) family of catalysts, which selectively reduce CO_2 to CO.[167] This system is optimal for inclusion into protein scaffolds to study the ability of proteins to interface with non-earth abundant metals, as Mn has been utilized as a substitute to Re in the family and will allow for comparison of protein influence on properties for both types of metals.[168] On top of the ease of comparison to alternate metals, the ease of altering the chelating diimine ligands has led to reports of numerous catalysts which include proton reponsive units in the proximity of the catalytic site,

showing the ability of catalytic properties to be modulated with primary and secondary shell interactions.[96, 167, 169, 170]

Unlike prior work in this thesis, which has focused on utilizing natural intractions to house artificial catalysts into proteins scaffolds, there is no known affinity for diimine ligands found in nature. For the desired catalyst to be incorporated into a protein an alternative approach was required; utilization of a strong protein/ligand affinity to facilitate cofactor incorporation. One of the strongest protein/ligand interactions found in nature is the streptavidin/biotin interaction, having a K_d in the low picomolar range.[159] Another advantage to this system is the easy of functionalization of the biotin molecule, as a free carboxylic acid which is solvent exposed in the protein/ligand conjugate is easily functionalized with any chemical moiety of choice. This system has been extensively by the groups of Whitesides and Ward, showing the ability of the protein system to alter the catalytic properties of unnatural catalysts.

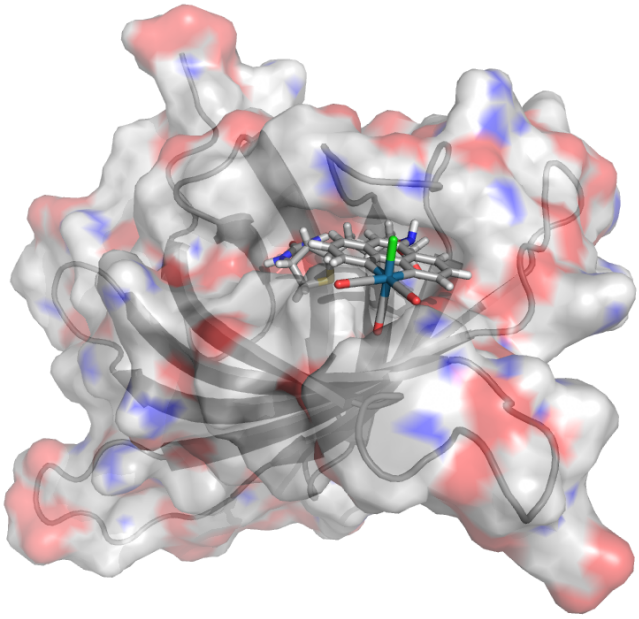

Figure 61: Molecular dynamics minimized model of SA-BRe

To facilitate this interaction, we first synthesized a biotinylated diimine ligand based off the commercially available phenanthroline molecule, which modeled well into the streptavidin core. (Figure 52, 60) The desired catalyst, BRe, was readily obtained in high yields and purities using a short two step synthetic scheme. With the metal catalyst in hand, binding stoichiometry for BRe with streptavidin was analyzed using the well-established 4'- hydroxyazobenzene-2-carboxylic acid (HABA) displacement assay.[171] (Figure 62) In this assay, HABA binds to streptavidin (SA) with low micromolar dissociation constant, which gives rise to absorbance near 500 nm. In a typical HABA displacement assay, 10 μM of Streptavidin in 20 mM phosphate, 150 mM NaCl, pH 7.5 was saturated with 500 uM HABA. After incubation at room temperature for 30 minutes, resulting solution was

used for spectrophotometric titration. From a stock DMSO solution of BRe, incremental amount of ligand were added to the HABA saturated Streptavidin, and decrease of absorbance at 500nm was monitored as a function ligand concentration. The titration curve shown in 1B indicates that BRe binds to SA with (0.9:1) ratio, which is in agreement with the reported activity of commercial SA that was used in the assay.

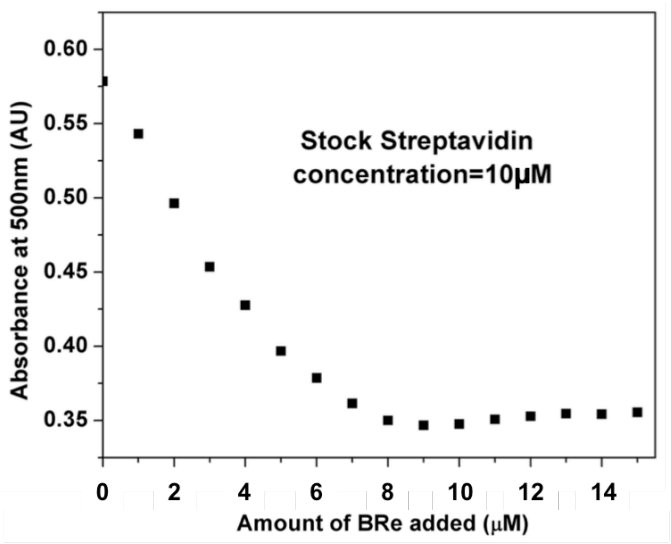

Figure 62: UV-vis monitored sequential titration of HABA-Streptavidin complex with BRe, showing loss of absorbance at 450 nm.

Inspired by BRe binding to SA with high affinity, we then turned to characterize the specroscopic properties of the designed metalloenzyme. The synthesized complex exhibited a typical UV-vis spectrum of the family of catalysts, with a broad, high energy metal-to-ligand charge transfer (MLCT) band centered at

380 nm, in agreement with similar complexes synthesized previously. (Figure 63) Large scale preps of the SA-BRe system lead to a similar UV-vis trace, along with a significant contribution at 280 nm from the tryptophan absorbance of the protein, indicicating successful incorporation of the catalyst into the protein hydrophobic pocket.

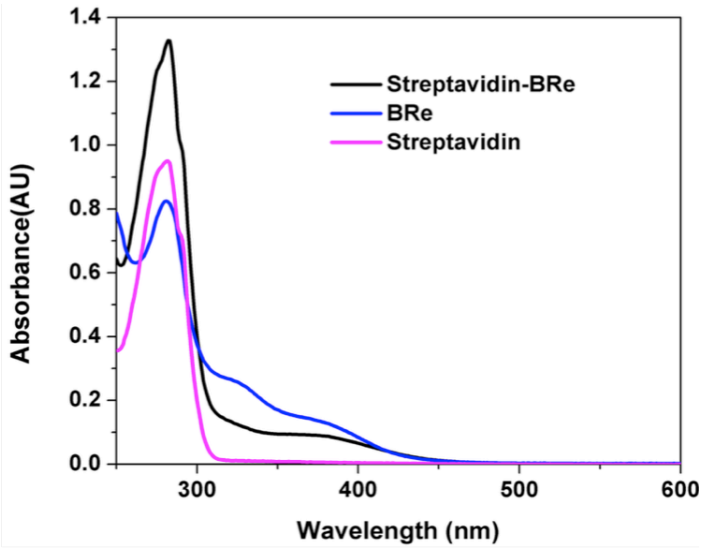

Figure 63: UV-Vis spectra of BRe, Streptavidin, and SA-Bre

Another technique utilized to assess the local environment of incorporated catalysts is IR spectroscopy, as stretching frequencies can be easily altered by solvent accessibility and electrostatics. The designed catalyst's ν(CO) frequencies were monitored both in the absence and presence of protein using FTIR. (Figure 64) The BRe complex alone, deposited in a thin film on a CaF_2 window from a methanol stock solution, exhibited three CO stretches at 2023, 1910, and 1891 cm^{-1}. For the

Streptavidin-Bre trace, a stock solution of streptavidin in water was treated with BRe from a DMSO stock solution with (1.5:1) molar ratio. The resulting solution was placed on the CaF_2 window and dried under vacuum to generate the thin film. Under these conditions the SA-BRe complex exhibits three stretches in the same region as the BRe system at 2028, 1924, and 1905 cm^{-1}. The three CO stretches are all shifted to higher energy stretching frequencies than the complex alone. We attribute this shift to the complex existing in a solvent-protected state, whereas solvent molecules can no longer H-bond with the CO ligands, therefore increasing the bond strength and therefore stretching frequency.

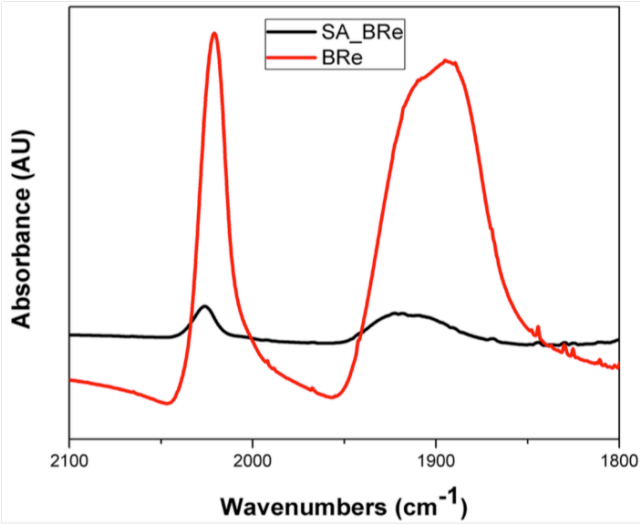

Figure 64: Thin film FTIR spectra of BRe and SA-BRe, taken on a KBr pellet.

To characterize the CO_2 reduction ability of the design catalysts in an aqueous system, we utilized a well-characterized photosensitized system comprised

of ruthenium bipyridine ($Ru(Bpy)_3^{2+}$) as a visible light photosensitizer and ascorbic acid as a sacrificial electron donor. Upon continuous illumination of both BRe and SA-BRe under a CO_2 atmosphere, both CO and H_2 can be detected in the headspace of the reaction mixture. (Figure 65) Soluble CO_2 reduction products were assayed for after 8 hours of continuous illumination by injection of aliquots of the reaction mixture onto an ion chromatography system, where formate was detected for both catalysts characterized. During the time period assayed, the TON for the BRe system was 42 while the SA-BRe system underwent 119 turnovers, an enhancement of 2.8 which agrees well with previous work. Interestingly, inclusion of the catalyst into the protein pocket shifts the CO_2 reduction specificity from primarily formate for the catalyst alone to a mixture of CO and formate for the protein system, with both producing similar amounts of H_2.

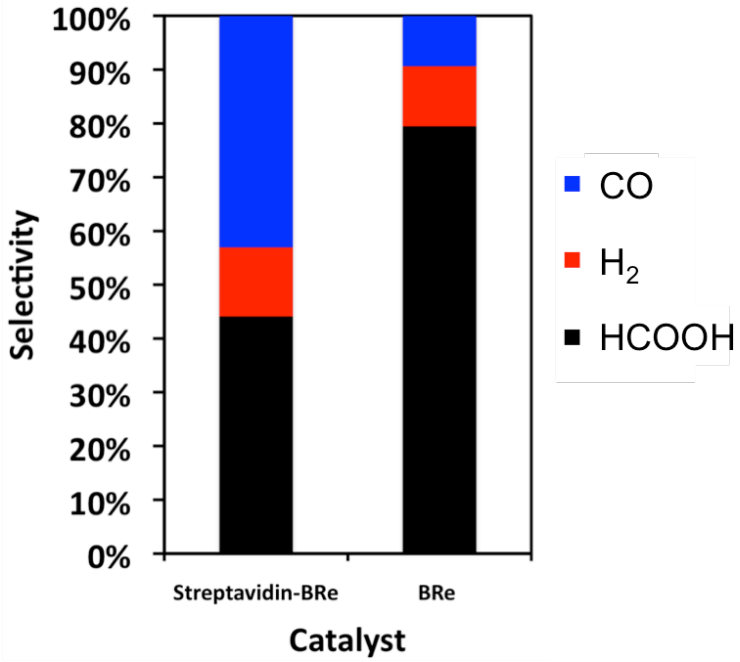

Figure 65: Photoinduced CO_2 reduction catalyzed by BRe and SA-BRe, with selectivity reported as % of total turnovers of each catalyst. Conditions: 100 mM ascorbic acid, 1 atm CO_2, 1 mM $Ru(Bpy)_3^{2+}$, 10% DMF, pH 6

To aid in determining the mechanism by which protein confinement enhances the catalytic ability of the rhenium catalyst, we utilized transient absorption spectroscopy, a pump-probe type experiment. We first explored $Ru(Bpy)_3^{2+}$ and BRe alone in a mixed solvent system and ascorbic acid as a reductive quencher. By pumping the molecules with a 332 nm laser, and probing from 350-700 nm, we were able to identify signature bands corresponding to the catalytically relevant states. (Figures 66 and 67) Upon excitation of $Ru(Bpy)_3^{2+}$, the MLCT band undergoes rapid quenching along with a board absorbance at wavelengths above

600 nm, which we attribute to the triplet state. This is then reductively quenched and leads to formation of a persistent signal at 510 nm, attributed to the singly-reduced state responsible for electron transfer to the catalyst in the photochemical system.

Similarly, photoexcited BRe exhibits signals at 360 and 510 nm, attributed to the excited state, which decay rapidly to a persistent signal at 580 nm, the singly-reduced BRe signal. (Figure 67) Examining the kinetics of the signal at 580 nm the lifetime of the Re(0) state can be monitored, a state of importance along the proposed catalytic cycle. (Figure 68) In the absence of protein the Re(0) decays within 250 μs via charge recombination pathways. Upon inclusion of streptavidin into the system the Re(0) lifetime increases significantly to over 500 μs, facilitating turnover of the bound catalyst.

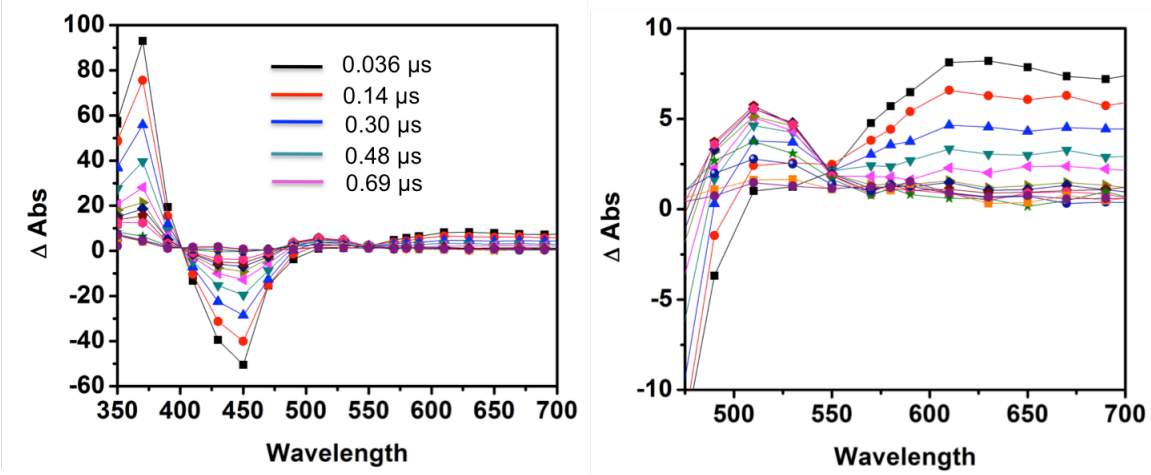

Figure 66: Transient absorption spectra of $Ru(Bpy)_3^{2+}$ at the indicated time points. Spectra correspond to full (left) and scaled (right).

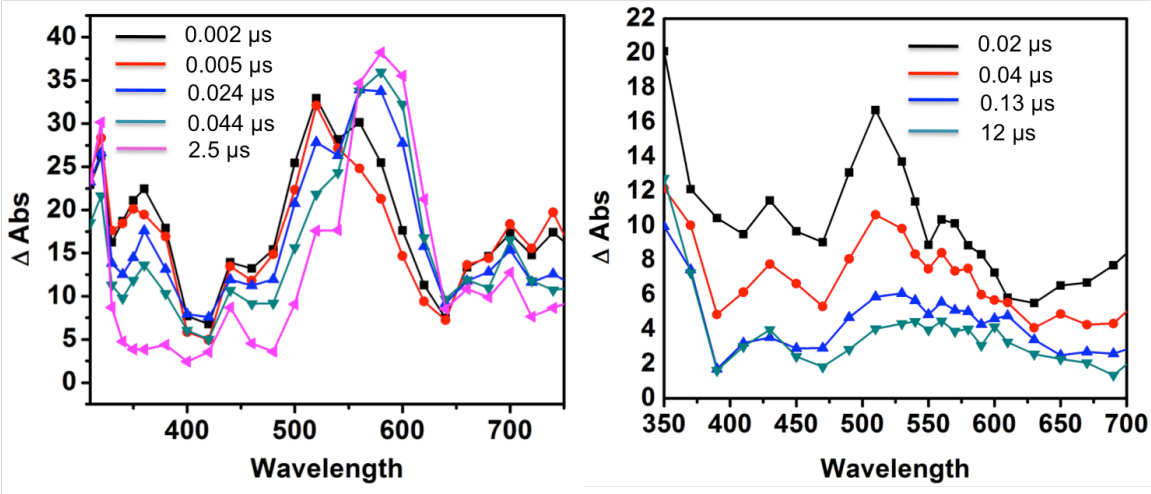

Figure 67: Transient absorption spectra of BRe at the indicated time points. Spectra correspond to acetonitrile (left) and water (right).

We then wanted to examine the interaction between the photosensitizer and the catalyst with and without protein. By altering the kinetic setup to pump the system at 532 nm, only the $Ru(Bpy)_3^{2+}$ will be excited by the laser, therefore any signals seen will be stemming from this initial excitation. With this setup, we monitored the kinetics of two wavelengths; 580 nm corresponding to the Re(0) state and 510 nm corresponding to the reduced photosensitizer. (Figures 69 and 70) Under these conditions, the signal at 580 nm in the absence of catalyst decays with a rate constant of 2.05×10^9 M^{-1} s^{-1}. Upon inclusion of BRe the signal decays significantly faster with a rate constant of 1.85×10^{10} M^{-1} s^{-1}, indicative of a diffusion-controlled process. This is accompanied by an increase in the signal at 510 nm with a matching rate constant, resulting from an electron transfer from the photosensitizer to BRe. When SA-BRe is instead included as catalyst in the

experiment, no significant increase in the decay rate at 580 is seen, along with a lack of increase in signal at 510 nm, indicating the interaction between the photosensitizer and the catalyst is reduced in the presence of the protein.

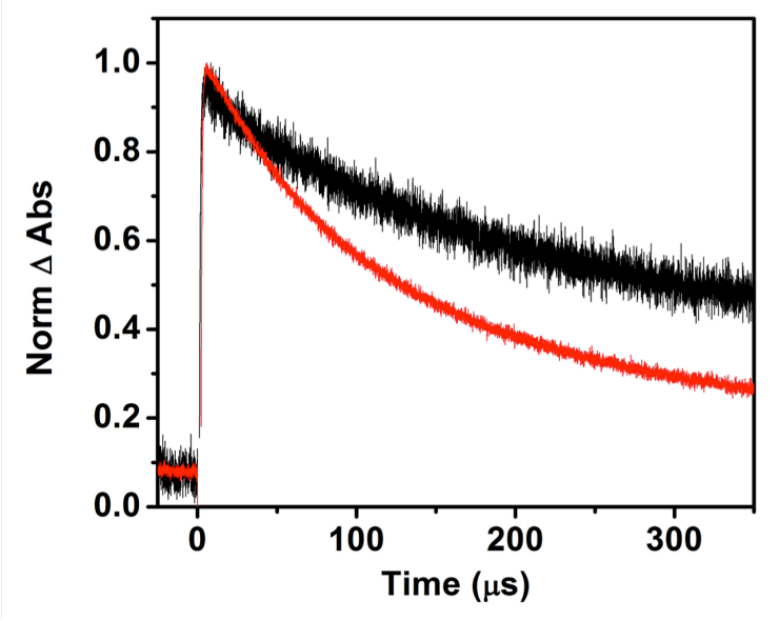

Figure 68: Transient absorption decay kinetics at 580 nm for BRe (red) and SA-BRe (black). Samples were excited at 332 nm.

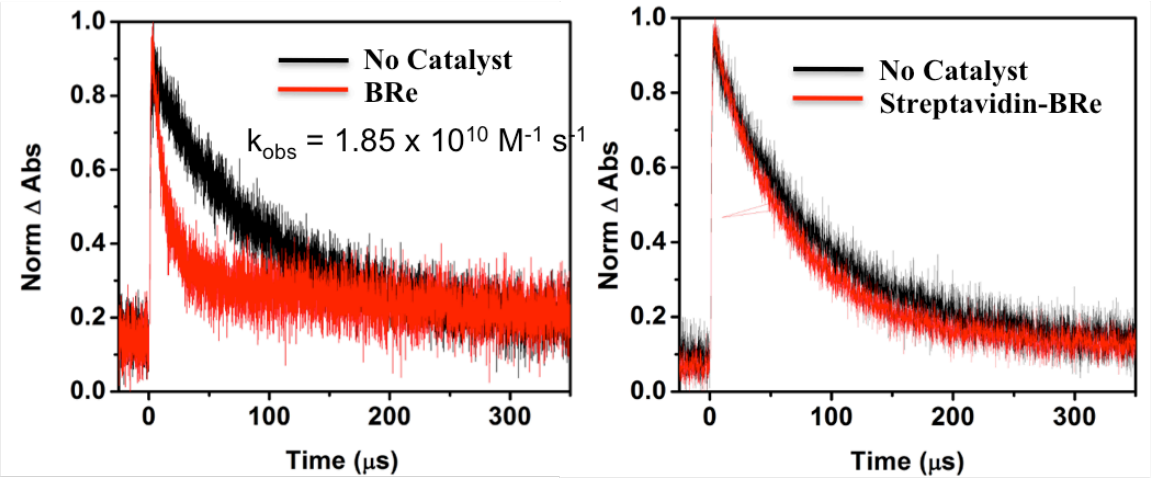

Figure 69: Transient absorption decay kinetics at 510 nm for BRe (left) and SA-BRe (right). Samples were excited at 532 nm, in the absence (black) or presence of catalyst (red).

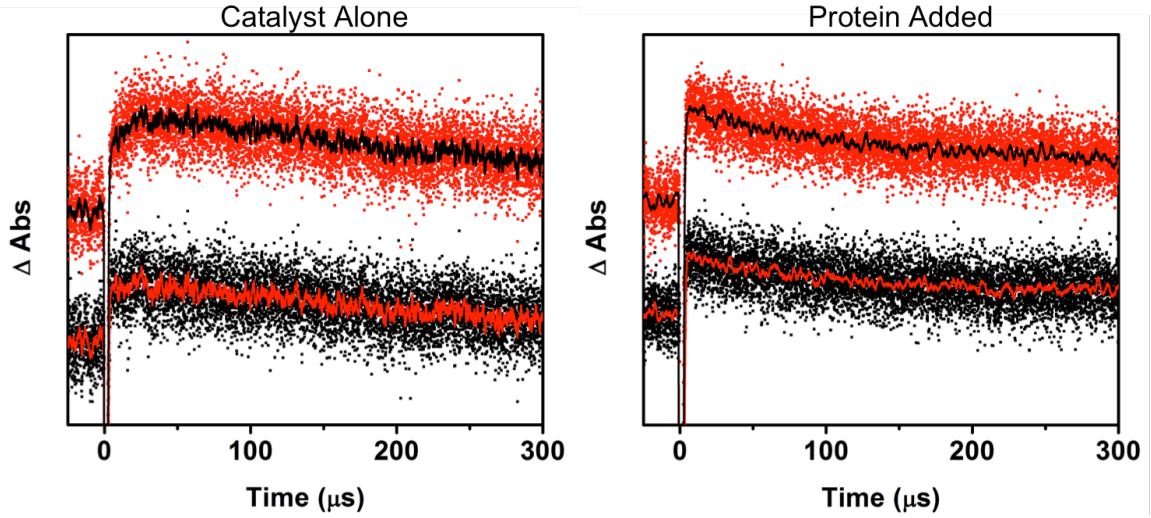

Figure 70: Transient absorption decay kinetics at 510 nm for BRe (left) and SA-BRe (right). Samples were excited at 532 nm, in the absence (black) or presence of catalyst (red).

A previous report of a ruthenium-sensitized Re-diimine system which functioned in water reported only formate production from the system at pH 4, compared to the above characterization at pH 6.[151] Interested by this difference, we characterized the SA-BRe catalyst at varied pH values from 4-6. (Figure 71) At pH 4, our designed metalloenzyme produces exclusively formate, however a very low TON is seen. By increasing the pH to 4.5, above the pK_a of ascorbic acid, the photochemical system functioned more efficiently and led to more turnovers, as well as an increase in the fraction of both H_2 and CO produced. Further increase of the pH to 5 and 6 led to nearly exclusive production of H_2 and CO from the catalyst.

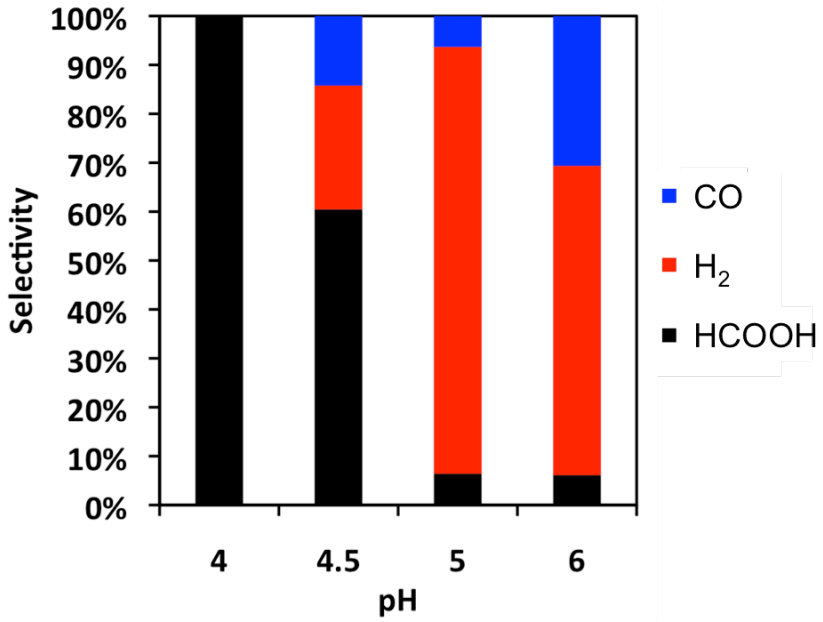

Figure 71: Photoinduced CO_2 reduction catalyzed by SA-BRe, with selectivity reported as % of total turnovers of each catalyst. Conditions: 100 mM ascorbic acid, 1 atm CO_2, 1 mM $Ru(Bpy)_3^{2+}$

The Re-diimine catalysts have been long been implicated for their exclusive production of CO from organic solvents; a large amount of computational work has accompanied this experimental evidence leading to well-accepted mechanisms of action.[168] The selectivity that is seen for these catalysts is attributed to the activation barrier for the protonation of the metal to form a hydride to be too high to facilitate H_2 or formate production. However, solvents can play a major role in stabilizing reactive intermediates, altering the electrostatics of a catalyst and therefore the basicity of the metal. To fully explore the novel reactivity seen when these catalysts are utilized in water, we utilized DFT methodologies to characterize the mechanism of action in water by exploring a model complex.

Starting from the neutral phenanthroline-$Re(CO)_3Cl$, the catalyst was optimized through the reduction cycle down to the twice reduced phenathroline-$Re(CO)_3^{-1}$. Calculated reduction potentials of -1.256 and -1.360 for the first and second reduction are in good agreement with previously determined values for similar catalysts.[168] It is worth noting that in water the driving force for the halide dissociation is significantly greater than what is seen in MeCN, having a driving force 8.3 kcal more. In order to assess the selectivity of the catalyst we then modeled all reasonable catalyst states, starting from the phenathroline-$Re(CO)_3^{-1}$, for all three products measured experimentally (CO, H_2, and Formate) in order to propose product formation-mechanisms in the photosensitizing system (reducing potential of -1.26 V vs SHE). (Figures 72 and 73) Even in the alternative solvent, the CO-forming mechanism is not changed relative to what has been proposed in the past.

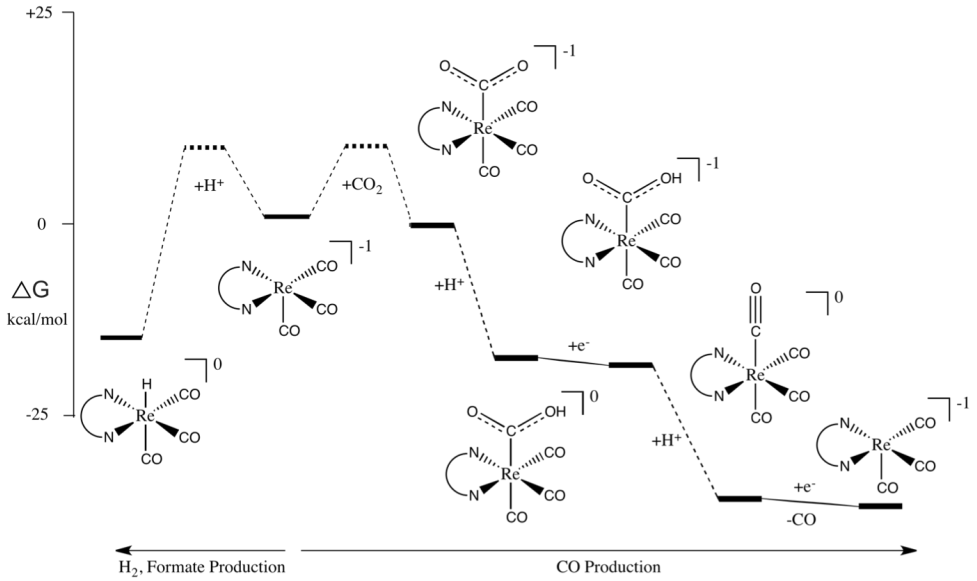

Figure 72: Computationally optimized mechanism for CO_2 reduction in water by the BRe system photosensitized by $Ru(Bpy)_3^2$. Dashed lines correspond steps with transition states.

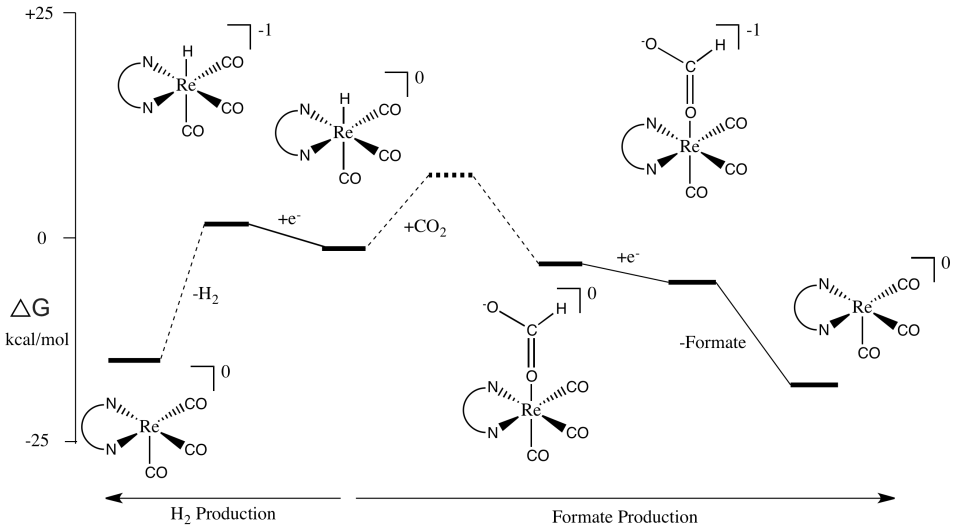

Figure 73: Computationally optimized mechanism for CO_2 reduction in water by the BRe system photosensitized by $Ru(Bpy)_3^2$. Dashed lines correspond steps with transition states.

Due to H_2 and formate not being explored previously, the H_2 and formate production pathways are novel mechanisms of action, both stemming from the hydride formation in Figure 70. By examining the transition states of the key mechanistic step (CO_2 binding or protonation of the metal), insight can be obtained as to why the selectivity towards CO production is lost when functioning in water. In previous work, the barrier of protonation (12.8 kcal) is significantly higher than the barrier of CO_2 binding (3.2 kcal), which is followed by a barrierless protonation step (the first irreversible step). This can be compared to values calculated in water, where protonation by carbonic acid occurs with a barrier of 11.65 kcal/mol and CO_2 binding occurs at a comparable 10.5 kcal/mol, leading to the lack of specificity seen during catalysis. Current work is focusing on identification of alternative transition states relevant to the H_2 and formate production pathways to give further insight into the mechanism of action and as to why the selectivity is altered when the pH is changed.

In conclusion, I presented here the design and characterization of an artificial CO_2-reducing metalloenzyme. Using transient absorption spectroscopy I showed that the catalytically active state is stabilized in the presence of protein, and the interaction with the photosensitizer is actually disfavored by the protein. This implicates redesign of the photocatalytic system as a means to increase the overall yield of CO_2 reduction with the designed enzyme. Further, using computational methods I proposed novel H_2 and formate producing mechanisms from the Re-diimine catalyst, as well as gave insight as to the change in selectivity by isolating

transition states computationally. The designed system is optimal for redesign in order to enhance the protein-effects during catalysis, as well as for optimization via *in vivo* selection methodologies.

CHAPTER 5

CONCLUSIONS AND OUTLOOK

In this thesis, I have presented six different successful attempts to utilize both peptide and protein design to obtain artificial metalloenzymes. The first aspect of my work revolved around the design of electron transfer modules into artificial peptides. With the two constructs that I presented, as well as prior work in my lab in the same field, we are able to show that we have a high level of control over both the cluster type as well as the inter-cluster distance through use of the Domain Swapped Dimer peptide. I was able to show that these peptides are also not isolated to only a single function, which can often be the case with designed peptides, but instead the peptides are able to interact with artificial photosensitizers and natural redox proteins. This work is a major step forward n the design of tailor made redox pathways, as this peptide (or others based off the ubiquitous coiled-coil protein fold) can be incorporated with artificial redox enzymes which carry out reactions in order to shuttle electrons from either dyes or from an electrode surface.

The second aspect of my work, designing two systems as hydrogen producing biohybrids, showed the generality of the methodology proposed here. Using two heme-binding proteins, I was able to show that the protein environment can tune the redox pathways via two separate mechanisms, charge interactions or through direct coordination of the artificial catalyst. As researchers continue to explore the role that proteins play in catalysis, general systems such as the one that I have described here will be immensely useful for mechanistic insight into natural

metalloenzymes. Along with the basic science aspect, the designed systems can be easily interfaced with both material systems and designed electron transfer peptides to generate robust, photoactive materials for fuel generation.

Finally, with the presentation of the work on CO_2 reduction catalysts, I took a step towards an atomic level understanding of how the reactions that we are employing are working in the designed systems, and what about the protein is actually aiding in the overall catalytic cycle. It is mechanistic insight garnered from these types of studies that will allow for the future design of robust, highly active, and cheap catalysts for fuel generation, a major step in solving the renewable fuel demands that society has today.

Moving forward, the designed systems are optimal for future work in two separate aspects. The first is mechanistic understanding of the role proteins play in catalysis. This will be done using the advanced spectroscopic tools that are being developed, such as time resolved systems or advanced electrochemical characterization techniques. Specifically, the proteins described here pair well with the XANES and EXAFS techniques, using x-rays to probe the local electronic environment around catalysts to gain insight as to why they function better or worse.

Ultimately, the systems are optimal for interfacing with materials. With novel materials for light absorption, with large pore size, alternative charges or functionalities on the surfaces, and stability, it is only time before the best materials for interfacing proteins are found. With these in hand, catalytic systems can be

designed and deployed into the consumer world, aiding in solving the energetic problems we are facing now and will face in the future.

REFERENCES

[1] Dresselhaus, M. S., and Thomas, I. L. (2001) Alternative energy technologies, *Nature 414*, 332-337.

[2] Nejat, P., Jomehzadeh, F., Taheri, M. M., Gohari, M., and Abd Majid, M. Z. (2015) A global review of energy consumption, CO2 emissions and policy in the residential sector (with an overview of the top ten CO2 emitting countries), *Ren. Sus. Ener. Rev. 43*, 843-862.

[3] Gust, D., Moore, T. A., and Moore, A. L. (2012) Realizing artificial photosynthesis, *Faraday Discuss. 155*, 9-26.

[4] Ort, D. R., Merchant, S. S., Alric, J., Barkan, A., Blankenship, R. E., Bock, R., Croce, R., Hanson, M. R., Hibberd, J. M., Long, S. P., Moore, T. A., Moroney, J., Niyogi, K. K., Parry, M. A. J., Peralta-Yahya, P. P., Prince, R. C., Redding, K. E., Spalding, M. H., van Wijk, K. J., Vermaas, W. F. J., von Caemmerer, S., Weber, A. P. M., Yeates, T. O., Yuan, J. S., and Zhu, X. G. (2015) Redesigning photosynthesis to sustainably meet global food and bioenergy demand, *Proc. Natl. Acad. Sci. U. S. A. 112*, 8529-8536.

[5] Liu, J., Chakraborty, S., Hosseinzadeh, P., Yu, Y., Tian, S., Petrik, I., Bhagi, A., and Lu, Y. (2014) Metalloproteins containing cytochrome, iron-sulfur, or copper redox centers, *Chem. Rev. 114*, 4366-4469.

[6] Lubitz, W., Ogata, H., Rudiger, O., and Reijerse, E. (2014) Hydrogenases, *Chem. Rev. 114*, 4081-4148.

[7] Friedle, S., Reisner, E., and Lippard, S. J. (2010) Current challenges of modeling diiron enzyme active sites for dioxygen activation by biomimetic synthetic complexes, *Chem. Soc. Rev. 39*, 2768-2779.

[8] Knorzer, P., Silakov, A., Foster, C. E., Armstrong, F. A., Lubitz, W., and Happe, T. (2012) Importance of the protein framework for catalytic activity of [FeFe]-Hydrogenases, *J. Biol. Chem. 287*, 1489-1499.

[9] Fontecave, M. (2006) Iron-sulfur clusters: ever-expanding roles, *Nat. Chem. Biol. 2*, 171-174.

[10] Beinert, H., Holm, R. H., and Munck, E. (1997) Iron-sulfur clusters: nature's modular, multipurpose structures, *Science 277*, 653-659.

[11] Klausner, R. D., and Rouault, T. A. (1993) A double life: cytosolic aconitase as a regulatory RNA binding protein, *Mol. Biol. Cell 4*, 1-5.

[12] Koay, M. S., Antonkine, M. L., Gärtner, W., and Lubitz, W. (2008) Modelling low-potential [Fe4S4] clusters in proteins., *Chem. Biodiv. 5*, 1571-1587.

[13] Klingen, A. R., and Ullmann, G. M. (2004) Negatively charged residues and hydrogen bonds tune the ligand histidine pKa values of Rieske iron-sulfur proteins, *Biochemistry 43*, 12383-12389.

[14] Brereton, P. S., Verhagen, M. F. J. M., Zhou, Z. H., and Adams, M. W. W. (1998) Effect of iron-sulfur cluster enviornment in modulating the thermodynamic properties and biological function of ferredoxin from *Pyrococcus furiosus*, *Biochemistry 37*, 7351-7362.

[15] Hoppe, A., Pandelia, M.-E., Gärtner, W., and Lubitz, W. (2011) [Fe3S4]- and [Fe3S4]-cluster formation in synthetic peptides., *Biochim. Biophys. Acta 1807*, 1414-1422.

[16] Beck, B. W., Xie, Q., and Ichiye, T. (2001) Sequence determination of reduction potentials by cysteinyl hydrogen bonds and peptide pipoles in [4Fe-4S] ferredoxins, *Biophys J 81*, 601-613.

[17] Kolling, D. J., Brunzelle, J. S., Lhee, S., Crofts, A. R., and Nair, S. K. (2007) Atomic resolution structures of rieske iron-sulfur protein: role of hydrogen bonds in tuning the redox potential of iron-sulfur clusters, *Structure 15*, 29-38.

[18] Backes, G., Mino, Y., Loehr, T. M., Meyer, T. E., Cusanovich, M. A., Sweeney, W. V., Adman, E. T., and Sandersloehr, J. (1991) The environment of Fe4s4 clusters in ferredoxins and high-potential Iron proteins - New information from X-ray crystallography and resonance raman-spectroscopy, *J. Am. Chem. Soc. 113*, 2055-2064.

[19] Coldren, C. D., Hellinga, H. W., and Caradonna, J. P. (1997) The rational design and construction of a cuboidal iron-sulfur protein, *Proc. Natl. Acad. Sci. U. S. A. 94*, 6635-6640.

[20] Mulholland, S. E., Gibney, B. R., Rabanal, F., and Dutton, P. L. (1998) Characterization of the fundamental protein ligand requirements of [4Fe-4S](2+/+) clusters with sixteen amino acid maquettes, *J. Am. Chem. Soc. 120*, 10296-10302.

[21] Mulholland, S. E., Gibney, B. R., Rabanal, F., and Dutton, P. L. (1999) Determination of nonligand amino acids critical to [4Fe-4S]2+/+ assembly in ferredoxin maquettes, *Biochemistry 38*, 10442-10448.

[22] Gibney, B. R., Mulholland, S. E., Rabanal, F., and Dutton, P. L. (1996) Ferredoxin and ferredoxin-heme maquettes, *Proc. Natl. Acad. Sci. U. S. A. 93*, 15041-15046.

[23] Laplaza, C. E., and Holm, R. H. (2001) Helix-loop-helix peptides as scaffolds for the construction of bridged metal assemblies in proteins: The spectroscopic A-cluster structure in carbon monoxide dehydrogenase, *J. Am. Chem. Soc. 123*, 10255-10264.

[24] Scott, M. P., and Biggins, J. (1997) Introduction of a [4Fe-4S (S-cys)4]+1,+2 iron-sulfur center into a four-α helix protein using design parameters from the domain of the Fx cluster in the photosystem I reaction center, *Protein Sci. 6*, 340-346.

[25] Antonkine, M. L., and Golbeck, J. H. (2006) Molecular interactions of the stromal subunit PsaC with the PsaA/PsaB heterodimer, *Adv. Photosynth. Respir. 24*, 79-98.

[26] Antonkine, M. L., Koay, M. S., Epel, B., Breitenstein, C., Gopta, O., Gaertner, W., Bill, E., and Lubitz, W. (2009) Synthesis and characterization of de novo designed peptides modelling the binding sites of [4Fe-4S] clusters in photosystem I, *Biochim. Biophys. Acta, Bioenerg. 1787*, 995-1008.

[27] Grzyb, J., Xu, F., Nanda, V., Luczkowska, R., Reijerse, E., Lubitz, W., and Noy, D. (2012) Empirical and computational design of iron-sulfur cluster proteins, *Biochim. Biophys. Acta 1817*, 1256-1262.

[28] Grzyb, J., Xu, F., Weiner, L., Reijerse, E. J., Lubitz, W., Nanda, V., and Noy, D. (2010) De novo design of a non-natural fold for an iron-sulfur protein: alpha-helical coiled-coil with a four-iron four-sulfur cluster binding site in its central core, *Biochim. Biophys. Acta 1797*, 406-413.

[29] Fritsch, J., Scheerer, P., Frielingsdorf, S., Kroschinsky, S., Friedrich, B., Lenz, O., and Spahn, C. M. (2011) The crystal structure of an oxygen-tolerant hydrogenase uncovers a novel iron-sulphur centre, *Nature 479*, 249-252.

[30] Shomura, Y., Yoon, K. S., Nishihara, H., and Higuchi, Y. (2011) Structural basis for a [4Fe-3S] cluster in the oxygen-tolerant membrane-bound [NiFe]-hydrogenase, *Nature 479*, 253-256.

[31] Grubel, K., and Holland, P. L. (2012) New iron-sulfur clusters help hydrogenases tolerate oxygen, *Angew. Chem. Int. Ed. 51*, 3308-3310.

[32] Bentrop, D., Capozzi, F., and Luchinat, C. (2001) Iron-sulfur proteins, *Handbook on Metalloproteins*, 359-447.

[33] Roy, A., Sarrou, I., Vaughn, M. D., Astashkin, A. V., and Ghirlanda, G. (2013) De novo design of an artificial bis[4Fe-4S] binding protein, *Biochemistry 52*, 7586-7594.

[34] Ogihara, N. L., Ghirlanda, G., Bryson, J. W., Gingery, M., DeGrado, W. F., and Eisenberg, D. (2001) Design of three-dimensional domain-swapped dimers and fibrous oligomers, *Proc. Natl. Acad. Sci. U. S. A. 98*, 1404-1409.

[35] Carter, P. (1971) Spectrophotometric determination of serum iron at the submicrogram level with a new reagent (ferrozine), *Anal. Biochem. 40*, 450-458.

[36] Mathews, R., Charlton, S., Sands, R. H., and Palmer, G. (1974) On the nature of the spin coupling between the iron-sulfur clusters in the eight-iron ferredoxins, *J. Biol. Chem. 249*, 4326-4328.

[37] Sherman, B. D., Pillai, S., Kodis, G., Bergkamp, J., Mallouk, T. E., Gust, D., Moore, T. A., and Moore, A. L. (2011) A porphyrin-stabilized iridium oxide water oxidation catalyst, *Can. J. Chem. 89*, 152-157.

[38] Loewe, R. S., Ambroise, A., Muthukumaran, K., Padmaja, K., Lysenko, A. B., Mathur, G., Li, Q., Bocian, D. F., Misra, V., and Lindsey, J. S. (2004) Porphyrins bearing mono or tripodal benzylphosphonic acid tethers for attachment to oxide surfaces, *J. Org. Chem. 69*, 1453-1460.

[39] Guldi, D. M., Zilbermann, I., Anderson, G., Li, A., Balbinot, D., Jux, N., Hatzimarinaki, M., Hirsch, A., and Prato, M. (2004) Multicomponent redox gradients on photoactive electrode surfaces, *Chem. Commun.*, 726-727.

[40] Roy, A., Sommer, D. J., Schmitz, R. A., Brown, C. L., Gust, D., Astashkin, A., and Ghirlanda, G. (2014) A de novo designed 2[4Fe-4S] ferredoxin mimic mediates electron transfer, *J. Am. Chem. Soc. 136*, 17343-17349.

[41] Han, G. W., Yang, X. L., McMullan, D., Chong, Y. E., Krishna, S. S., Rife, C. L., Weekes, D., Brittain, S. M., Abdubek, P., Ambing, E., Astakhova, T., Axelrod, H. L., Carlton, D., Caruthers, J., Chiu, H. J., Clayton, T., Duan, L., Feuerhelm, J., Grant, J. C., Grzechnik, S. K., Jaroszewski, L., Jin, K. K., Klock, H. E., Knuth, M. W., Kumar, A., Marciano, D., Miller, M. D., Morse, A. T., Nigoghossian, E., Okach, L., Paulsen, J., Reyes, R., van den Bedem, H., White, A., Wolf, G., Xu, Q., Hodgson, K. O., Wooley, J., Deacon, A. M., Godzik, A., Lesley, S. A., Elsliger, M. A., Schimmel, P., and Wilson, I. A. (2010) Structure of a tryptophanyl-tRNA synthetase containing an iron-sulfur cluster, *Acta Cryst. F 66*, 1326-1334.

[42] Rothery, R. A., and Weiner, J. H. (1991) Alteration of the iron-sulfur cluster composition of *Escherichia coli* dimethyl sulfoxide reductase by site-directed mutagenesis, *Biochemistry 30*, 8296-8305.

[43] Durrant, J. D., de Oliveira, C. A. F., and McCammon, J. A. (2011) POVME: An algorithm for measuring binding-pocket volumes, *J. Mol. Graphics Modell. 29*, 773-776.

[44] Meyer, J. (2008) Iron-sulfur protein folds, iron-sulfur chemistry, and evolution., *J. Biol. Inorg. Chem. 13*, 157-170.

[45] Antonkine, M., Breitenstein, C., Epel, B., Bill, E., Gartner, W., and Lubitz, W. (2007) De Novo peptides modelling the binding sites of [4Fe-4S] clusters in photosystem I, *Photosynth. Res. 91*, 282-282.

[46] Fontecilla-Camps, J. C., Volbeda, A., Cavazza, C., and Nicolet, Y. (2007) Structure/function relationships of [NiFe]- and [FeFe]-hydrogenases, *Chem. Rev. 107*, 4273-4303.

[47] Johnson, D. C., Dean, D. R., Smith, A. D., and Johnson, M. K. (2005) Structure, function, and formation of biological iron-sulfur clusters, *Annu. Rev. Biochem. 74*, 247-281.

[48] Lill, R. (2009) Function and biogenesis of iron-sulfur proteins, *Nature 460*, 831-838.

[49] Dubini, A., Mus, F., Seibert, M., Grossman, A. R., and Posewitz, M. C. (2009) Flexibility in anaerobic metabolism as revealed in a mutant of Chlamydomonas reinhardtii lacking hydrogenase activity, *J. Biol. Chem. 284*, 7201-7213.

[50] Jin, Z., Heinnickel, M., Krebs, C., Shen, G., Golbeck, J. H., and Bryant, D. A. (2008) Biogenesis of iron-sulfur clusters in Photosystem I: holo-NfuA from the cyanobacterium Synechococcus sp. PCC 7002 rapidly and efficiently transfers [4Fe-4S] clusters to APO-PsaC in vitro, *J. Biol. Chem. 283*, 28426-28435.

[51] Jordan, P., Fromme, P., Witt, H. T., Klukas, O., Saenger, W., and Krauss, N. (2001) Three-dimensional structure of cyanobacterial photosystem I at 2.5 A resolution, *Nature 411*, 909-917.

[52] Mulder, D. W., Shepard, E. M., Meuser, J. E., Joshi, N., King, P. W., Posewitz, M. C., Broderick, J. B., and Peters, J. W. (2011) Insights into [FeFe]-hydrogenase structure, mechanism, and maturation, *Structure 19*, 1038-1052.

[53] Peters, J. W., Lanzilotta, W. N., Lemon, B. J., and Seefeldt, L. C. (1998) X-ray crystal structure of the Fe-only hydrogenase (CpI) from Clostridium pasteurianum to 1.8 angstrom resolution, *Science 282*, 1853-1858.

[54] Sweeney, W. V., and Rabinowitz, J. C. (1980) Proteins containing 4Fe-4S clusters: an overview, *Annu. Rev. Biochem. 49*, 139-161.

[55] Vignais, P. M., Billoud, B., and Meyer, J. (2001) Classification and phylogeny of hydrogenases, *FEMS Microbiol. Rev. 25*, 455-501.

[56] Kennedy, M. L., and Gibney, B. R. (2002) Proton coupling to [4Fe-4S]2+/+ and [4Fe-4Se]2+/+ oxidation and reduction in a designed protein, *J. Am. Chem. Soc. 124*, 6826-6827.

[57] Mathews, R., Charlton, S., Sands, R. H., and Palmer, G. (1974) Nature of the spin coupling between the iron-sulfur clusters in the eight-iron ferredoxins, *J. Biol. Chem. 249*, 4326-4328.

[58] Torres, R. A., Lovell, T., Noodleman, L., and Case, D. A. (2003) Density functional and reduction potential calculations of Fe4S4 clusters, *J. Am. Chem. Soc. 125*, 1923-1936.

[59] Smith, E. T., and Feinberg, B. A. (1990) Redox properties of several bacterial ferredoxins using square wave voltammetry, *J. Biol. Chem. 265*, 14371-14376.

[60] Eisenstein, K. K., and Wang, J. H. (1969) Conversion of light to chemical free energy. I. Porphyrin-sensitized photoreduction of ferredoxin by glutathione, *J. Biol. Chem. 244*, 1720-1728.

[61] Kyritsis, P., Hatzfeld, O. M., Link, T. A., and Moulis, J.-M. (1998) The two [4Fe-4S] clusters in Chromatium vinosum ferredoxin have largely different reduction potentials. Structural origin and functional consequences, *J. Biol. Chem. 273*, 15404-15411.

[62] Kathan-Galipeau, K., Nanayakkara, S., O'Brian, P. A., Nikiforov, M., Discher, B. M., and Bonnell, D. A. (2011) Direct probe of molecular polarization in de novo protein-electrode interfaces, *ACS Nano 5*, 4835-4842.

[63] Lichtenstein, B. R., Farid, T. A., Kodali, G., Solomon, L. A., Anderson, J. L. R., Sheehan, M. M., Ennist, N. M., Fry, B. A., Chobot, S. E., Bialas, C., Mancini, J. A., Armstrong, C. T., Zhao, Z., Esipova, T. V., Snell, D., Vinogradov, S. A., Discher, B. M., Moser, C. C., and Dutton, P. L. (2012) Engineering oxidoreductases: maquette proteins designed from scratch, *Biochem. Soc. Trans. 40*, 561-566.

[64] McAllister, K. A., Zou, H., Cochran, F. V., Bender, G. M., Senes, A., Fry, H. C., Nanda, V., Keenan, P. A., Lear, J. D., Saven, J. G., Therien, M. J., Blasie, J. K., and DeGrado, W. F. (2008) Using α-helical coiled-coils to design nanostructured metalloporphyrin arrays, *J. Am. Chem. Soc. 130*, 11921-11927.

[65] Strzalka, J., Xu, T., Tronin, A., Wu, S. P., Miloradovic, I., Kuzmenko, I., Gog, T., Therien, M. J., and Blasie, J. K. (2006) Structural studies of amphiphilic 4-helix bundle peptides incorporating designed extended chromophores for nonlinear optical biomolecular materials, *Nano Lett. 6*, 2395-2405.

[66] Topoglidis, E., Discher, B. M., Moser, C. C., Dutton, P. L., and Durrant, J. R. (2003) Functionalizing nanocrystalline metal oxide electrodes with robust synthetic redox proteins, *ChemBioChem 4*, 1332-1339.

[67] Harriman, A. (1980) Luminescence of porphyrins and metalloporphyrins. Part 1. Zinc(II), nickel(II) and manganese(II) porphyrins, *J. Chem. Soc., Faraday Trans. 1 76*, 1978-1985.

[68] Zastrow, M. L., Peacock, A. F. A., Stuckey, J. A., and Pecoraro, V. L. (2012) Hydrolytic catalysis and structural stabilization in a designed metalloprotein, *Nat. Chem. 4*, 118-123.

[69] Zastrow, M. L., and Pecoraro, V. L. (2013) Influence of active site location on catalytic activity in de novo-designed zinc metalloenzymes, *J. Am. Chem. Soc. 135*, 5895-5903.

[70] Berwick, M. R., Lewis, D. J., Jones, A. W., Parslow, R. A., Dafforn, T. R., Cooper, H. J., Wilkie, J., Pikramenou, Z., Britton, M. M., and Peacock, A. F. A. (2014) De novo design of Ln(III) coiled coils for imaging applications, *J. Am. Chem. Soc. 136*, 1166-1169.

[71] Boyle, A. L., and Woolfson, D. N. (2011) De novo designed peptides for biological applications, *Chem. Soc. Rev. 40*, 4295-4306.

[72] Brodin, J. D., Ambroggio, X. I., Tang, C., Parent, K. N., Baker, T. S., and Tezcan, F. A. (2012) Metal-directed, chemically tunable assembly of one-, two- and three-dimensional crystalline protein arrays, *Nat. Chem. 4*, 375-382.

[73] Brodin, J. D., Carr, J. R., Sontz, P. A., and Tezcan, F. A. (2014) Exceptionally stable, redox-active supramolecular protein assemblies with emergent properties, *Proc. Natl. Acad. Sci. U. S. A. 111*, 2897-2902.

[74] Dutton, P. L., and Moser, C. C. (2011) Engineering enzymes, *Faraday Discuss. 148*, 443-448.

[75] Ghirlanda, G., Lear, J. D., Ogihara, N. L., Eisenberg, D., and DeGrado, W. F. (2002) A hierarchic approach to the design of hexameric helical barrels, *J. Mol. Biol. 319*, 243-253.

[76] Huard, D. J. E., Kane, K. M., and Tezcan, F. A. (2013) Re-engineering protein interfaces yields copper-inducible ferritin cage assembly, *Nat. Chem. Biol. 9*, 169-176.

[77] King, N. P., Bale, J. B., Sheffler, W., McNamara, D. E., Gonen, S., Gonen, T., Yeates, T. O., and Baker, D. (2014) Accurate design of co-assembling multi-component protein nanomaterials, *Nature 510*, 103-108.

[78] Mills, J. H., Khare, S. D., Bolduc, J. M., Forouhar, F., Mulligan, V. K., Lew, S., Seetharaman, J., Tong, L., Stoddard, B. L., and Baker, D. (2013) Computational design of an unnatural amino acid dependent metalloprotein with atomic level accuracy, *J. Am. Chem. Soc. 135*, 13393-13399.

[79] Tinberg, C. E., Khare, S. D., Dou, J., Doyle, L., Nelson, J. W., Schena, A., Jankowski, W., Kalodimos, C. G., Johnsson, K., Stoddard, B. L., and Baker, D. (2013) Computational design of ligand-binding proteins with high affinity and selectivity, *Nature 501*, 212-216.

[80] Bockris, J. O. (1972) A hydrogen economy, *Science 176*, 1323.

[81] Lewis, N. S., and Nocera, D. G. (2006) Powering the planet: chemical challenges in solar energy utilization, *Proc. Natl. Acad. Sci. U. S. A. 103*, 15729-15735.

[82] Faiella, M., Roy, A., Sommer, D., and Ghirlanda, G. (2013) De novo design of functional proteins: Toward artificial hydrogenases, *Biopolymers 100*, 558-571.

[83] Armstrong, F. A., and Hirst, J. (2011) Reversibility and efficiency in electrocatalytic energy conversion and lessons from enzymes, *Proc. Natl. Acad. Sci. U. S. A. 108*, 14049-14054.

[84] Madden, C., Vaughn, M. D., Diez-Perez, I., Brown, K. A., King, P. W., Gust, D., Moore, A. L., and Moore, T. A. (2012) Catalytic turnover of [FeFe]-hydrogenase based on single-molecule imaging, *J. Am. Chem. Soc. 134*, 1577-1582.

[85] Armstrong, F. A., and Fontecilla-Camps, J. C. (2008) Biochemistry. A natural choice for activating hydrogen, *Science 321*, 498-499.

[86] Camara, J. M., and Rauchfuss, T. B. (2012) Combining acid-base, redox and substrate binding functionalities to give a complete model for the [FeFe]-hydrogenase, *Nat. Chem. 4*, 26-30.

[87] Darensbourg, M. Y., Lyon, E. J., Zhao, X., and Georgakaki, I. P. (2003) The organometallic active site of [Fe]hydrogenase: models and entatic states, *Proc. Natl. Acad. Sci. U. S. A. 100*, 3683-3688.

[88] Helm, M. L., Stewart, M. P., Bullock, R. M., DuBois, M. R., and DuBois, D. L. (2011) A synthetic nickel electrocatalyst with a turnover frequency above 100,000 s(-)(1) for H(2) production, *Science 333*, 863-866.

[89] Tard, C., and Pickett, C. J. (2009) Structural and functional analogues of the active sites of the [Fe]-, [NiFe]-, and [FeFe]-hydrogenases, *Chem. Rev. 109*, 2245-2274.

[90] Huang, J., Mulfort, K. L., Du, P. W., and Chen, L. X. (2012) Photodriven charge separation dynamics in CdSe/ZnS core/shell quantum dot/Cobaloxime hybrid for efficient hydrogen production, *J. Am. Chem. Soc. 134*, 16472-16475.

[91] Jian, J. X., Liu, Q., Li, Z. J., Wang, F., Li, X. B., Li, C. B., Liu, B., Meng, Q. Y., Chen, B., Feng, K., Tung, C. H., and Wu, L. Z. (2013) Chitosan confinement enhances hydrogen photogeneration from a mimic of the diiron subsite of [FeFe]-hydrogenase, *Nat. Comm. 4*.

[92] Krawicz, A., Yang, J. H., Anzenberg, E., Yano, J., Sharp, I. D., and Moore, G. F. (2013) Photofunctional construct that interfaces molecular cobalt-based catalysts for H2 Production to a visible-light-absorbing semiconductor, *J. Am. Chem. Soc. 135*, 11861-11868.

[93] Lense, S., Dutta, A., Roberts, J. A. S., and Shaw, W. J. (2014) A proton channel allows a hydrogen oxidation catalyst to operate at a moderate overpotential with water acting as a base, *Chem. Commun. 50*, 792-795.

[94] Reback, M. L., Buchko, G. W., Kier, B. L., Ginovska-Pangovska, B., Xiong, Y. J., Lense, S., Hou, J. B., Roberts, J. A. S., Sorensen, C. M., Raugei, S., Squier, T. C., and Shaw, W. J. (2014) Enzyme design from the bottom up: An active nickel electrocatalyst with a structured peptide outer coordination sphere, *Chem. Eur. J. 20*, 1510-1514.

[95] Wang, F., Wang, W. G., Wang, X. J., Wang, H. Y., Tung, C. H., and Wu, L. Z. (2011) A highly efficient photocatalytic system for hydrogen production by a robust hydrogenase mimic in an aqueous solution, *Angew. Chem. Int. Ed. 50*, 3193-3197.

[96] Dutta, A., DuBois, D. L., Roberts, J. A., and Shaw, W. J. (2014) Amino acid modified Ni catalyst exhibits reversible H2 oxidation/production over a broad pH range at elevated temperatures, *Proc. Natl. Acad. Sci. U. S. A. 111*, 16286-16291.

[97] Roy, A., Madden, C., and Ghirlanda, G. (2012) Photo-induced hydrogen production in a helical peptide incorporating a [FeFe] hydrogenase active site mimic, *Chem. Commun. 48*, 9816-9818.

[98] Sano, Y., Onoda, A., and Hayashi, T. (2011) A hydrogenase model system based on the sequence of cytochrome c: photochemical hydrogen evolution in aqueous media, *Chem. Commun. 47*, 8229-8231.

[99] Artero, V., Chavarot-Kerlidou, M., and Fontecave, M. (2011) Splitting water with cobalt, *Angew. Chem. Int. Ed. 50*, 7238-7266.

[100] Kaeffer, N., Chavarot-Kerlidou, M., and Artero, V. (2015) Hydrogen evolution catalyzed by cobalt diimine-dioxime complexes, *Acc. Chem. Res. 48*, 1286-1295.

[101] Lakadamyali, F., Kato, M., Muresan, N. M., and Reisner, E. (2012) Selective reduction of aqueous protons to hydrogen with a synthetic cobaloxime catalyst in the presence of atmospheric oxygen, *Angew. Chem. Int. Ed. 51*, 9381-9384.

[102] Wakerley, D. W., Gross, M. A., and Reisner, E. (2014) Proton reduction by molecular catalysts in water under demanding atmospheres, *Chem. Commun. 50*, 15995-15998.

[103] Kellett, R. M., and Spiro, T. G. (1985) Cobalt porphyrin electrode films as H2 evolution catalysts, *Inorg. Chem. 24*, 2378-2382.

[104] Lee, C. H., Dogutan, D. K., and Nocera, D. G. (2011) Hydrogen generation by hangman metalloporphyrins, *J. Am. Chem. Soc. 133*, 8775-8777.

[105] Manbeck, G. F., and Fujita, E. (2015) A review of iron and cobalt porphyrins, phthalocyanines and related complexes for electrochemical and photochemical reduction of carbon dioxide, *J. Porphyrins Phthalocyanines 19*, 45-64.

[106] Natali, M., Luisa, A., Iengo, E., and Scandola, F. (2014) Efficient photocatalytic hydrogen generation from water by a cationic cobalt(II) porphyrin, *Chem. Commun. 50*, 1842-1844.

[107] Kleingardner, J. G., Kandemir, B., and Bren, K. L. (2014) Hydrogen evolution from neutral water under aerobic conditions catalyzed by cobalt microperoxidase-11, *J. Am. Chem. Soc. 136*, 4-7.

[108] Sommer, D. J., Vaughn, M. D., and Ghirlanda, G. (2014) Protein secondary-shell interactions enhance the photoinduced hydrogen production of cobalt protoporphyrin IX, *Chem. Commun. 50*, 15825–16001.

[109] Gibson, D. G., Smith, H. O., Hutchison, C. A., 3rd, Venter, J. C., and Merryman, C. (2010) Chemical synthesis of the mouse mitochondrial genome, *Nat. Methods 7*, 901-903.

[110] Harrison, S. C., and Blout, E. R. (1965) Reversible conformational changes of myoglobin and apomyoglobin, *J. Biol. Chem. 240*, 299-&.

[111] Li, C. Z., Nishiyama, K., and Taniguchi, I. (2000) Electrochemical and spectroelectrochemical studies on cobalt myoglobin, *Electrochim. Acta 45*, 2883-2888.

[112] Fourmond, V., Hoke, K., Heering, H. A., Baffert, C., Leroux, F., Bertrand, P., and Leger, C. (2009) SOAS: A free program to analyze electrochemical data and other one-dimensional signals, *Bioelectrochemistry 76*, 141-147.

[113] Iwuchukwu, I. J., Vaughn, M., Myers, N., O'Neill, H., Frymier, P., and Bruce, B. D. (2010) Self-organized photosynthetic nanoparticle for cell-free hydrogen production, *Nat. Nanotechnol. 5*, 73-79.

[114] Millsaps, J. F., Bruce, B. D., Lee, J. W., and Greenbaum, E. (2001) Nanoscale photosynthesis: photocatalytic production of hydrogen by platinized photosystem I reaction centers, *Photochem. Photobiol. 73*, 630-635.

[115] Lu, Y., Yeung, N., Sieracki, N., and Marshall, N. M. (2009) Design of functional metalloproteins, *Nature 460*, 855-862.

[116] Brucker, E. A., Olson, J. S., Phillips, G. N., Dou, Y., and Ikeda-Saito, M. (1996) High resolution crystal structures of the deoxy, oxy, and aquomet forms of cobalt myoglobin, *J. Biol. Chem. 271*, 25419-25422.

[117] Ueno, T., Koshiyama, T., Ohashi, M., Kondo, K., Kono, M., Suzuki, A., Yamane, T., and Watanabe, Y. (2005) Coordinated design of cofactor and active site structures in development of new protein catalysts, *J. Am. Chem. Soc. 127*, 6556-6562.

[118] Ueno, T., Yokoi, N., Abe, S., and Watanabe, Y. (2007) Crystal structure based design of functional metal/protein hybrids, *J. Inorg. Biochem. 101*, 1667-1675.

[119] Mathura, S., Sannasy, D., de Sousa, A. S., Perry, C. B., Navizet, I., and Marques, H. M. (2013) The preparation of N-acetyl-Co(III)-microperoxidase-8 (NAcCoMP8) and its ligand substitution reactions: A comparison with aquacobalamin (vitamin B-12a), *J. Inorg. Biochem. 123*, 66-79.

[120] Muckerman, J. T., and Fujita, E. (2011) Theoretical studies of the mechanism of catalytic hydrogen production by a cobaloxime, *Chem. Commun. 47*, 12456-12458.

[121] Wang, W. H., Lu, J. X., Yao, P., Xie, Y., and Huang, Z. X. (2003) The distinct heme coordination environments and heme-binding stabilities of His39Ser and His39Cys mutants of cytochrome b5, *Protein Eng. 16*, 1047-1054.

[122] Bashford, D., Case, D. A., Dalvit, C., Tennant, L., and Wright, P. E. (1993) Electrostatic calculations of side-chain pk(a) values in myoglobin and comparison with NMR data for histidines, *Biochemistry 32*, 8045-8056.

[123] Dempsey, J. L., Brunschwig, B. S., Winkler, J. R., and Gray, H. B. (2009) Hydrogen evolution catalyzed by cobaloximes, *Acc. Chem. Res. 42*, 1995-2004.

[124] Hargrove, M. S., and Olson, J. S. (1996) The stability of holomyoglobin is determined by heme affinity, *Biochemistry 35*, 11310-11318.

[125] Faraone-Mennella, J., Tezcan, F. A., Gray, H. B., and Winkler, J. R. (2006) Stability and folding kinetics of structurally characterized cytochrome c-b562, *Biochemistry 45*, 10504-10511.

[126] Itagaki, E., and Hager, L. P. (1966) Studies on cytochrome B562 of Escherichia Coli .I. Purification and crystallization of cytochrome B562, *J. Biol. Chem. 241*, 3687-&.

[127] Itagaki, E., Palmer, G., and Hager, L. P. (1967) Studies on cytochrome B562 of Escherichia Coli .2. Reconstitution of cytochrome B562 from apoprotein and hemin, *J. Biol. Chem. 242*, 2272-&.

[128] Lederer, F., Glatigny, A., Bethge, P. H., Bellamy, H. D., and Mathews, F. S. (1981) Improvement of the 2.5 a resolution model of cytochrome-B562 by redetermining the primary structure and using molecular graphics, *J. Mol. Biol. 148*, 427-448.

[129] Bersch, B., Blackledge, M. J., Meyer, T. E., and Marion, D. (1996) Ectothiorhodospira halophila ferrocytochrome c551: solution structure and comparison with bacterial cytochromes c, *J. Mol. Biol. 264*, 567-584.

[130] Frazao, C., Soares, C. M., Carrondo, M. A., Pohl, E., Dauter, Z., Wilson, K. S., Hervas, M., Navarro, J. A., De la Rosa, M. A., and Sheldrick, G. M. (1995) Ab initio determination of the crystal structure of cytochrome c6 and comparison with plastocyanin, *Structure 3*, 1159-1169.

[131] Takano, T., and Dickerson, R. E. (1980) Redox conformation changes in refined tuna cytochrome c, *Proc. Natl. Acad. Sci. U. S. A. 77*, 6371-6375.

[132] Berggren, G., Adamska, A., Lambertz, C., Simmons, T. R., Esselborn, J., Atta, M., Gambarelli, S., Mouesca, J. M., Reijerse, E., Lubitz, W., Happe, T., Artero, V., and Fontecave, M. (2013) Biomimetic assembly and activation of [FeFe]-hydrogenases, *Nature 499*, 66-69.

[133] Esselborn, J., Lambertz, C., Adamska-Venkatesh, A., Simmons, T., Berggren, G., Noth, J., Siebel, J., Hemschemeier, A., Artero, V., Reijerse, E., Fontecave, M., Lubitz, W., and Happe, T. (2013) Spontaneous activation of [FeFe]-hydrogenases by an inorganic [2Fe] active site mimic, *Nat. Chem. Biol. 9*, 607-609.

[134] Du, J., Sono, M., and Dawson, J. H. (2011) The H93G myoglobin cavity mutant as a versatile scaffold for modeling heme iron coordination structures in protein active sites and their characterization with magnetic circular dichroism spectroscopy, *Coord. Chem. Rev. 255*, 700-716.

[135] Du, P. W., Schneider, J., Luo, G. G., Brennessel, W. W., and Eisenberg, R. (2009) Visible light-driven hydrogen production from aqueous protons catalyzed by molecular cobaloxime catalysts, *Inorg. Chem. 48*, 8646-8646.

[136] Dhanasekaran, T., Grodkowski, J., Neta, P., Hambright, P., and Fujita, E. (1999) p-terphenyl-sensitized photoreduction of CO2 with cobalt and iron porphyrins. Interaction between CO and reduced metalloporphyrins, *J. Phys. Chem. A 103*, 7742-7748.

[137] Hambourger, M., Moore, G. F., Kramer, D. M., Gust, D., Moore, A. L., and Moore, T. A. (2009) Biology and technology for photochemical fuel production, *Chem. Soc. Rev. 38*, 25-35.

[138] Steinreiber, J., and Ward, T. R. (2008) Artificial metalloenzymes as selective catalysts in aqueous media, *Coord. Chem. Rev. 252*, 751-766.

[139] Wang, W., Wang, S., Ma, X., and Gong, J. (2011) Recent advances in catalytic hydrogenation of carbon dioxide, *Chem. Soc. Rev. 40*, 3703-3727.

[140] Wang, W. H., Himeda, Y., Muckerman, J. T., Manbeck, G. F., and Fujita, E. (2015) CO2 hydrogenation to formate and methanol as an alternative to photo- and electrochemical CO2 reduction, *Chem. Rev.*

[141] Kumar, B., Llorente, M., Froehlich, J., Dang, T., Sathrum, A., and Kubiak, C. P. (2012) Photochemical and photoelectrochemical reduction of CO2, *Annu. Rev. Phys. Chem. 63*, 541-569.

[142] Costentin, C., Drouet, S., Robert, M., and Saveant, J. M. (2012) A local proton source enhances CO2 electroreduction to CO by a molecular Fe catalyst, *Science 338*, 90-94.

[143] Costentin, C., Robert, M., Saveant, J. M., and Tatin, A. (2015) Efficient and selective molecular catalyst for the CO2-to-CO electrochemical conversion in water, *Proc. Natl. Acad. Sci. U. S. A. 112*, 6882-6886.

[144] Jeletic, M. S., Mock, M. T., Appel, A. M., and Linehan, J. C. (2013) A cobalt-based catalyst for the hydrogenation of CO2 under ambient conditions, *J. Am. Chem. Soc. 135*, 11533-11536.

[145] Hawecker, J., Lehn, J. M., and Ziessel, R. (1986) Photochemical and electrochemical reduction of carbon-dioxide to carbon-monoxide mediated by (2,2'-bipyridine)tricarbonylchlororhenium(I) and related complexes as homogeneous catalysts, *Helv. Chim. Acta 69*, 1990-2012.

[146] Hayashi, T., Sano, Y., and Onoda, A. (2015) Generation of new artificial metalloproteins by cofactor modification of native hemoproteins, *Isr. J. Chem. 55*, 76-84.

[147] Johnson, F. P. A., George, M. W., Hartl, F., and Turner, J. J. (1996) Electrocatalytic reduction of CO2 using the complexes [Re(bpy)(CO)(3)L](n) (n=+1, L=P(OEt)(3), CH3CN; n=0, L=Cl-, Otf(-); bpy=2,2'-bipyridine; Otf(-)=CF3SO3) as catalyst precursors: Infrared spectroelectrochemical investigation, *Organometallics 15*, 3374-3387.

[148] Kurz, P., Probst, B., Spingler, B., and Alberto, R. (2006) Ligand variations in [ReX(diimine)(CO)(3)] complexes: Effects on photocatalytic CO2 reduction, *Eur. J. Inorg. Chem.*, 2966-2974.

[149] Schneider, J., Vuong, K. Q., Calladine, J. A., Sun, X. Z., Whitwood, A. C., George, M. W., and Perutz, R. N. (2011) Photochemistry and photophysics of a Pd(II) metalloporphyrin: Re(I) tricarbonyl bipyridine molecular dyad and its activity toward the photoreduction of CO2 to CO, *Inorg. Chem. 50*, 11877-11889.

[150] Sullivan, B. P., Bolinger, C. M., Conrad, D., Vining, W. J., and Meyer, T. J. (1985) One-electron and 2-electron pathways in the electrocatalytic reduction of CO2 by fac-Re(2,2'-Bipyridine)(CO)3Cl, *J. Am. Chem. Soc. Chem. Commun.*, 1414-1415.

[151] Nakada, A., Koike, K., Nakashima, T., Morimoto, T., and Ishitani, O. (2015) Photocatalytic CO2 reduction to formic acid using a Ru(II)-Re(I) supramolecular complex in an aqueous solution, *Inorg. Chem. 54*, 1800-1807.

[152] Grodkowski, J., Neta, P., Fujita, E., Mahammed, A., Simkhovich, L., and Gross, Z. (2002) Reduction of cobalt and iron corroles and catalyzed reduction of CO2, *J. Phys. Chem. A 106*, 4772-4778.

[153] Grodkowski, J., Dhanasekaran, T., Neta, P., Hambright, P., Brunschwig, B. S., Shinozaki, K., and Fujita, E. (2000) Reduction of cobalt and iron phthalocyanines and the role of the reduced species in catalyzed photoreduction of CO2, *J. Phys. Chem. A 104*, 11332-11339.

[154] Behar, D., Dhanasekaran, T., Neta, P., Hosten, C. M., Ejeh, D., Hambright, P., and Fujita, E. (1998) Cobalt porphyrin catalyzed reduction of CO2. Radiation chemical, photochemical, and electrochemical studies, *J. Phys. Chem. A 102*, 2870-2877.

[155] Bassegoda, A., Madden, C., Wakerley, D. W., Reisner, E., and Hirst, J. (2015) Reversible Interconversion of CO2 and Formate by a Molybdenum-Containing Formate Dehydrogenase (vol 136, pg 15473, 2014), *J. Am. Chem. Soc. 137*, 4592-4592.

[156] Groysman, S., and Holm, R. H. (2007) Synthesis and structures of bis(dithiolene)tungsten(IV,VI) thiolate and selenolate complexes: Approaches to the active sites of molybdenum and tungsten formate dehydrogenases, *Inorg. Chem. 46*, 4090-4102.

[157] Mota, C. S., Rivas, M. G., Brondino, C. D., Moura, I., Moura, J. J., Gonzalez, P. J., and Cerqueira, N. M. (2011) The mechanism of formate oxidation by metal-dependent formate dehydrogenases, *J. Biol. Inorg. Chem. 16*, 1255-1268.

[158] Morris, A. J., Meyer, G. J., and Fujita, E. (2009) Molecular approaches to the photocatalytic reduction of carbon dioxide for solar fuels, *Acc. Chem. Res. 42*, 1983-1994.

[159] Ward, T. R. (2011) Artificial metalloenzymes based on the biotin-avidin technology: enantioselective catalysis and beyond, *Acc. Chem. Res. 44*, 47-57.

[160] Leung, K., Nielsen, I. M., Sai, N., Medforth, C., and Shelnutt, J. A. (2010) Cobalt-porphyrin catalyzed electrochemical reduction of carbon dioxide in water. 2. Mechanism from first principles, *J. Phys. Chem. A 114*, 10174-10184.

[161] Nielsen, I. M., and Leung, K. (2010) Cobalt-porphyrin catalyzed electrochemical reduction of carbon dioxide in water. 1. A density functional study of intermediates, *J. Phys. Chem. A 114*, 10166-10173.

[162] Sommer, D., Vaughn, M., Clark, B. C., Tomlin, J., Roy, A., and Ghirlanda, G. (2015) Reengineering Cyt b562 for hydrogen production: A facile route to artificial hydrogenases, *Biochim. Biophys. Acta, Bioenerg. In Press*.

[163] Baffert, C., Artero, V., and Fontecave, M. (2007) Cobaloximes as functional models for hydrogenases. 2. Proton electroreduction catalyzed by difluoroborylbis(dimethylglyoximato)cobalt(II) complexes in organic media, *Inorg. Chem. 46*, 1817-1824.

[164] Felton, G. A. N., Glass, R. S., Lichtenberger, D. L., and Evans, D. H. (2007) Iron-only hydrogenase mimics. Thermodynamic aspects of the use of electrochemistry to evaluate catalytic efficiency for hydrogen generation (vol 44, pg 9183, 2005), *Inorg. Chem. 46*, 5126-5126.

[165] Haraguchi, H. (2004) Metallomics as integrated biometal science, *J. Anal. Atom. Spec. 19*, 5-14.

[166] Beinert, H. (2000) Iron-sulfur proteins: ancient structures, still full of surprises., *J. Biol. Inorg. Chem. 5*, 2-15.

[167] Manbeck, G. F., Muckerman, J. T., Szalda, D. J., Himeda, Y., and Fujita, E. (2015) Push or pull? Proton responsive ligand effects in rhenium tricarbonyl CO2 reduction catalysts, *J. Phys. Chem. B 119*, 7457-7466.

[168] Riplinger, C., Sampson, M. D., Ritzmann, A. M., Kubiak, C. P., and Carter, E. A. (2014) Mechanistic contrasts between manganese and rRhenium bipyridine electrocatalysts for the reduction of carbon dioxide, *J. Am. Chem. Soc. 136*, 16285-16298.

[169] Norris, M. R., Concepcion, J. J., Glasson, C. R. K., Fang, Z., Lapides, A. M., Ashford, D. L., Templeton, J. L., and Meyer, T. J. (2013) Synthesis of phosphonic acid derivatized bipyridine ligands and their ruthenium complexes, *Inorg. Chem. 52*, 12492-12501.

[170] Dutta, A., Lense, S., Hou, J., Engelhard, M. H., Roberts, J. A., and Shaw, W. J. (2013) Minimal proton channel enables H2 oxidation and production with a water-soluble nickel-based catalyst, *J. Am. Chem. Soc. 135*, 18490-18496.

[171] Skander, M., Humbert, N., Collot, J., Gradinaru, J., Klein, G., Loosli, A., Sauser, J., Zocchi, A., Gilardoni, F., and Ward, T. R. (2004) Artificial metalloenzymes: (Strept)avidin as host for enantioselective hydrogenation by achiral biotinylated rhodium-diphosphine complexes, *J. Am. Chem. Soc. 126*, 14411-14418.

APPENDIX A

PERMISSION TO REPRODUCE PORTIONS OF CHAPTER 2 FROM *BIOPOLYMERS-PROTEIN SCIENCE*

JOHN WILEY AND SONS LICENSE TERMS AND CONDITIONS

Mar 28, 2016

This Agreement between Dayn J Sommer ("You") and John Wiley and Sons ("John Wiley and Sons") consists of your license details and the terms and conditions provided by John Wiley and Sons and Copyright Clearance Center.

License Number	3837801348295
License date	Mar 28, 2016
Licensed Content Publisher	John Wiley and Sons
Licensed Content Publication	Biopolymers
Licensed Content Title	De novo design of functional proteins: Toward artificial hydrogenases
Licensed Content Author	Marina Faiella,Anindya Roy,Dayn Sommer,Giovanna Ghirlanda
Licensed Content Date	Nov 26, 2013
Pages	14
Type of use	Dissertation/Thesis
Requestor type	Author of this Wiley article
Format	Electronic
Portion	Full article
Will you be translating?	No
Title of your thesis / dissertation	Design of Protein-based Hybrid Catalysts for Fuel Production
Expected completion date	Apr 2016
Expected size (number of pages)	160
Requestor Location	Dayn J Sommer 600 E. Tyler Mall TEMPE, AZ 85281 United States Attn: Dayn J Sommer
Billing Type	Invoice
Billing Address	Dayn J Sommer 600 E. Tyler Mall TEMPE, AZ 85281 United States Attn: Dayn J Sommer

APPENDIX B

PERMISSION TO REPRODUCE PORTIONS OF CHAPTER 2 FROM *BIOPOLYMERS-PROTEIN SCIENCE*

JOHN WILEY AND SONS LICENSE TERMS AND CONDITIONS

Mar 28, 2016

This Agreement between Dayn J Sommer ("You") and John Wiley and Sons ("John Wiley and Sons") consists of your license details and the terms and conditions provided by John Wiley and Sons and Copyright Clearance Center.

License Number	3837801419726
License date	Mar 28, 2016
Licensed Content Publisher	John Wiley and Sons
Licensed Content Publication	Biopolymers
Licensed Content Title	Modulation of cluster incorporation specificity in a de novo iron-sulfur cluster binding peptide
Licensed Content Author	Dayn Joseph Sommer,Anindya Roy,Andrei Astashkin,Giovanna Ghirlanda
Licensed Content Date	Jul 27, 2015
Pages	7
Type of use	Dissertation/Thesis
Requestor type	Author of this Wiley article
Format	Electronic
Portion	Full article
Will you be translating?	No
Title of your thesis / dissertation	Design of Protein-based Hybrid Catalysts for Fuel Production
Expected completion date	Apr 2016
Expected size (number of pages)	160
Requestor Location	Dayn J Sommer 600 E. Tyler Mall TEMPE, AZ 85281 United States Attn: Dayn J Sommer
Billing Type	Invoice
Billing Address	Dayn J Sommer 600 E. Tyler Mall TEMPE, AZ 85281 United States

APPENDIX C

PERMISSION TO REPRODUCE PORTIONS OF CHAPTER 2 FROM THE *JOURNAL OF THE AMERICAN CHEMICAL SOCIETY*

RightsLink®

Home | Account Info | Help | Live Chat

Title:	A De Novo Designed 2[4Fe-4S] Ferredoxin Mimic Mediates Electron Transfer	Logged in as: Dayn Sommer Account #: 3000875976 LOGOUT
Author:	Anindya Roy, Dayn Joseph Sommer, Robert Arthur Schmitz, et al	
Publication:	Journal of the American Chemical Society	
Publisher:	American Chemical Society	
Date:	Dec 1, 2014	

PERMISSION/LICENSE IS GRANTED FOR YOUR ORDER AT NO CHARGE

This type of permission/license, instead of the standard Terms & Conditions, is sent to you because no fee is being charged for your order. Please note the following:

- Permission is granted for your request in both print and electronic formats, and translations.
- If figures and/or tables were requested, they may be adapted or used in part.
- Please print this page for your records and send a copy of it to your publisher/graduate school.
- Appropriate credit for the requested material should be given as follows: "Reprinted (adapted) with permission from (COMPLETE REFERENCE CITATION). Copyright (YEAR) American Chemical Society." Insert appropriate information in place of the capitalized words.
- One-time permission is granted only for the use specified in your request. No additional uses are granted (such as derivative works or other editions). For any other uses, please submit a new request.

BACK CLOSE WINDOW

APPENDIX D

PERMISSION TO REPRODUCE PORTIONS OF CHAPTER 3 FROM *CHEMICAL COMMUNICATIONS*

Reproduced from *Chem. Commun.*, 2014, 50, 15852-15855

APPENDIX E

PERMISSION TO REPRODUCE PORTIONS OF CHAPTER 3 FROM *BIOCHEMICA ET BIOPHYSICA ACTA - BIOENERGETICS*

Title: Reengineering cyt b562 for hydrogen production: A facile route to artificial hydrogenases

Author: Dayn Joseph Sommer,Michael David Vaughn,Brett Colby Clark,John Tomlin,Anindya Roy,Giovanna Ghirlanda

Publication: Biochimica et Biophysica Acta (BBA) - Bioenergetics

Publisher: Elsevier

Date: Dec 31, 1969

Order Completed

Thank you for your order.

This Agreement between Dayn J Sommer ("You") and Elsevier ("Elsevier") consists of your order details and the terms and conditions provided by Elsevier and Copyright Clearance Center.

License number	Reference confirmation email for license number
License date	Mar 28, 2016
Licensed content publisher	Elsevier
Licensed content publication	Biochimica et Biophysica Acta (BBA) - Bioenergetics
Licensed content title	Reengineering cyt b562 for hydrogen production: A facile route to artificial hydrogenases
Licensed content author	Dayn Joseph Sommer,Michael David Vaughn,Brett Colby Clark,John Tomlin,Anindya Roy,Giovanna Ghirlanda
Licensed content date	Available online 12 September 2015
Licensed content volume number	n/a
Licensed content issue number	n/a
Number of pages	1
Type of Use	reuse in a thesis/dissertation
Portion	full article
Format	electronic
Are you the author of this Elsevier article?	Yes
Will you be translating?	No
Title of your thesis/dissertation	Design of Protein-based Hybrid Catalysts for Fuel Production
Expected completion date	Apr 2016
Elsevier VAT number	GB 494 6272 12
Billing Type	Invoice
Billing address	Dayn J Sommer 600 E. Tyler Mall